

# CHALMERS



## Ringhals Diagnostics and Monitoring

*Final Research Report 2012-2014*

V. DYKIN

C. MONTALVO

H. NYLÉN

I. PÁZSIT

*Department of Nuclear Engineering*

CHALMERS UNIVERSITY OF TECHNOLOGY

Gothenburg, Sweden, 2014

CTH-NT-304/RR-19 December 2014



**CTH-NT-304/RR-19**

**December 2014**

**Ringhals Diagnostics and Monitoring,  
Final Research Report 2012-2014**

**V. Dykin, C. Montalvo Martín, H. Nylén and I. Pázsit**

**Department of Nuclear Engineering  
Chalmers University of Technology  
SE-412 96 Göteborg, Sweden  
ISSN 0281-9775**



# **Ringhals Diagnostics and Monitoring, Final Research Report 2012-2014**

**V. Dykin, C. Montalvo Martín, H. Nylén and I. Pázsit**

**Department of Nuclear Engineering, Chalmers University of Technology  
SE-412 96 Göteborg, Sweden**

## **Abstract**

This report gives an account of the work performed by the Department of Nuclear Engineering, Chalmers, in the frame of research collaboration with Ringhals, Vattenfall AB, contract No. 630217-031. The contract constitutes a 3-year co-operative research work concerning diagnostics and monitoring of the BWR and PWR units. The work in the contract has been performed between January 1<sup>st</sup> 2012, and December 31<sup>st</sup>, 2014. During this period, we have worked with four main items as follows:

1. Development and application of the analysis method of core barrel vibrations, developed in the previous Stages, to three ex-core measurements performed during several cycles in R2, R3 and R4. What regards R2, this was the first attempt to analyze ex-core measurements taken at BOC, MOC and EOC, with the new curve-fitting procedure;
2. Investigation of the ultra-low frequency oscillations in reactor power in R4;
3. Development of the theory and simulations in order to determine the void content in R1 from the analysis of in-core measurements;
4. Evaluation of the measurements made in R1 with the use of 4 LPRMs and one TIP detector, for testing the velocity and void fraction profile reconstruction methods.

This work was performed at the Department of Nuclear Engineering, Chalmers University of Technology by Imre Pázsit (project leader), Cristina Montalvo Martín (visitor from the Technical University of Madrid), Victor Dykin and Henrik Nylén, who was also the contact person at Ringhals.



## **Contents**

<b>1. INTRODUCTION</b>	<b>1</b>
<b>2. DEVELOPMENT AND APPLICATION OF THE NEW ANALYSIS METHOD OF CORE BARREL VIBRATIONS TO IN THE PWR UNITS</b>	<b>1</b>
2.1. Introduction, background	1
2.2. General principles and background	4
2.3. The first separation of the double peaks and the hypothesis	8
2.4. Search for the proof of the hypothesis	13
2.5. The mode separation with averaging and the proof of the hypothesis	16
2.6. Results of the measurement made in 2013	17
2.6.1. Details of the measurements in Ringhals 3	17
2.6.2. Analysis of the different components	17
2.6.3. Trend analysis	20
2.7. Measurements made in R2 and R4 in 2014	21
2.8. Conclusions	21
<b>3. INVESTIGATION OF THE ULTRA-LOW FREQUENCY OSCILLATIONS IN REACTOR POWER IN R3 AND R4</b>	<b>23</b>
3.1. Measurement data	24
3.2. Correlation analysis of the neutron noise measurements	26
3.3. 31	
3.3. Signal Transmission Path Analysis	32
3.4. Conclusions	45
3.5. Double transit time in PWR measurements.	46
3.5.1. Calculation of the noise induced by two propagating perturbations travelling with the same velocity in opposite directions.	46
3.5.2. Results and discussion	50
3.5.3. Conclusions	52
3.6. Future work	53
<b>4. DEVELOPMENT OF THE THEORY AND SIMULATIONS TO DETERMINE VOID CONTENT IN R-1 FROM THE ANALYSIS OF IN-CORE NEUTRON NOISE MEASUREMENTS.</b>	<b>54</b>
4.1. Introduction	54
4.2. Model description and simulation	55
4.3. Reconstruction of axial void fraction profile from neutron noise measurements	57
4.4. Reconstruction of axial void velocity profile from the simulated neutron noise measurements	59

4.4.1. Overview of the transit time based method for steam velocity reconstruction	59
4.4.2. Overview of the ANN based method for steam velocity reconstruction	61
4.5. Conclusions	65
<b>5. EVALUATION OF THE MEASUREMENTS MADE IN R1 WITH THE USE OF 4 LPRMS AND ONE TIP DETECTOR, FOR TESTING THE VELOCITY AND VOID FRACTION PROFILE RECONSTRUCTION METHODS</b>	<b>67</b>
5.1. Introduction	67
5.2. TIP-LRPM measurements in the 2012-2014 period	68
5.3. Spectral analysis of the TIP-LRPM signals	69
5.4. Conclusions	80
<b>6. PROPOSAL FOR 2015</b>	<b>80</b>
<b>7. ACKNOWLEDGEMENT</b>	<b>82</b>
<b>REFERENCES</b>	<b>82</b>
<b>APPENDIX A</b>	<b>88</b>
Evaluation of the measurements taken in R2 in 2014	88
<b>APPENDIX B</b>	<b>95</b>
Evaluation of the measurements taken in R4 in 2014	95







## 1. INTRODUCTION

The long term goal of the contract is to utilize the research potential of the Department of Nuclear Engineering at Chalmers in treating reactor physics problems related to the operation of the power plant. This is achieved in a co-operative research project, in the course of which the understanding of relevant problems increases at the department as well as methods are elaborated and implemented for their solution. The results obtained in the earlier stages have been reported in [13]-[31].

The work in three-year contract period has been performed between January 1<sup>st</sup> 2012, and December 31<sup>st</sup>, 2014. During this period, we have worked with four items as follows:

1. Development and application of the new analysis method of core barrel vibrations, developed in the previous Stages, to three ex-core measurements performed during several cycles in R2, R3 and R4.. What regards R2, this was the first attempt to analyze ex-core measurements taken at BOC, MOC and EOC, with the method developed in the previous stages;
2. Investigation of the ultra-low frequency oscillations in reactor power in R4;
3. Development of the theory and simulations in order to determine the void content in R1 from the analysis of in-core measurements;
4. Evaluation of the measurements made in R1 with the use of 4 LPRMs and one TIP detector, for testing the velocity void fraction profile reconstruction methods.

A further general objective of the work is to gain experience with the important and characteristic features of power spectra and certain operational variables in the normal state, in order to be able to perform diagnostics of various phenomena.

A proposal for the continuation of the work for 2015 is also given at the end of this report.

## 2. DEVELOPMENT AND APPLICATION OF THE NEW ANALYSIS METHOD OF CORE BARREL VIBRATIONS TO IN THE PWR UNITS

### 2.1. Introduction, background

Noise investigations in PWRs were started at an early stage in Sweden. The work included the diagnostics of core barrel vibrations in the three PWRs at Ringhals, R2, R3 and R4. Two tools have been developed during the 70's and the 80's by the noise diagnostic community, SPECDEC [1] in Petten, the Netherlands and VIBREAL [2] in Studsvik, Sweden. Both were tested for the analysis of CBM measurements. These methods had some shortcomings in that they assumed that the core barrel vibrations are either completely isotropic, or unidirectional along a fixed line, or a mixture of these two, in order to approximate anisotropic, but not unidirectional vibrations.

When a long-term collaborative research project between Ringhals and Chalmers University of Technology started in 1994 with CBM diagnostics as one item, these methods were reviewed. As a first step, they were generalised to the case of arbitrary anisotropic 2-D vibrations of the core barrel, together with a method of taking various combinations of the four ex-core detectors at the same axial level, in order to enhance either the beam mode, or the shell mode vibrations [39]. The enhanced method was used to perform an analysis of the measurements taken irregularly between 1991 and 1998 [16]. The analysis showed that there was a systematic increase of the beam mode amplitude in all three Ringhals PWRs [16]. This gave rise to some concerns, but did not lead to any further actions at that time. Partly, the number of measurements was too small to give a reliable statistical basis for the speed of the increase of the amplitude; and partly, visual inspection of the core barrel internal components, which takes place every 5 years, did not show any noticeable damage or wear.

The interest in CBM analysis re-emerged in 2005 when the same type of visual inspections showed visible signs of wear in the radial keys and clevis inserts at the lower (and later also at the upper) radial support of the core barrel and core support plate in units 2-4 [3]. The wear appeared to be most serious in Ringhals-3, but inspections in 2012 showed that the play between the radial key and the clevis inserts was most pronounced for Unit 2. It was summarized that the fatigue was caused by increased amplitude of the core barrel vibrations, which in its turn was due to material ageing problems. Hence the hold-down spring of R3 was replaced during the refuelling in connection with the summer outage of 2006. One measurement was taken just before refuelling in R3 and R4, and one after refuelling in all three units, to see the effect of the change of the hold-down spring [5]. Thereafter regular noise measurements were taken in all three units in the consecutive cycles with the goal of having two or three dedicated measurements per cycle. These measurements were evaluated on a regular basis by a consulting company [6]-[7].

It was expected that the amplitude of the vibration peaks would decrease in R3 after the outage, due to the replacement of the hold-down springs, whereas there would be no change in the other units. However, the comparison of the measurements before and after the refuelling showed that the beam mode amplitude peaks dropped in *both* R3 and R4 [5] (a similar statement could not be made for R2 since no measurements were made before the shut-down in the previous cycle). *Fig. 1* shows a plot of the APSD amplitudes in R3 and R4 for different cycles where the increase within the cycle and the decrease after refuelling can be observed for units R3 and R4.

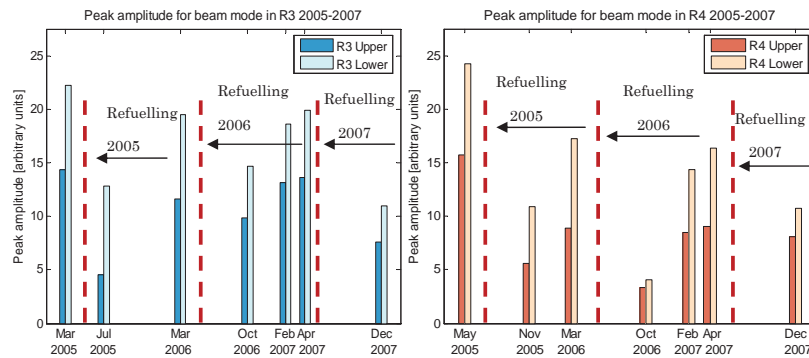


Fig. 1. Evolution of the peak amplitude of the beam mode for some previous cycles in Ringhals 3 (upper figure), and Ringhals 4 (lower figure), taken from Ref. 4.

Hence the decrease of the amplitude could not be attributed to the replacement of the hold-down springs. The further two measurements made during the fuel cycle showed that the amplitudes of the beam mode peaks increased monotonically during the cycle, and reached approximately the same value by the end of the cycle for all units as at the end of the previous cycle. After refuelling the amplitude dropped again approximately to the same value as at the beginning of the previous cycle [6]-[7].

Such a behaviour has been observed also in other PWRs [8]-[9], but it was the first time it was noticed in Ringhals, since previously at most one measurement was made within one cycle. The increase of the amplitude of the peaks in the ex-core detector APSDs raises the question of whether it is due to the increase of the amplitude of the mechanical vibrations, or it is only due to the change of the scaling factor between the mechanical vibrations and the normalised neutron noise. The goal of the investigations in core barrel vibration analysis during the present three-year project was to obtain a clarification of this question.

The dominating opinion in the noise community (which is however not documented and even less proven in the literature) is that the periodic increase of the beam mode vibration peaks is due to the increase of the neutron physical scaling factor between the mechanical vibrations and the induced neutron noise, whereas the amplitude of the vibrations does not change [9]. The increase of the scaling factor is attributed to the change of the boron content during the cycle, as well as to burn-up and flux redistribution effects. Such a conclusion is in analogy with the evolution of the moderator temperature coefficient (MTK) of PRWs, whose magnitude is known to increase monotonically during the cycle, and whose increase is associated with the change of the boron content of the moderator. However, the surmise for a similar increase of the scaling factor of the CBM being attributed to the change in the boron content is not possible to prove from theory or by numerical simulations. In any simple model, a change in the neutronic properties of the moderator or the core will affect both the static flux (the expectations) and the amplitude of the neutron noise, expressed by the vibration peak, the same way. Hence the amplitude of the normalised noise does not change.

In short of a simple theoretical reasoning, numerical methods were resorted to, in order to correctly take into account the spatial and spectral changes due to burn-up and boron change effects during the cycle. Calculations were performed by a dynamic noise simulator used for noise calculations, CORE SIM [25], which uses input core data from operating plants. Calculations performed with core data from the beginning of cycle (BOC), middle of cycle (MOC) and end of cycle (EOC) showed that the scaling factor slightly decreased rather than increased during the cycle with fuel burn-up and decreasing boron content [26]. Hence the increase of the beam mode vibration peak in the ex-core neutron noise APSD during the cycle in the Ringhals PWRs remained unexplained, since it was rather unlikely that the amplitude of the core barrel vibrations should show such a periodic behaviour.

A new attempt was started for the clarification of the phenomenon in 2008 with in-core and ex-core measurements and a refined curve fitting method which was able to resolve multiple peaks in the power spectra. A hypothesis was formulated on the origin of the two peaks close to each other in frequency around the 8 Hz beam mode vibrations. The work leading to the proof of the hypothesis, which required also a deeper understanding and modification of the analysis method, was performed during the present 3-years contract period. The sequence of the work, starting with a hypothesis for the explanation up to the validation of it will be described below.

## 2.2. General principles and background

The analysis of the vibration properties is based on the magnitude of the peaks of auto power spectral densities (APSD) of the ex-core detector signals. It is assumed that the peaks appear as the result of a similar peak in the mechanical spectra of the flow induced stochastic vibrations of the core barrel, through a simple scaling constant  $\mu$ . A typical measurement result, taken in Ringhals 4, is shown in *Fig. 2*. In the neutron spectra two broad peaks can be distinguished: the beam mode, around 8 Hz, and the shell mode around 20 Hz [39]. The latter is of no interest for the present study, which will be focussed on the diagnostics of the beam mode core-barrel vibrations.

For the analysis of the ex-core neutron measurements made between 1991-1998, the previously used VIBREAL and SPECDEC models were developed into a more versatile and robust method [39]. The essence of the method can be summarised as follows. First, the symmetry properties of the signals of four detectors at the same axial level, either upper or lower, with respect to the beam- and shell-mode vibrations as well as the independence of the background noise from the rest are utilised to enhance the beam- and the shell mode contributions as well as the reactivity noise. This is achieved by taking sums and/or differences of the signals of four ex-core detectors at one axial level in the time domain, before the spectral analysis. Then, spectral properties are determined from the specific signal combinations for each vibration mode, and parameters of the motion, again specific to the type of the vibration, are determined.

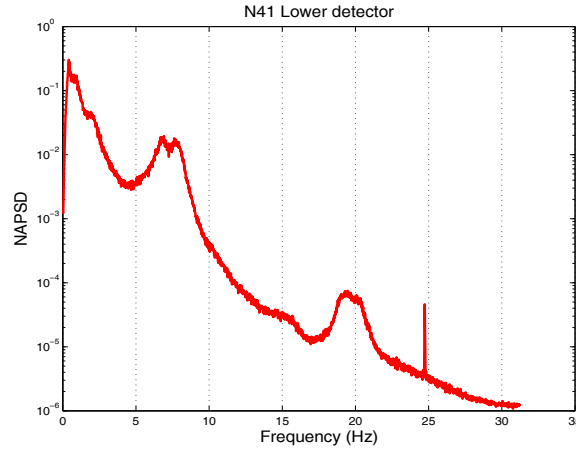


*Fig. 2 Spectra from an ex-core neutron detector from the Ringhals R4 PWR.*

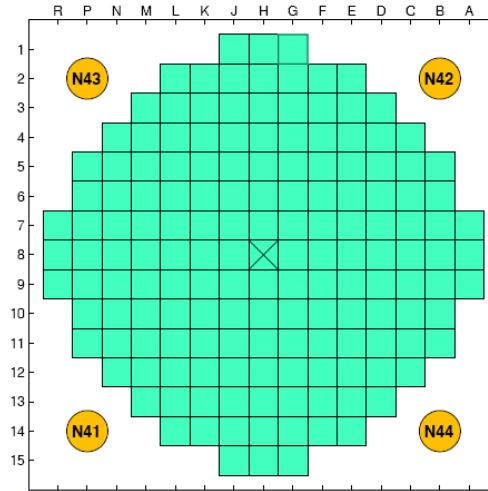


*Fig. 3 Layout of the ex-core neutron detectors placed around the core.*

The beam mode vibrations are considered as a 2-D random walk, which can be characterised by an amplitude  $C$ , anisotropy of the vibrations  $k$ , and preferred direction  $\alpha$  (hence the method is referred to as the  $k - \alpha$  model [39], [56]). With four detectors placed around the core with numbering as shown in Fig. 3, i.e. detectors N41 and N42, as well as N43 and N44 being placed diagonally opposite to each other, these two diagonals will define the  $x$  and  $y$  components of the beam mode vibrations. The neutron noise induced by the beam mode vibrations is proportional to the displacement components, scaled with an (unknown) displacement-to-detector current factor  $\mu$ . The total signals of the four detectors, accounting for all noise components, can be obtained as follows. One assumes that the individual signals of each in-core detector consist of four components, i.e.

an uncorrelated background noise  $\delta r_i(t)$ , a reactivity or point-kinetic component  $\delta P(t)$ , beam mode vibrations of the core barrel  $\mu \delta r(t)$  (containing two directional components  $x(t)$  and  $y(t)$ ), and shell mode vibrations of the core barrel  $D(t)$ . Based on symmetry considerations, the four detector signals can be written as [39]:

$$\delta \phi_1(t) = \delta r_1(t) + \delta P(t) - \mu x(t) + D(t), \quad (1)$$

$$\delta \phi_2(t) = \delta r_2(t) + \delta P(t) + \mu x(t) + D(t), \quad (2)$$

$$\delta \phi_3(t) = \delta r_3(t) + \delta P(t) + \mu y(t) - D(t), \quad (3)$$

$$\delta \phi_4(t) = \delta r_4(t) + \delta P(t) - \mu y(t) - D(t). \quad (4)$$

Here,  $\delta \phi_i$ ,  $i = 1 \dots 4$  stand for the neutron noise from detectors N41, N42, N43 and N44 respectively (either upper or lower),  $\mu$  is the (unknown) scaling factor between the neutron noise and the mechanical vibrations, and  $x(t)$  and  $y(t)$  are the components of the beam mode vibrations. The last two terms in each expression correspond to the core barrel motion modes (beam and shell), and their respective signs express the corresponding symmetry of the vibration modes. The uncorrelated background is due to other processes than the core barrel motion and is hence statistically independent from it; moreover, it is uncorrelated between the four different detectors. The reactivity term may be induced either by independent processes or by the CBM itself, or a combination of the two. We will return to this question later.

The separation of the beam mode and the reactivity components, or rather the enhancement of beam mode component, goes as follows. Based on Eqs (1)-(4), the four detectors at one axial level are used in the following combination to determine the beam mode displacement components:

$$\mu x(t) = \frac{1}{2}(\delta \phi_{41} - \delta \phi_{42}), \quad (5)$$

$$\mu y(t) = \frac{1}{2}(\delta \phi_{43} - \delta \phi_{44}). \quad (6)$$

This signal combination eliminates the reactivity component, and it is assumed that it diminishes the background noise, which is assumed to be small anyway compared to the peak. Amplifying the weight one of the vibration modes (in this case the beam mode) in the time domain by using a suitable combination of the detector signals as above will be referred to as the “mode enhancement” method (to distinguish it from the “mode separation” method, described later).

Along similar lines, the reactivity component can be obtained from the above as

$$\delta P(t) = \frac{1}{4} \sum_{i=1}^4 \delta \phi_i(t) - \frac{1}{4} \sum_{i=1}^4 \delta r_i(t) \approx \frac{1}{4} \sum_{i=1}^4 \delta \phi_i(t), \quad (7)$$



where again it can be assumed that the averaging expressed by (7) eliminates the contribution from the uncorrelated noise. As it will be seen later, the reactivity peak in the frequency spectra can be associated with the individual vibrations of the fuel elements, which is the most recent finding of the recent work, and it represents a deviation from, or rather an addition to the standard model of beam mode vibrations.

Disregarding individual fuel vibrations for the time being, as it was done initially in the project, and considering only the beam mode vibrations, the analysis in the frequency domain goes as follows. If the auto- and cross spectra of the left hand sides of (5) and (6) are denoted as  $S_{xx}(\omega)$ ,  $S_{yy}(\omega)$  and  $S_{xy}(\omega)$ , respectively, then according to the method developed in [39], one has

$$S_{xx}(\omega) = |C(\omega)|^2 (1 + k \cos 2\alpha), \quad (8)$$

$$S_{yy}(\omega) = |C(\omega)|^2 (1 - k \cos 2\alpha), \quad (9)$$

$$S_{xy}(\omega) = |C(\omega)|^2 k \sin 2\alpha, \quad (10)$$

The vibration amplitude  $|C(\omega)|$  can be obtained from the above as

$$APSD_c(\omega) = \frac{S_{xx}(\omega) + S_{yy}(\omega)}{2}. \quad (11)$$

For both the four upper and the four lower ex-core detectors one single amplitude is obtained each, denoted in the continuation as “upper” and “lower”, on which the analysis is made. The peak value of the amplitude  $C(\omega)$  at the beam mode frequency is proportional to the amplitude of the vibrations, such that it takes into account the anisotropy of the motion and its possible change. It does not give the vibration amplitude in absolute terms, due to the unknown scaling factor  $\mu$  between mechanical vibrations and detector current in the formulae. However, if the scaling factor is unchanged, it can be used to perform trend analysis by monitoring the change of the amplitude. This property can be used for long-term trend analysis. Alternatively, a change of the amplitude  $|C(\omega)|$  can instead stand for the change of the scaling factor, as is the assumption for the explanation of the short-term change of the amplitude of the APSD peak within a cycle.

This procedure was applied to analyse several measurements between 2006 and 2009 by a consulting company (for a few samples, see [6], [7], [27]). It was confirmed that the amplitude of the beam mode increases during the cycle and decreases right after the refuelling. However, it was also noted that the phase behaviour and coherence between the detector signals did not always follow the symmetry conditions following from the general considerations. This gave an indication that the assumptions (1)-(4) might not be fully valid. At the same time it was also noticed that sometimes the peak corresponding to the beam mode vibrations showed to be a double peak.

It appeared plausible to assume that a better understanding of the reason of the amplitude increase during the cycle, as well as the inconsistency of the coherence and phase relationships had to do with the presence of a double peak around 8 Hz, and the need arose to separate those two peaks. Hence, for better resolution, the method of separating the peak corresponding to the beam mode vibrations by visual inspection was replaced by a curve fitting procedure. First a curve fitting method, based on the assumption that the shape of the peak in the vibration spectra corresponds to that of a linear damped oscillator, driven by a white noise force, was tried [24],[35]. Although it gave an appreciable improvement as compared to the manual method, it also had some shortcomings, such as the dependence of the simulation of an (unknown) background. Hence another method, based on the Breit-Wigner formula, suggested by Perez and Wood [40] was implemented [26]. As will be described below, it gave significantly better results.

The essence of the method is to fit the measured ex-core detector APSDs to a functional form as

$$APSD(\omega) = \sum_{\lambda} \left\{ \frac{\mu_{\lambda} A_{\lambda} + (\omega - \nu_{\lambda}) B_{\lambda}}{\mu_{\lambda}^2 + (\omega - \nu_{\lambda})^2} + \frac{\mu_{\lambda} A_{\lambda} - (\omega + \nu_{\lambda}) B_{\lambda}}{\mu_{\lambda}^2 + (\omega + \nu_{\lambda})^2} \right\}. \quad (12)$$

Here each resonance in the frequency dependence is characterized by a group of four parameters: the pole strength  $A_{\lambda}$ , resonance frequency  $\nu_{\lambda}$ , damping  $\mu_{\lambda}$  and skewness  $B_{\lambda}$ . This last parameter determines the overlapping between resonances. It is this parameter which makes the formula a very effective tool, because it makes possible to resolve strongly overlapping resonances, the identification of which is otherwise very difficult [32]. A further advantage of the method that it does not require the assumption of a background in addition to the peaks; the aggregate of the tails of the individual peaks, through the curve fitting, gives an excellent fit to the background and hence to the whole spectrum. Because of the effectiveness of this type of curve fitting, it was used in all subsequent work.

### 2.3. The first separation of the double peaks and the hypothesis

Resolving the two peaks lying close to each other in frequency, at around the 8 Hz beam mode frequency, is a crucial advantage of the curve fitting method applied. Its first application for the separation of the two peaks in order to clarify the reason of the increase of the beam mode peak during the cycle was made in Stage 12 of the Chalmers-Ringhals collaboration project in 2007-2008. Three measurements, taken during cycle 24 of R4, in October 2006, and February and April 2007, respectively, were evaluated. The selection of the cycle and the unit was due to the fact that up to that date, this was the only cycle in which three measurements were taken within one cycle.

Some sample results of the curve fitting and the separation of the peaks are shown in 4 Fig. 4 and Fig. 5. In this phase of the project the curve fitting was done up to 10 Hz, since the beam mode peak is around 8 Hz. In later stages the fitting range was extended by

adding more peaks to the assumed curve shape, but it did not lead to significant improvements, hence one returned to the fitting up to 10 Hz only.

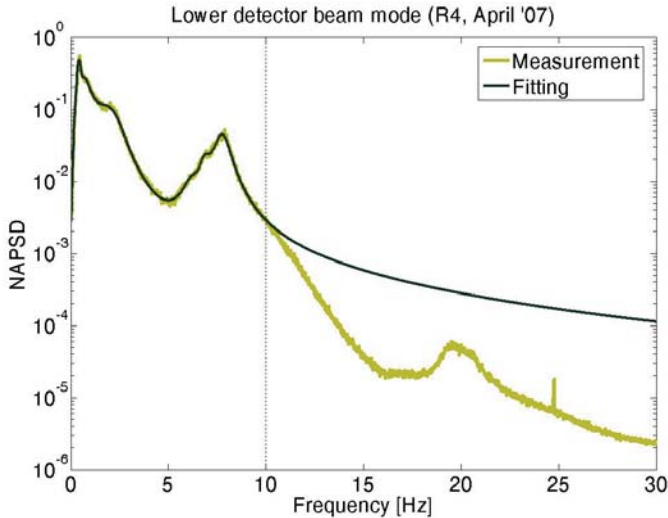


*Fig. 4 Result of the fitting procedure on the upper detector beam mode amplitude in the measurement in April 2007, cycle 24 of Ringhals 4*

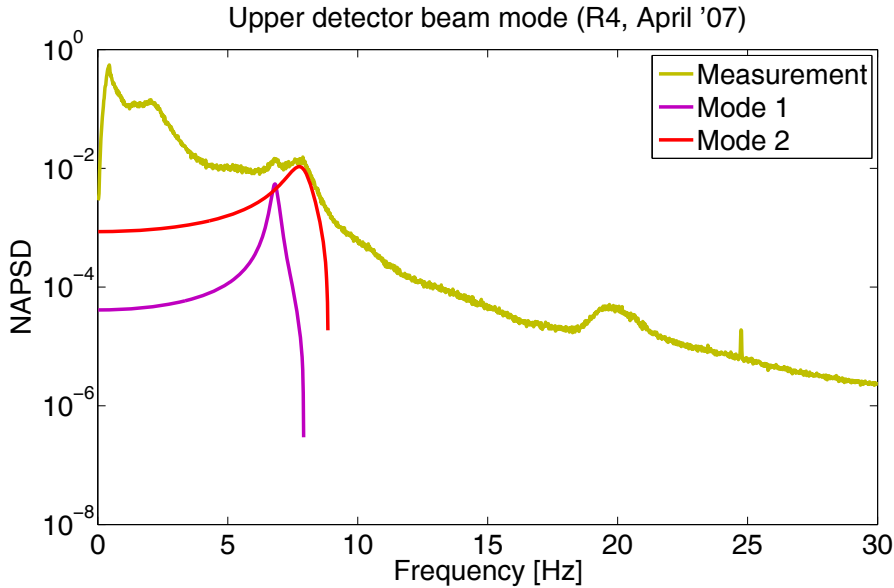


*Fig. 5 Separation of the two beam mode peaks with the Breit-Wigner fitting method.*

As the above illustration shows, in all beam mode amplitude spectra, two peaks could be distinguished and their amplitudes quantified around 8 Hz. One peak is located around 6.8 Hz, which will be referred to as Mode 1 and the other around 7.9 Hz, referred to as Mode 2<sup>1</sup>. An analysis of the three measurements during the cycle showed that the amplitude of Mode 1 remained roughly constant during the cycle, whereas the amplitude of Mode 2 changed rather markedly, i.e. increased monotonically during the cycle. No significant change in the frequencies was observed for either peaks. The results of the trend analysis of the amplitude evolution during the cycle are shown in *Fig. 6* for the lower detectors. The figures also indicate the evolution of the amplitudes obtained from the type of analysis made earlier, in which no distinction between the two peaks was made and they were considered as one single peak. Such an analysis yields a single resonance frequency which changes during the cycle. The reason is that, in terms of the resolved peaks, at the beginning of the cycle Mode 1 had the larger amplitude, whereas from the middle of the cycle, Mode 2 was dominating. The frequency determined by the traditional method was equal to that of the dominating component to distinguish between the beam and shell modes and even the reactivity component.

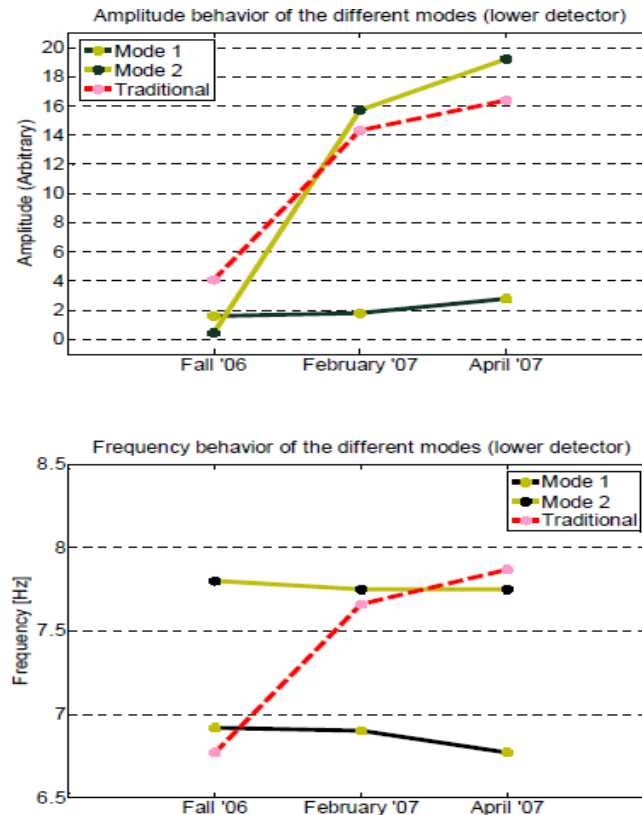


*Fig. 6 The evolution of the amplitudes of the two peaks of the lower detectors, compared to the traditional method assuming only one peak.*

<sup>1</sup> Note that the term “Mode” here is used to distinguish between the two peaks in the beam mode vibrations, hence it has a meaning different from the term “mode”, used to distinguish between the beam and shell modes and even the reactivity component.

The different behaviour of the two peaks indicates that they represent two different phenomena and have different origin. In order to expedite the identification of the character of the processes leading to the two separate peaks, concurrently some complementary measurements were performed in 2008. These were made by using movable in-core detectors at five different radial positions, with each detector at six different axial positions. The incentive of these measurements was to determine the axial profile of the amplitude of the noise in the vibration peak, in order to identify fuel assembly vibration modes, as suggested in Ref. [38] by Sweeney et al. Fuel assembly vibrations showing the characteristics of a pendular motion, i.e. fixed upper point and free movement of the lower end should be induced by the motion of the core barrel, whereas fundamental mode and higher order, more involved axial noise amplitude modes could be attributed to fuel assembly vibrations. Such measurements were performed and analysed already in Stage 4 of the collaboration project [17], but at that time they were not connected to the core barrel vibration diagnostics.

The details of the measurements made in 2008 and their evaluation are found in [34] and [26], here only a short summary is given. Similarly to the ex-core measurements, the in-core detector spectra also contained several peaks, approximately at the same frequencies as the peaks of the ex-core detector spectra. The axial dependence of the amplitudes of these peaks was evaluated manually, and not by the curve fitting procedure. The axial dependence of the peak amplitudes for the two relevant frequencies at 6.8 (Mode 1) and 7.9 Hz (Mode 2) are shown in *Fig. 7* and *Fig. 8*.

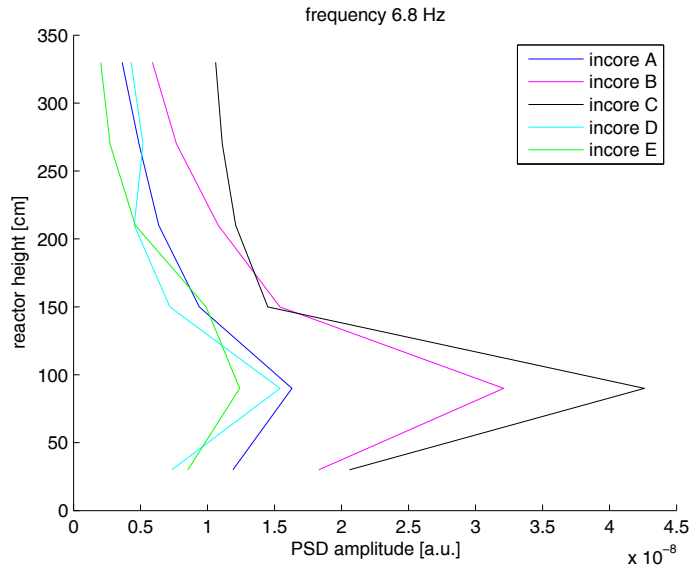


*Fig. 7 Axial profile of amplitudes for Mode 1 obtained from in-core movable detectors.*

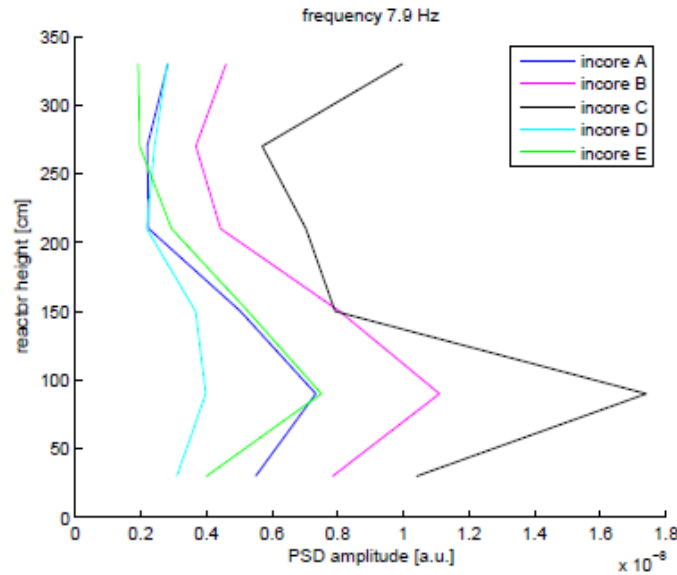


Fig. 8 Axial profile of amplitudes for Mode 2 obtained from in-core movable detectors.

In view of the fact that the in-core measurements are primarily sensitive to individual fuel assembly vibrations, from Fig. 7 and Fig. 8 the conclusion was drawn that the peak at 6.8 Hz resembles to the fuel assembly vibrations due to the beam mode movement of the core barrel, whereas the higher frequency peak at 7.9 Hz is due to the first bending mode of the individual fuel assembly vibrations, induced by the turbulent flow and being largely independent of the core barrel motion.

It has to be added that this conclusion is not completely unambiguous, because the results are not fully consistent. E.g. for the peak at 6.8 Hz, which is assumed to be induced by the vibrations of the core barrel, the amplitude should have a maximum in the lowermost detector signal, whereas in the measurements the maximum is not at the lowermost level. Further, the amplitude should not have a local maximum at the uppermost position, rather it should be a local minimum. The axial dependence shown in Fig. 8 indicates as if there was a free movement possible for the fuel assemblies also at the upper level, just as much as at the lower level, which is conceivable. Very recent observations suggest that even the core barrel movement can include lateral vibrations at the upper level. However, taking all facts into account, the assumption on the origin of the two peaks stated above is the “best estimate” that can be obtained from the measurements.

Based on the facts described in the foregoing, a hypothesis was formulated on the origin of the two peaks (modes) in the ex-core neutron spectra. Mode 1 is associated with the beam mode vibrations of the core barrel. The measurements show that the amplitude of Mode 1 does not change during the cycle, or only very moderately. If the scaling factor between the CBM and the ex-core detector signal does not change during the cycle, as the CORE SIM calculations reported in [26] found, it means that the amplitude of the beam mode core barrel vibrations does not change during the cycle, which is reassuring. This

does not exclude the possibility of a long-term trend, as found in the earlier measurements taken over a long period of time [16].

Mode 2 in the ex-core detector APDSs is associated with the incoherent vibrations of the individual fuel assemblies, induced by the turbulent flow. The amplitude of this peak in the APSD increases monotonically during the cycle. Then the same question arises as with the CBM before, namely whether this increase corresponds to the increase of the amplitude of the vibrations, or to that of the scaling factor. A change in the vibration properties of the fuel assemblies is easier to understand than that of the core barrel vibrations, since their mechanical properties change during the cycle due to the burnup. This is not the case for the core barrel, whose properties only change over a time scale much longer than a cycle length. It is also possible that the scaling factor between fuel assembly vibrations and the ex-core detector signals changes during the cycle, since this was not investigated in the previously mentioned CORE SIM calculations. Such calculations were performed quite recently, and they show that if several fuel assemblies vibrate at various positions independently of each other, then the scaling factor between the mechanical vibration effect and the ex-core neutron noise indeed shows a monotonic increase during the fuel cycle [33].

The possibility that individual fuel assembly vibrations can be detected by the ex-core detectors was already suggested by Sweeney et al. [41]. They claimed that the beam mode peak corresponds to the vibrations of fuel assemblies, induced by core barrel support motion and therefore, any change in fuel loading or fuel design may change the ex-core neutron APSDs profiles. Moreover, they also performed calculations of the scaling factor between individual fuel assembly vibrations and the induced ex-core noise, and found that it increased during the cycle. However, it has to be noted that their calculations were based on static Monte-Carlo methods. Static calculations can be used to calculate the scaling factor for the CBM, since it is basically a geometry effect without any dynamics, as it was already mentioned in [51]. However, the noise induced by the vibrations of fuel assemblies requires dynamic calculations with the inclusion of delayed neutrons. This is because the vibration of a localised core component, either a control or absorber rod, acts as a perturbation within the core and will generate a neutron noise that contains both a reactivity (point kinetic) component and a space-dependent component which interfere with each other in a way that is determined by the rod/assembly position and vibration trajectory [37], [56]. This gave the incentive to calculate the ex-core neutron noise induced by fuel assembly vibrations with the dynamic core simulator CORE SIM, and the results confirmed the need of using a dynamic code for such calculations [33].

#### **2.4. Search for the proof of the hypothesis**

Further measurements were taken in Ringhals R4 and R3 in the next cycles. In 2009-2010 (Stage 13 of the collaboration project, Ref [28]), both in-core and ex-core measurements were made in R4. Although three measurements were planned, only two could be executed, in February and April 2009, respectively. The purpose was still to

confirm or deny the hypothesis formulated above, and also to test the fitting procedure to fit the whole spectra, up to 20 Hz. The fitting procedure was applied not only in ex-core spectra but also the in-core APSDs. A sample result of the fitting of the spectra up to 20 Hz in one of the ex-core signals is shown in *Fig. 9*.

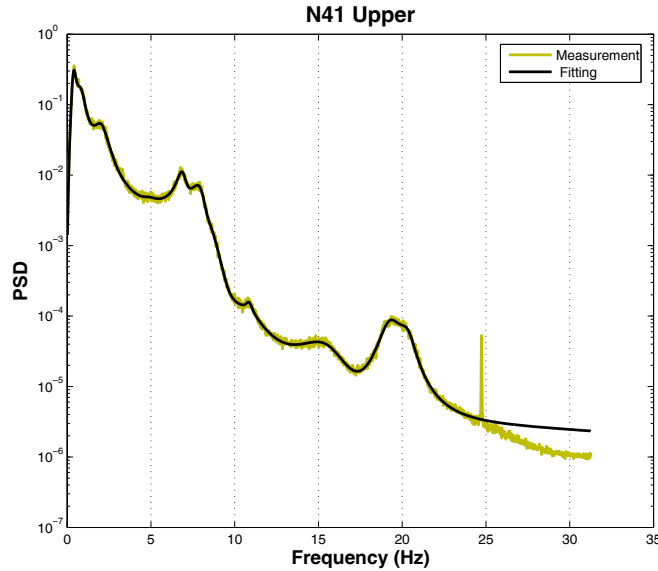


*Fig. 9 APSD of an ex-core neutron detector from Ringhals R4, with the curve fitting extended to 20 Hz.*

Both in-core and ex-core results were consistent with previous measurements. The result of the in-core measurements gave the same picture as in the previous Stage, i.e. suggesting that Mode 1 is induced by the CBM and Mode 2 by the individual fuel assembly vibrations. Regarding the trend analysis of the amplitudes of the modes from the ex-core measurements, the results were largely inconclusive. The main reason was that the time span between the two measurements was only 3 months. Hence the different time evolution of the two modes, with the amplitude of Mode 1 remaining unchanged and that of Mode 2 monotonically increasing, could not be reproduced at that time. The behaviour was different for the upper and the lower detectors, but both modes evolved similarly to each other for both the upper and lower detectors. The results of the trend analysis are shown in *Fig. 10*.

At this point an aspect was realised that had been overlooked so far. Namely, the assumption of Mode 2 being due to fuel assembly vibrations is inconsistent with the signal processing applied in the procedure. The analysis is made on the beam mode component, separated from the other components (reactivity, shell mode and uncorrelated noise) based on Eqs (5), (6), and (8)-(11). This separation is based on a symmetry property of the signals which holds only for the ex-core noise induced by the beam mode vibrations but not for the individual fuel assembly vibrations. The ex-core noise induced by individual vibrations of the fuel assemblies does not possess such symmetries at all (except for the



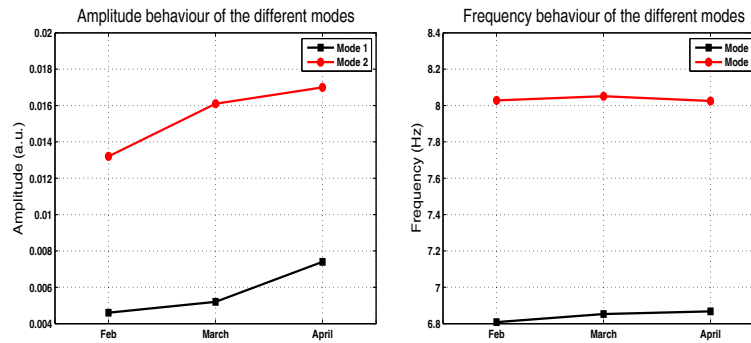


*Fig. 10 Time evolution of the amplitude and the frequency of the two modes in the measurements in 2009 in R4.*

singular case of a fuel assembly vibrating in the geometrical centre of a core with complete azimuthal symmetry). Neither the phase nor the amplitude relationships between opposite detectors will show the same symmetry properties as that of the pendular motion of the core barrel. Rather, these will be much more complicated and moreover will depend on the position of the vibrating fuel element in the core and the vibration pattern in space [37], [56].

This recognition served also as a possible explanation why in earlier work the coherence and phase relationships between the detector signals at the frequency of the core barrel motion were contradictory with the expected symmetry properties. In those earlier investigations the core barrel (Mode 1) and fuel assembly (Mode 2) vibrations were not separated, and hence the results were influenced by the inclusion of the fuel assembly vibrations which do not possess the symmetry properties. This observation gives further support to the hypothesis that Mode 2 is induced by fuel assembly vibrations.

In view of this it was decided that for the analysis of Mode 2, it is more consistent to evaluate the amplitudes individually for each detector. The need of the comparison of the amplitudes of Mode 2 with Mode 1 necessitated that even Mode 1 was evaluated separately for all 8 detectors, without making use of the beam mode symmetries. Hence from 2011 (Stage 14, Ref. [29] and Stage 2012, [30]), the curve fitting procedure was applied individually to all 8 detectors, without the averaging procedure. This procedure was fairer for Mode 2, but it had the adverse effect that the interpretation of the results became complicated. Instead of one trend curve for the upper four and one trend curve for the lower four detectors for the two modes, there was a total of 8 trend curves, which in addition had all different trends (even opposing trends) for each mode.

The results of such a trend analysis from Stage 14 are shown in *Fig. 11*. The left hand side figure shows the development of the amplitude of Mode 1, and the r.h.s. figure that of Mode 2, for all 8 detectors separately. The trend analysis (temporal evolution of the amplitudes) is made by comparing the values of the blue curve (representing the data in the January measurements) with those of the red curve (data from the June measurements). The difference represents the evolution of the amplitude, shown for all 8 detectors (4 upper

and 4 lower), respectively. It is clear that the analysis and the interpretation become cumbersome and it is not easy to extract a trend from the individual detector signals.

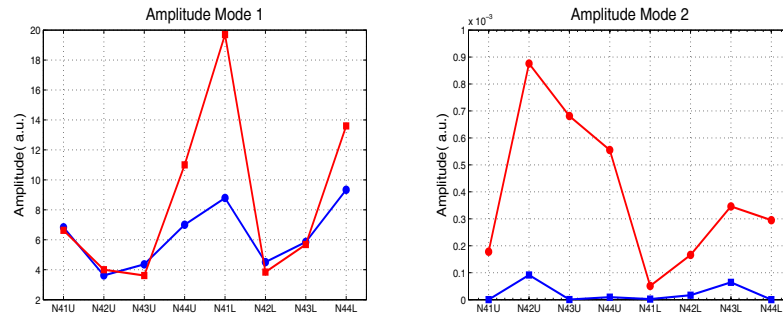


Fig. 11 APSDs of the beam mode (Mode 1, left figure) and of the reactivity component (Mode 2, right figure) after the separation, extracted from the measurements taken in January 2013 (blue line) and in May 2013 (red line) at Ringhals-3.

## 2.5. The mode separation with averaging and the proof of the hypothesis

Three measurements were performed in R3 in 2013, on 26 February, 16 April and 5 July 2013. The problem with the analysis above is that the results cannot be compressed to fewer variables by some averaging method such as the one used before, which would also reduce the scatter and uncertainty present in the individual signals. However it was possible to find a way out. The solution is to perform a different averaging for Mode 1 and Mode 2. This is based on the assumption that Mode 2 can be associated with the reactivity component of the signals, as defined by Eq. (7), suggested originally in Ref. [39]. With this assumption, the trend analysis is performed as follows. The peak amplitude for Mode 1 is determined by curve fitting to the averaging belonging to the beam mode, as before, whereas the peak amplitude for Mode 2 is determined by curve fitting belonging to the reactivity component. This procedure will be referred to as the “mode separation” method.

The association of Mode 2, i.e. the effect of the fuel assembly vibrations with the reactivity term, while at the same time assuming that in Mode 1 there is no reactivity component, can be motivated as follows. Fuel assembly vibrations, as a rule, have a reactivity effect in first order of the vibration amplitude. The exception is when the assembly vibrates in a zero static flux gradient, such as at the centre of the reactor, or off-centre, but vibrating along a line in a tangential direction. Such cases are unlikely already for a single assembly, and since one can assume that several assemblies vibrate at the same time, the probability of this happening is practically zero. On the other hand, due to symmetry considerations, pendulum vibrations of the core barrel, i.e. beam mode vibrations, can be compared to the case of the vibrations of a central control rod. Since displacement of the core barrel from the central position must have the same reactivity effect to whichever direction the core barrel moves, the central position must be a local minimum or maximum for the reactivity effect, i.e. the derivative of the reactivity change

along the displacement is zero. Thus, the reactivity effect of the vibration of the core barrel is only second order in the vibration amplitude.

The analysis of the measurements made in 2013 was performed along these lines. The principles of separating the beam mode component and the reactivity component will be described in the next subsection. As will be demonstrated, this procedure gave significantly better results than any of the two previous methods.

Hence, the analysis from the measurements made in 2013 in R3 was much more conclusive. Although the double peak in the beam mode frequency range region was difficult to resolve in either the individual detector spectra or in the averaged signal which enhances the beam mode, with the new method it worked very satisfactorily. First the beam mode was enhanced applying equations (5) and (6) to the signals from opposite detectors and the amplitude of the lower frequency peak was fitted. Mode 2, related to fuel assembly vibrations was obtained by calculating the global or reactivity noise according to Eq. (7) and a separate curve fitting was performed. The separation of the reactivity and the beam mode led to better fitting results.

## **2.6. Results of the measurement made in 2013**

### **2.6.1. Details of the measurements in Ringhals 3**

Three ex-core detector measurements were performed in Ringhals 3 in 2013, on 26 February, 16 April and 5 July 2013, corresponding to cycle 32. The sampling frequency in the present measurements was 62.5 Hz for all three sets of measurements. As it was concluded in earlier work, for the analysis of the beam mode vibrations, it was sufficient to perform the curve fitting only up to 10 Hz, and the fittings in the present work were made only up to this frequency.

### **2.6.2. Analysis of the different components**

Some illustrations of the results of the mode separation are shown in *Fig. 12-Fig. 14* below, which show the spectral regions of the beam mode around 8 Hz, the shell mode around 20 Hz, and a narrow peak corresponding to the pump frequency of 25 Hz. Analysis results for the individual detector signal N41 upper, as well as the beam mode component extracted from all four upper detector signals, are shown in *Fig. 12*. It is seen that, in addition to the fact that the peak corresponding to the extracted beam mode (red line) is narrower than the peak in the original spectra (green line), it is also located at the lower frequency part of the wide peak of the individual detector. This is in full agreement with the formerly formulated hypothesis that the individual detector peaks contain the sum of the two peaks corresponding to the beam mode (Mode 1, lower frequency) and the fuel assembly vibrations (Mode 2, higher frequency). It is also noted, however, that the frequency of Mode 1 is about 8 Hz, which is higher than the corresponding frequency of Mode 1 observed previously in R4 (6.8 Hz).

In contrast to some previous measurements, in the present measurements, the presence of two peaks cannot visually be seen either in the individual detector signals or in the beam mode component. The separation of the modes, based on solely the curve fitting procedure from the individual detector signals, would be rather difficult and inaccurate, which explains the failure of some previous attempts.

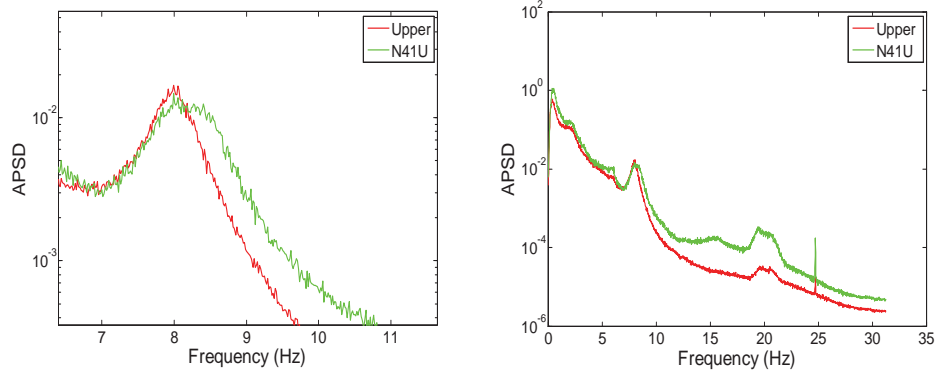


*Fig. 12 APSDs of the extracted beam mode (Mode 1, red line) and of the individual upper detector N41 (green line) from the measurement taken in May 2013 at Ringhals-3. The left figure is amplitude of the Beam Mode peaks resulting from fitting the spectra of each individual detector.*

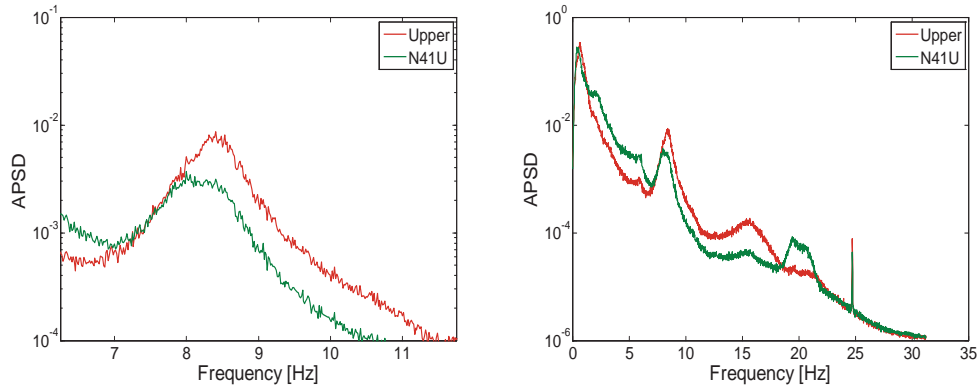


*Fig. 13 APSDs of the extracted reactivity component (Mode 2, red line) and of the individual upper detector N41 (green line) from the measurement taken in May 2013 at Ringhals-3. The left figure is a close up of the spectral region of interest from the right figure.*

The effect of the extraction (enhancement) of the reactivity component from four detector signals is illustrated in *Fig. 13*. In contrast to the beam mode, the peak corresponding to the reactivity component of such a separation of the reactivity component is not narrower than the peak in the individual detector signal, but its peak is at the high frequency part of the peak of the single detector signal. The peak frequency is about 8.6

Hz, which is again higher than the frequency of Mode 2 measured earlier in R4 (7.9 Hz). This further underlines and confirms the hypothesis that the reactivity component can be used to quantify the effect of the individual fuel assembly vibrations, representing Mode 2.

Some plots of the extracted beam mode and reactivity mode components are shown in Fig. 14, for the measurements taken in May 2013. The figure also shows that the peak amplitude of the beam mode component is larger for the lower detectors as for the upper detectors, whereas no such tendency is visible for the reactivity component. One can see again that the frequency of the beam mode is lower than that of the individual fuel assembly vibrations. From the spectra of the extracted components, by curve fitting the amplitudes of the peaks can be determined, and a trend analysis of the evolution of the amplitudes during the cycle can be made.

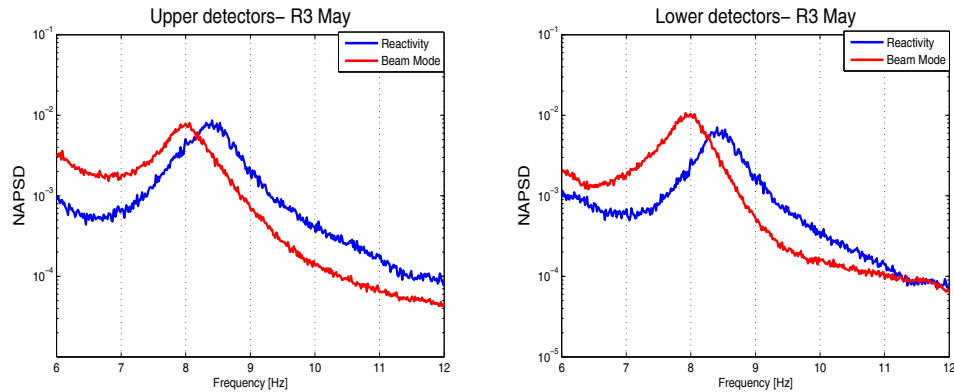


*Fig. 14 APSDs of the beam mode (Mode 1, red line) and of the reactivity component (Mode 2, blue line) after the separation, extracted from the measurement taken in May 2013 at Ringhals-3 for the upper (left figure) and lower detectors (right figure).*

Apart from the differing frequencies of the separated components Mode 1 and Mode 2, the phase behaviour between diagonally opposite detectors also shows a behaviour which is consistent with the hypothesis. Fig. 15 shows the APSDs of the separated beam mode and reactivity components, as well as the phase between the detectors N41L - N42L. It is seen that the phase is  $\pm 180^\circ$  up to about 8.5 Hz, i.e. over the whole frequency range of the beam mode core barrel vibrations. At 8.5 -8.6 Hz, which is the peak frequency of the reactivity component, the phase abruptly changes from  $180^\circ$ , i.e. out-of-phase behaviour, to zero degree, i.e. to in-phase behaviour. This is in agreement with the assumption that the peak at 8.6 Hz, i.e. Mode 2, corresponds to the reactivity effect of the vibrating fuel assemblies.

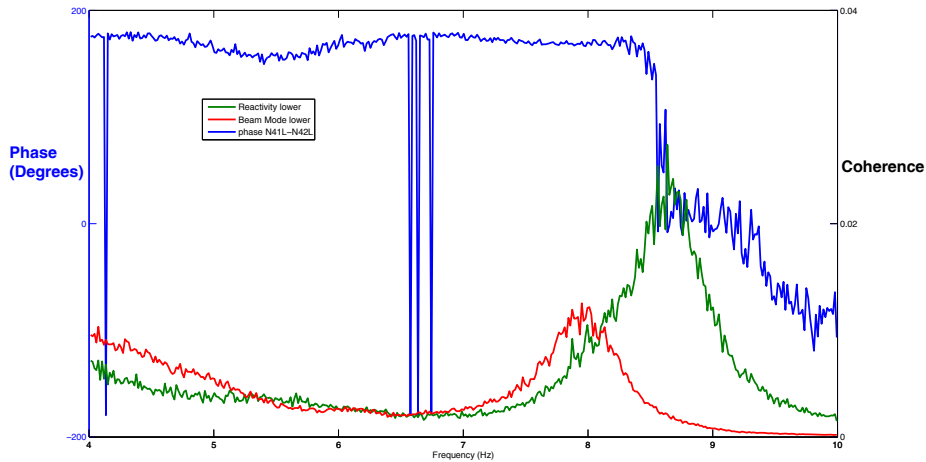


Fig. 15 Reactivity and beam mode spectra of the lower detectors for R3 plotted jointly with the phase of the CPSD for the diagonally opposite detectors N41L-N42L.

### 2.6.3. Trend analysis

The results of the trend analysis are shown Fig. 16. It is seen that the amplitude of the beam mode (Mode 1) does not change much during the cycle, whereas the fuel assembly vibration mode (Mode 2) experiences an appreciable increase in the amplitude. The trends for the upper and the lower detectors are similar with respect to the interrelation between the two different modes.

The results of the trend analysis also give further support to the hypothesis on the different physical origin of the two peaks. As it is seen in Fig. 16, the average (over the

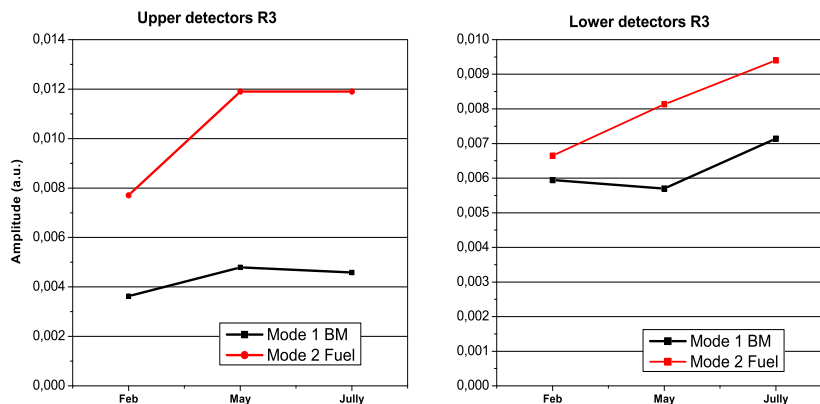


Fig. 16 Trend analysis of the amplitude of the Mode 1 (beam mode, blue line) and Mode 2 (reactivity component, red line) after the separation from the measurement taken 2013 at Ringhals-3 for the upper (left figure) and lower detectors (right figure).

fuel cycle) amplitude of Mode 1 is larger for the lower detectors than for the upper detectors, whereas for Mode 2 the amplitudes are comparable (or even larger for the upper detectors). This is consistent with the assumption that Mode 1 is the beam mode, which is associated with pendulum vibrations of the core barrel. On the other hand, since Mode 2 represents the individual fuel assembly vibrations, there is no such expectation on the axial dependence of the neutron noise at the vibration peak.

## 2.7. Measurements made in R2 and R4 in 2014

During 2014, new measurements were made in both R2 and R4. The evaluation of these measurements is found in Appendix A and B, respectively.

Regarding the analysis of R2, as it was already seen in the previous period, the structure of the spectra, i.e. the number and the peak frequencies of the peaks is different from those in R3 and R4, which are much more similar to each other, for obvious reasons. As Fig. 65 and Fig. 66 in Appendix A shows, the APSD of the ex-core detector signals in R2, several peaks appear between the beam mode and the shell mode peaks. One reason for the difference in the vibration spectra, reflected in the ex-core detector APSDs, is the difference in the thermal shield construction in R2 on one hand and in R3 and R4 on the other. Also, the beam mode peak is a single one, not showing the double peak character which helped in R3 and R4 to distinguish between the vibrations of the core barrel and the individual vibrations of the fuel assemblies.

Because of these differences, and also because of the different spectral (coherence and phase) properties of the R2 spectra, a similar separation of the beam mode and reactivity components as in R3 and R4, was not possible to make. For this reason, no reliable method for the trend analysis was found yet. This will be achieved in future work.

The evaluation of the measurements in 2014 in R4 showed similar trends as in the previous cycles. In the individual detector APSDs, two peaks can be seen at the beam mode frequency. However, after the separation of the pure beam mode and the reactivity components, there is still a double peak seen in the latter. This implies that the beam mode vibrations would also have a reactivity effect. The trend analysis shows that the reactivity component increases during the cycle as it did in the previous cycles, but the beam mode component also shows some increase. The reason for this may be connected with the appearance of the double peak in the reactivity component. Apart from this, the trend analysis is consistent with the previous cycles in that the increase of the reactivity component is markedly higher than that of the beam mode component. Surveillance of the core barrel motion will be continued in the next stages of the project.

## 2.8. Conclusions

Based on work in the previous Stages of the project, the hypothesis was suggested that at the beam mode vibration frequency, there are two peaks close to each other in the ex-core detector power spectra, which have different physical origins. According to the hypothesis, the lower frequency peak (Mode 1) belongs to the core-barrel vibrations, or

fuel assembly vibrations induced by the core barrel vibrations, and the higher frequency peak (Mode 2) corresponds to the individual, flow-induced vibrations of the fuel assemblies. During a fuel cycle, the amplitude of Mode 1 is roughly constant, whereas the amplitude of Mode 2 increases monotonically.

The results of the present analysis confirm the hypothesis concerning the different behaviour, and hence different physical origin, of the two peaks of the ex-core detector APSDs in the beam mode vibration domain. Further, they confirm the hypothesis of a constant Mode 1 corresponding to core barrel vibrations and monotonically increasing amplitude of Mode 2, which would correspond to the noise induced by individual fuel assembly vibrations. As a result, the main aspects of the behaviour are consistent with the hypothesis and the overall picture seems to become coherent. A further, indirect support for the hypothesis is provided by the analysis reported in Ref. [33], where it is shown that under general circumstances, the scaling constant between the vibration of fuel assemblies distributed over the core and the ex-core neutron noise induced by the vibrations increases monotonically during the fuel cycle.

The method will be tested further in the continuation of the collaboration project between Chalmers and Ringhals. Also, an extension of the method is planned, by taking all 8 (both upper and lower) detectors into account simultaneously, in order to try to quantify and diagnose 3-dimensional tilted vibration modes, since there are indications for the possibility of such vibration modes

Further, a deeper analysis of the vibration properties of Ringhals-2 is also needed in the future. As it was reported in the 2013 Stage of the project, the vibration properties of Ringhals 2 deviate from those of Ringhals 3 and 4, and the same mode separation method is not applicable. Further work is necessary to be able to interpret the measurements made in Ringhals-2.



### 3. INVESTIGATION OF THE ULTRA-LOW FREQUENCY OSCILLATIONS IN REACTOR POWER IN R3 AND R4

Some results on the investigation of ultra-low frequency oscillations in R3 and R4 are presented and discussed. This study was motivated by a general increase in the neutron noise amplitude level observed for some time in both units, which led to operational disturbances including certain alarms. More detailed description on the background can be found in the previous reports, Stage 13 and Stage 14 [28], [29]. Some preliminary results were already reported in Stage 14, which were not conclusive, and it was decided to continue the investigation in the period 2012-2014. Two new sets of measurements were performed and their DC components were analyzed. The measurements were taken in Ringhals-4 on 2012-08-09 and on 2014-07-23 during 6 hrs, using a 4 Hz sample rate. More details on the measurements can be found in the previous report [29].

In 2012 the analysis of the measurements was performed along two lines. The first one was a cross-spectral and cross-correlation analysis of the selected ex-core detector – core exit thermocouple pairs. The motivation for this was to determine the radial dependence of the coolant velocity between the corresponding detector pairs which could help to explain the ultra-low frequency oscillations [53]. More details on this topic are given in the corresponding report. The spectral analysis of new measurements pointed out several interesting features. One of them was the fact that it was possible to obtain a reasonable estimation of the transit times by using a linear fit to the phase of the CPSD function. These results for the transit times appeared to be in a good agreement with the preliminary theoretical estimations, as well as with the results obtained earlier for Ringhals-4.

Another type of investigations implemented in 2012 and 2014, is a so-called bi-variable or multi-variable partial autoregression analysis, also known as Signal Transmission Path (STP) Analysis (Ref. [46]-[49]). The main idea behind the STP is that for signals coupled through some physical process (feedback), it might be possible to point out which signal is the reason (source), and which is the consequence (the affected signal) by analysing the measured fluctuations in the respective signals. Such a method provides both the information about different coupling mechanisms between measured signals (direct/indirect effect), as well as the main source driving the phenomenon. To this end, STP analysis was performed for different combinations of ex-core neutron detectors and core exit thermocouples, with a dedicated MATLAB-based software.

One more interesting feature which was also highlighted in the previous report [29] was the presence of two different slopes in the phase of the coherence function (one between 0.1-0.4 Hz and another one between 0.4-0.8 Hz) observed for several detector pairs.

As an illustration, in *Fig. 17*, the phase of the CPSD function calculated between neutron detector N41 Upper and exit thermocouple M11 is plotted. The figure indicates the presence of two different slopes referring to probably two different transit times. Such a strange phase behaviour had already been noticed in the early 70s, in the measurements performed for BWRs, but had never been confirmed for PWRs. At that time, no clear interpretation of this phenomenon was found. One possible explanation of the presence of two different slopes in a PWR case might be due to the fact that each ex-core neutron detector senses the same signal twice, i.e. first time when the perturbation passes the neutron detector in the downcomer region, and second time after some time delay when it

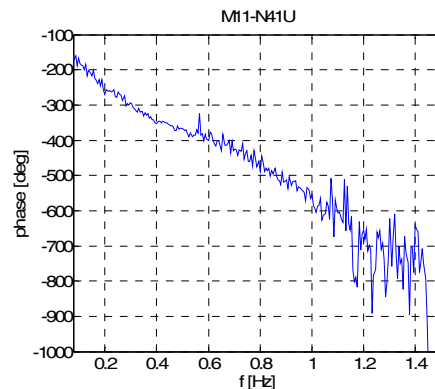


*Fig. 17 Phase between thermocouple M11 and ex-core detector N41 Upper as calculated from low-frequency measurements in Ringhals-3.*

passes through the core region. The validity of such a statement can be verified if the corresponding induced neutron noise is simulated and thereafter is compared with the measurements.

Such a complex perturbation can be modelled with two identical propagating perturbations travelling in opposite directions at some distance away from each other, i.e. one travels downstream in the downcomer and another one - upstream in the core region. Hypothetically, the presence of both signals in the measurements can lead to the appearance of a second slope in the phase spectra and, thus, to the second transit time. On the other hand, the neutron noise induced in the downcomer region can be considerably weaker than the one induced in the active part of the core and, therefore, can be undetectable. This hypothesis of existence of double transit time in PWR measurements will also be investigated in this section.

### 3.1. Measurement data

Two new sets of measurements were made and analysed in 2012 and 2014, respectively in order to understand the origin of the low frequency oscillations. In 2012 the 6 h measurements were taken in Ringhals-4 on 2012-08-09 with start 08:34:54, using a 4 Hz sample rate. In 2014, another set of 6 h measurements were performed on 2014-07-23

with start at 08:34:53 and a 4 Hz sampling rate. The set-up for both measurements was identical.

The core map with positions of the core-exit thermocouples (CET) and ex-core neutron detectors in the core, which was the same for both measurement sets, is shown in *Fig. 18*. The pairs of thermocouple-neutron detectors (radially close to each other) selected to perform the study are listed below:

- N41-CET-M11
- N41-CET-J12
- N42-CET-D3

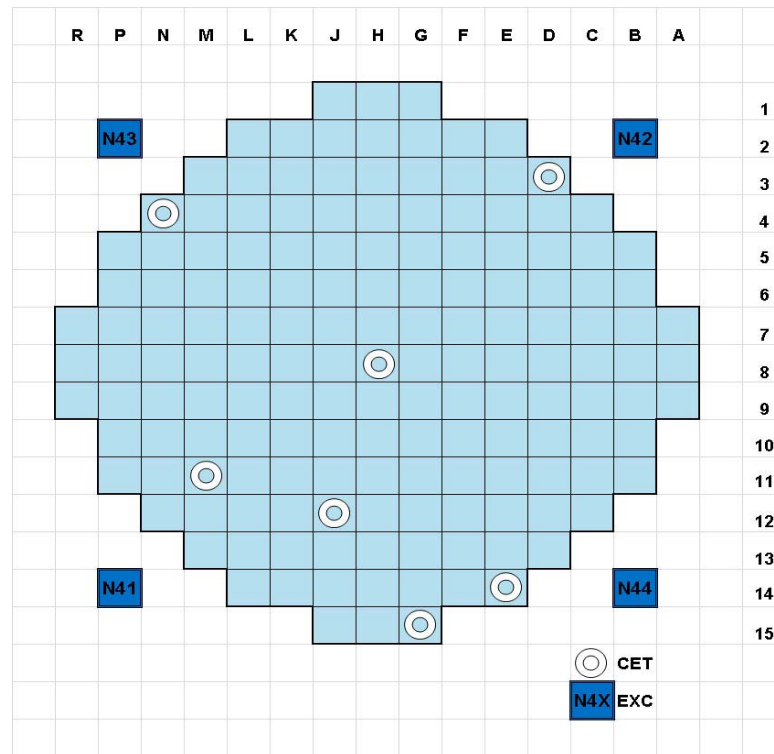


*Fig. 18 Core map showing the radial positions of the core-exit thermocouples (circles) and the positions of the ex-core neutron detectors(squares)*

- N43-CET-N4
- N44-CET-E14

In Stage 14 the analysis of measurements was planned to be done along two lines. Both of them were followed in 2012 whereas only one of them in 2014 (Signal Transmission Path Analysis, STPA). The first one was a cross-spectral and cross-correlation analysis of the selected ex-core detector–core exit thermocouple pairs. The motivation for this was to determine the radial coolant velocity between the corresponding

detector pairs. As it was noticed in the past [49], a tilted (asymmetric) radial distribution of the flow velocity, i.e. two quadrants having a slightly higher flow velocity than the other two, can lead to ultra-low frequency oscillations in which the role of the higher and lower velocity quadrants change with a very low frequency. More details on this topic are given in Stage 14. Thus, one task included into the present study was to test whether such a phenomenon takes place in Ringhals 3 and 4 by measuring the flow velocity in four quadrants.

### 3.2. Correlation analysis of the neutron noise measurements

In the following, a spectral analysis performed on different detector pairs is described. A more detailed study has already been presented in Stage 13 (however, it was made for much shorter measurements). Here, we only summarize the results obtained for the current measurements, in order to perform a qualitative comparison between these two cases. The selected detector pairs are:

- Pair N41U(L)-M11
- Pair N42U(L)-D3
- Pair N43U(L)-N4
- Pair N44U(L)-E14

In *Fig. 19-Fig. 22* the corresponding coherence functions together with their phases are plotted (in the left and right figures, respectively). These figures show that in the first three cases, the coherence between the upper/lower neutron detectors and the respective core exit thermocouples exhibits a similar behaviour, i.e. there is a wide peak ( $\sim 0.1-0.4$ ) in the frequency range between 0.2-0.6 Hz and much lower coherence ( $< 0.1$ ) in the ultra-low frequency region. Likewise, the phase behaviour resembles a strong linear dependence in the frequency range between 0.2-0.6 Hz and approaches a zero value below 0.1 Hz. The latter can be explained due to the strong effect of the reactivity noise which is usually dominating in this frequency region. Such a deterioration of the original signal by the global noise is especially visible in the case of a last detector pair (N44-E14), where both the coherence and the phase are very close to zero. Similar peaks and phase behaviour have also been observed in the earlier Stage 13. Applying the following linear fit

$$\varphi_{ij} = \tau_{ij}\omega + c_{ij} \quad (13)$$

to the phase of the CPSD, performed with a MATLAB built-in function “polyfit”, the transit time between different detector pairs can be obtained. In the above,  $i$  and  $j$  stand for the upper and lower detectors, respectively, and  $\tau_{ij}$  designates the slope of the phase which is equal to the corresponding transit time. In addition, the sign of the slope provides the information about the dominant flow direction, i.e. a “negative” sign corresponds to the upstream flow from  $j$  th-detector to  $i$  th -detector (since  $i$  th-detector detects the perturbation with some time-delay), whereas the “positive” sign indicates the downstream

flow from  $i$ th detector to  $j$ th detector. The results of such a fit, as well as the calculated transit times are presented in *Fig. 23* and *Table 1*, respectively. It should be pointed out here that the results for the last detector pair are not given here, since due to a very low coherence, the estimation of the transit time by the fitting procedure for such a case becomes almost impossible and leads to erroneous and unphysical values. From *Table 1*, it can be noted that in all three cases, the estimated transit time is around 1.2–1.8 seconds. This is a reasonably good estimate if one takes into account that the transit time of the coolant in the R4 core is around 1.4 s for coolant velocity 4.6–5 m/s and core height 3.6 m. Compared to the previous results presented in *Stage 13*, it is seen that the estimation of transit time is very close to the results obtained earlier.

Yet another interesting result which can be noticed from *Table 1* is a shorter transit time calculated between the thermocouple and upper neutron detector as compared to the one estimated between the same thermocouple and corresponding lower neutron detector. One possible reason for such a result might be a numerical uncertainty in the applied fitting procedure. Another possible explanation is based on the assumption that the neutron detector only detects the in-core perturbation which propagates upwards with a coolant.

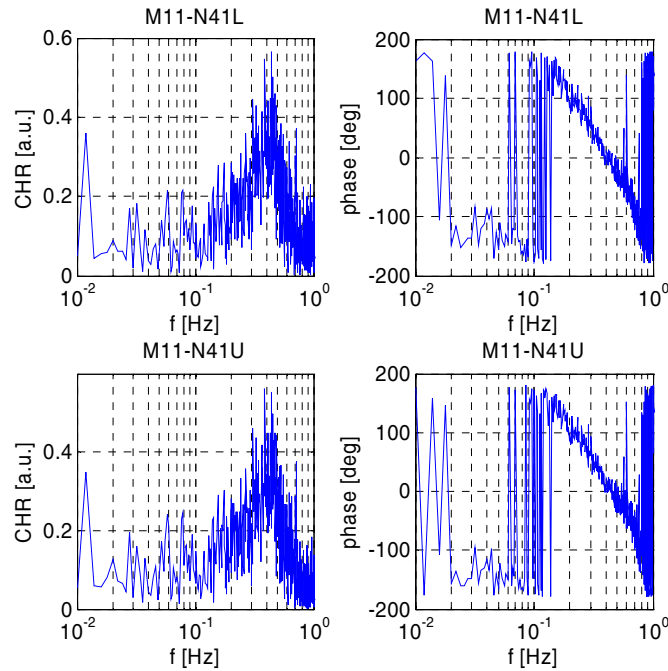


*Fig. 19 Coherence and phase between thermocouple M11 and ex-core detector N41*

The validity of this latter phenomenon is also planned to be investigated in the continuation.

Finally, for comparison, the coherence and phase functions calculated for different thermocouple pairs are also shown in *Fig. 24*. Obviously, there is not any visible correlation between the thermocouple signals.



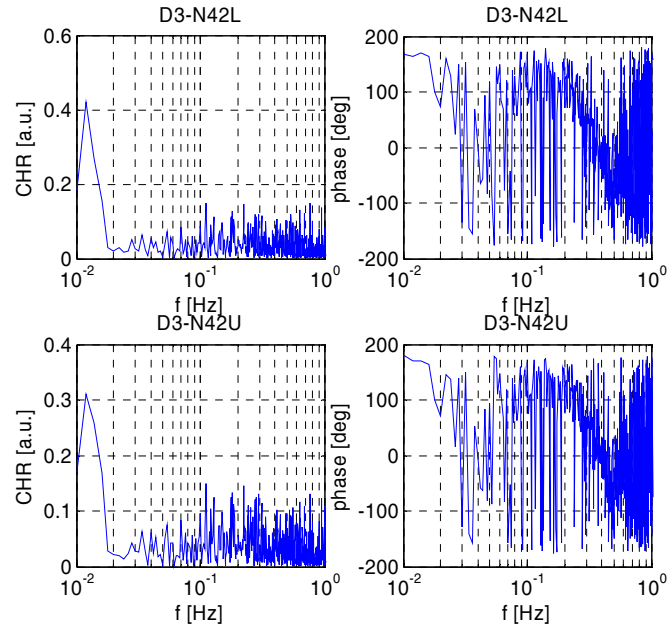


Fig. 20 Coherence and phase between thermocouple D3 and ex-core detector N42

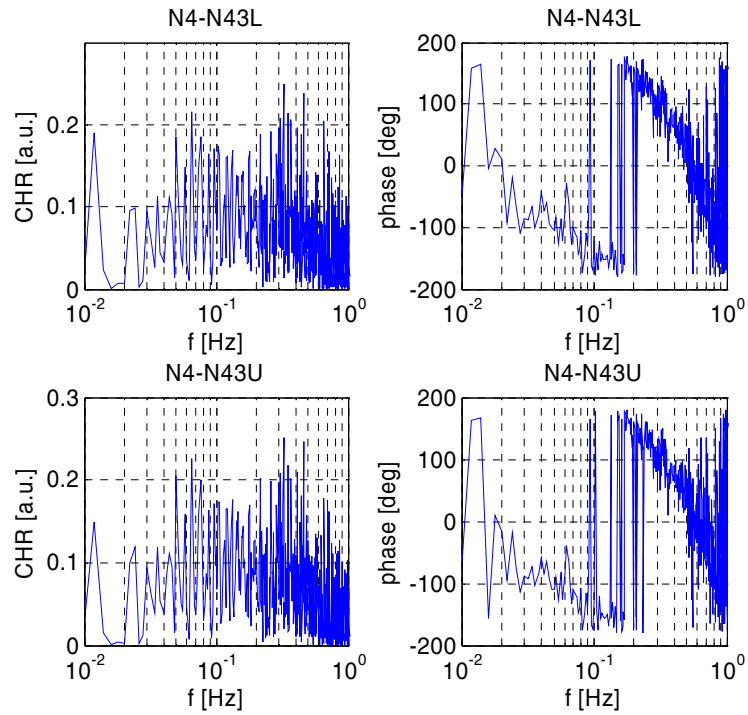


Fig. 21 Coherence and phase between thermocouple N4 and ex-core detector N43

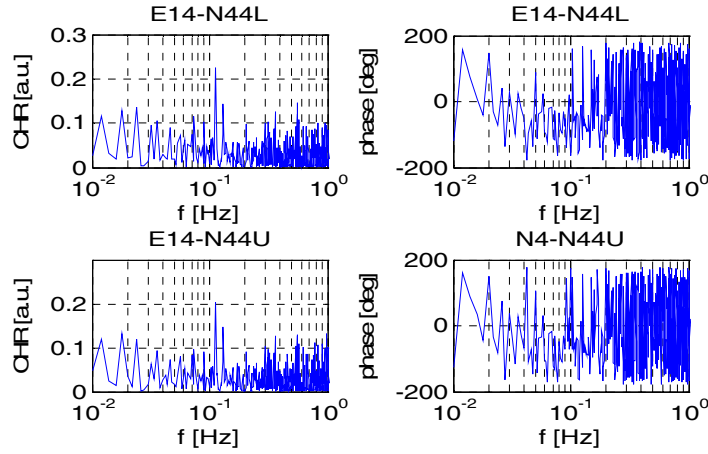


Fig. 22 Coherence and phase between thermocouple E14 and ex-core detector N44

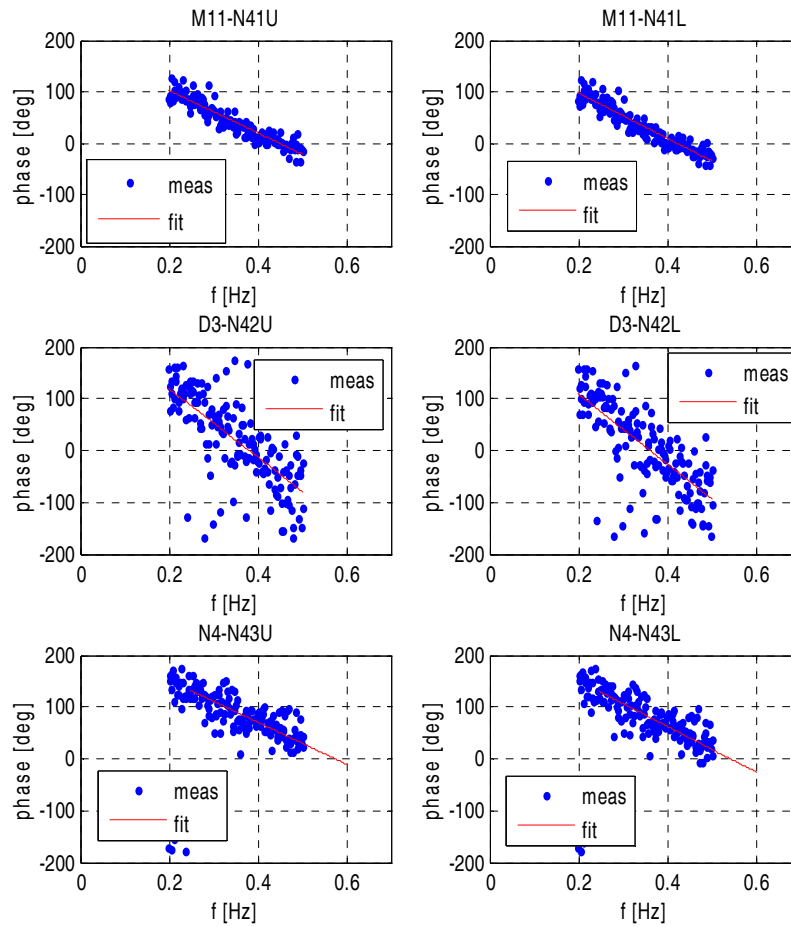
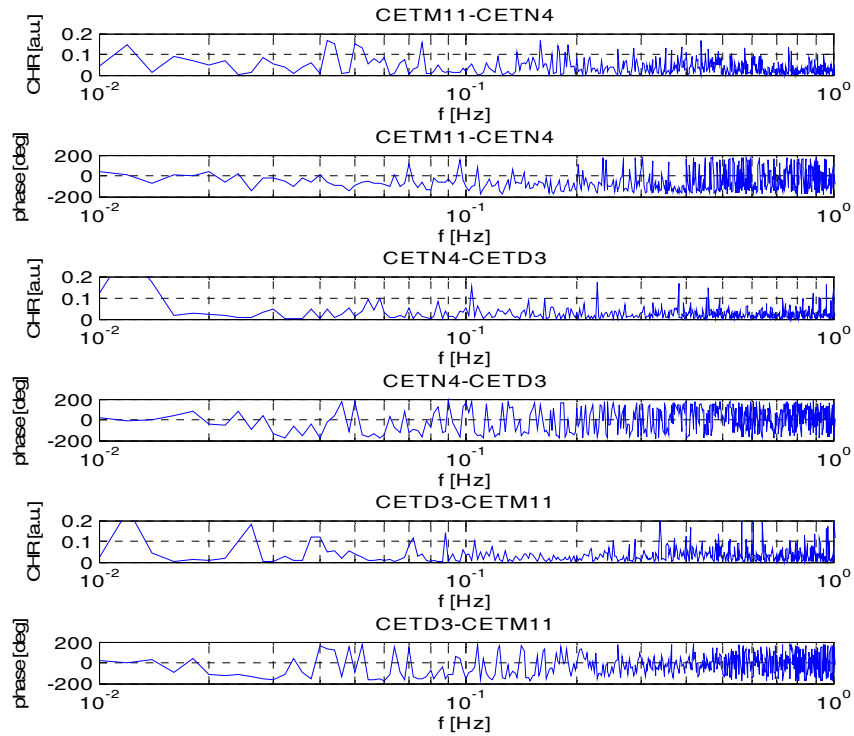


Fig. 23 Fitted phases between selected ex-core neutron detectors and thermocouples



**Table 1 Transit times calculated from the slopes of the phases between ex-core detectors and core-exit thermocouple.**

Detector pairs	Slope of the phase [deg/Hz]	Transit time [s]
M11-N41L	-440.9	1.225
M11-N41U	-412.1	1.145
D3-N42L	-673.0	1.870
D3-N42U	-661.5	1.838
N4-N43L	-440.6	1.224
N4-N43U	-405.0	1.125



*Fig. 24 Coherence and phase between selected pairs of thermocouples.*

### 3.3. Signal Transmission Path Analysis

The STP analysis was applied to two measurement sets taken in 2012 and 2014. The results of the analysis for both of them will be summarized here. First, a detailed analysis of the data set from 2012 will be presented which will be followed by a brief analysis of the second set, in order to notify the similarities and differences between two measurements as well as different trends within the measured period.

As a first step, the STP analysis is shown for only two detectors signals taken in 2012, i.e. for one ex-core neutron detector and one core-exit thermocouple detector. The selected detectors are designated as N42U and D3, respectively. Thereafter, attention will be paid to a more complicated case, when three detector signals are involved (one ex-core neutron detector and two core-exit thermocouples).

As a starting point, one first needs to specify the frequency range to be analyzed, which contains all frequencies of interest [46], [47]. For this purpose, in *Fig. 25* APSDs (Auto Power Spectral Density) for both detector signals N42U and D3 are shown. As *Fig. 25* shows, there are two different low-frequency regions that can be selected. The one is around 0.2-0.8 Hz (further referred to as “low frequency” region) and another one far

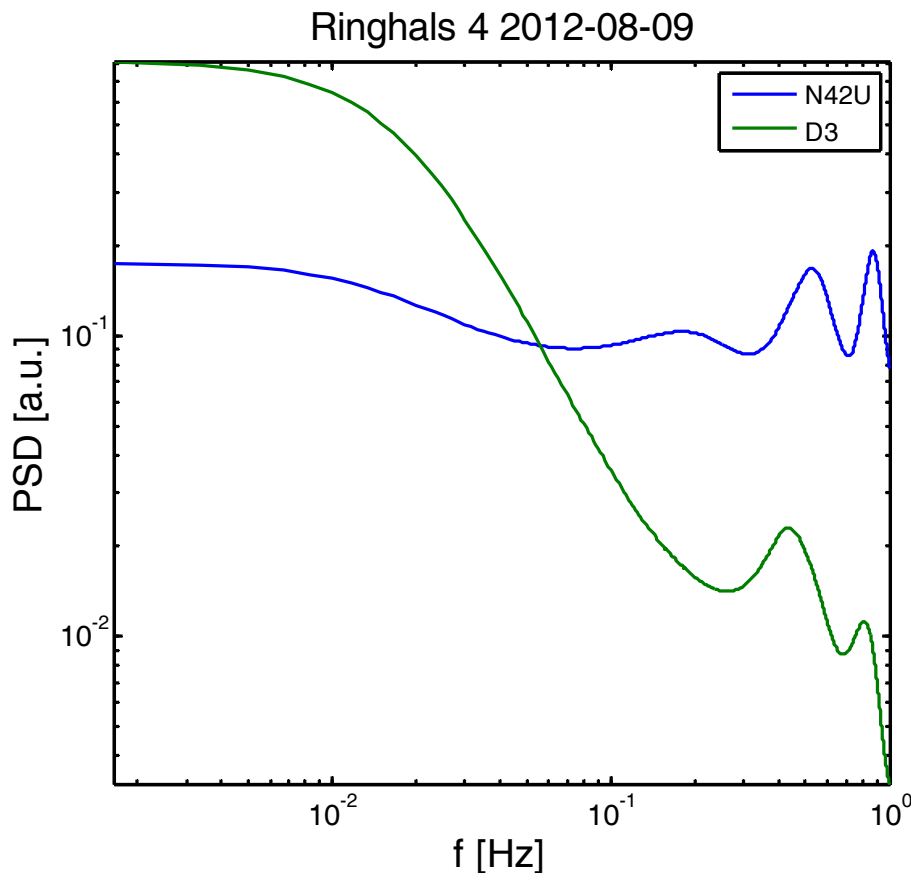


*Fig. 25 APSD of ex-core detector N42U and thermocouple D3 (2012)*

below 0.1 Hz (further referred to as “ultra low-frequency” region). Both regions will be analyzed in the present study; however, the main attention will be paid to the analysis of the latter one. As a next step, in order to identify different contributions from different noise sources into the corresponding APSDs, the so-called NPC (Noise Power Contribution) function for both detectors is plotted in *Fig. 26*. The main advantage of the NPC approach is that it allows to decompose the APSD of the measured signal (which represents some physical quantity) into contributions of different noise sources driving this quantity, as well as to identify the dominant noise source. Thus, comparing the APSD of DET N42U with the corresponding NPC function (upper part of *Fig. 26*), one can conclude that the induced neutron noise is mostly due to the fluctuations in the ex-core neutron detector signal itself with a small additional contribution coming from the core-exit thermocouple signal primarily in the ultra-low frequency region. A similar analysis is then applied to the second detector signal (CET-D3), which leads to the conclusion that the core-exit thermocouple APSD is strongly influenced only by the original noise source. In this case, the contribution from the DET N42U is relatively small and becomes visible only in low frequency region. Since the NPC function contains contributions from all existing noise sources (signals) (i.e. information about the power transmission through all possible STPs), it is usually not applicable to identify the type of the path (direct or indirect) which transmits signal power (APSD) from one quantity (signal) into another one. In order to see a direct effect between the selected signals, another group of functions, called PCH (Partial Coherence) and PNPC (Partial Noise Power Contribution) should be analysed. The first function (i.e. PCH) is usually used to quantify the direct correlation between the signals when all effects from other variables are excluded. The second function, i.e. PNPC provides the information about both direct and indirect coupling between two variables when any other contributions are eliminated. Therefore, the combined analysis of these two functions enables to evaluate the direct/indirect correlations in an explicit manner. The main principles of this method can be formulated in the following way [47]:

- a) if both functions are zero for the frequencies of interest, then there is no direct STP between two signals;
- b) if there is a direct STP between two signals, then one of the PNPC ratios follows the PCH behaviour in one direction and approaches zero in the opposite direction;
- c) if there are bilateral STPs between two signals, then PNPC ratios for both directions of signal flow take a value between zero and unity for the corresponding frequency range.

Such an analysis is especially interesting for the cases with a large number of possible noise sources, since it allows to separate the direct and indirect STPs (feedback) in a straight-forward way. For this purpose, both functions (PCH and PNPC) are plotted in *Fig. 27*. Here it should be pointed out that the values of both PCH and PNPC are very small which makes it difficult to draw any solid conclusions from STP analysis. Nevertheless, as one can see from this figure, there is one direct transmission path from D3 to N42U, which can be detected in the ultra-low frequency region, and one STP from N42U to D3 in the low frequency region. These results fully agree with the ones obtained earlier from APSD-NPC analysis. To this end, from the above analysis, one can conclude that in this particular case both detector signals CET-D3 and DET-N42U are almost uncorrelated and driven by their original noise sources. Nevertheless, some small correlation between two detectors signals resulting in the two above-mentioned direct STPs, one from D3 to N42U and another one from N43U to D3 in the ultra-low/low frequencies, respectively, still can be identified.

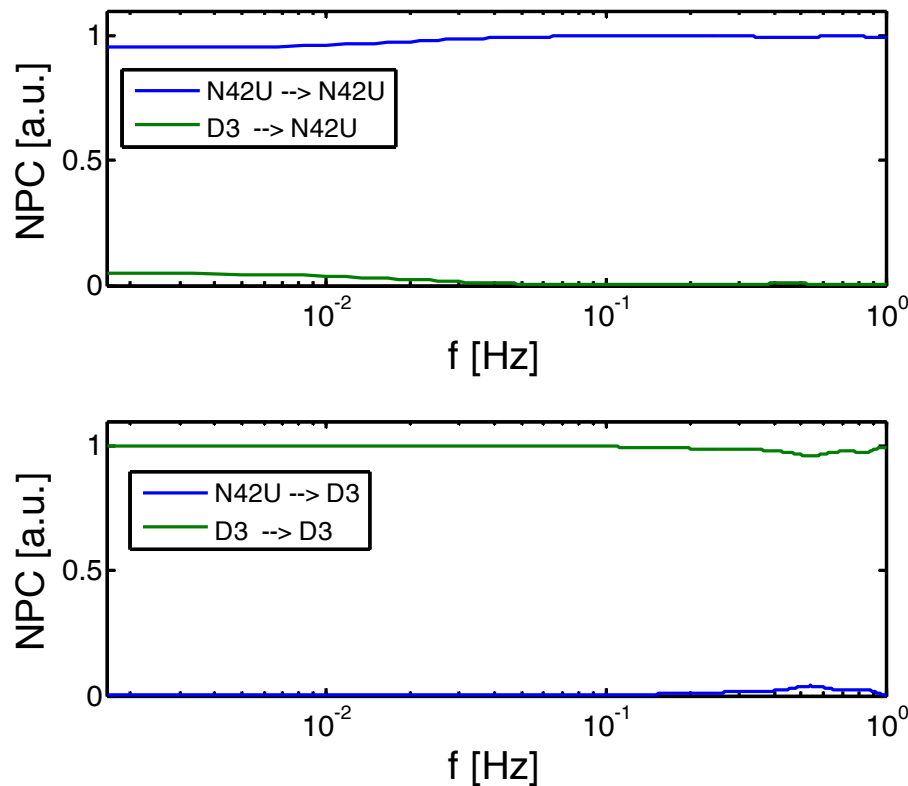


*Fig. 26 NPC of ex-core detectors N42U and thermocouple D3 (2012)*

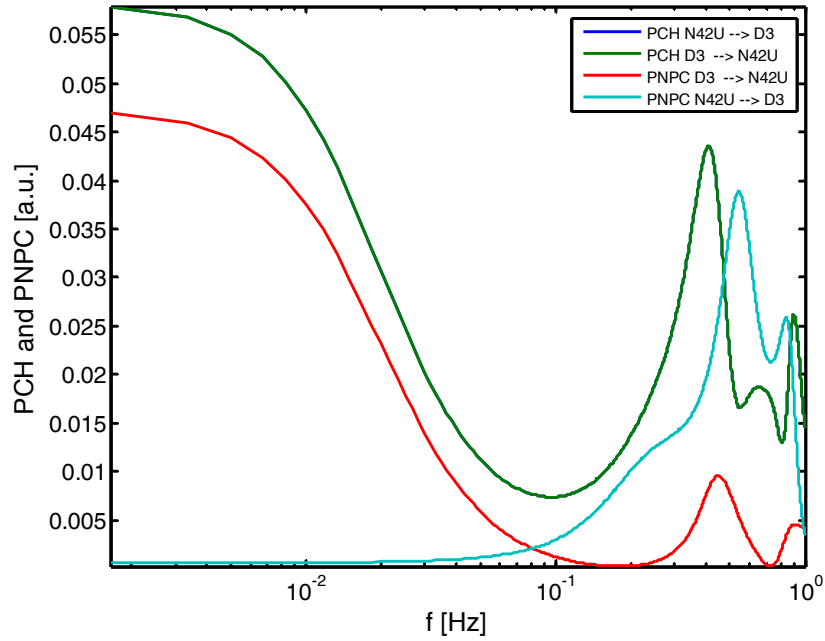


Fig. 27 PCH and PNPC of ex-core detectors N42U and thermocouple D3 (green and blue curves coincide with each other, 2012)

Some additional information about the time delay between two signals can also be obtained from the phase of PNC (see Fig. 28).

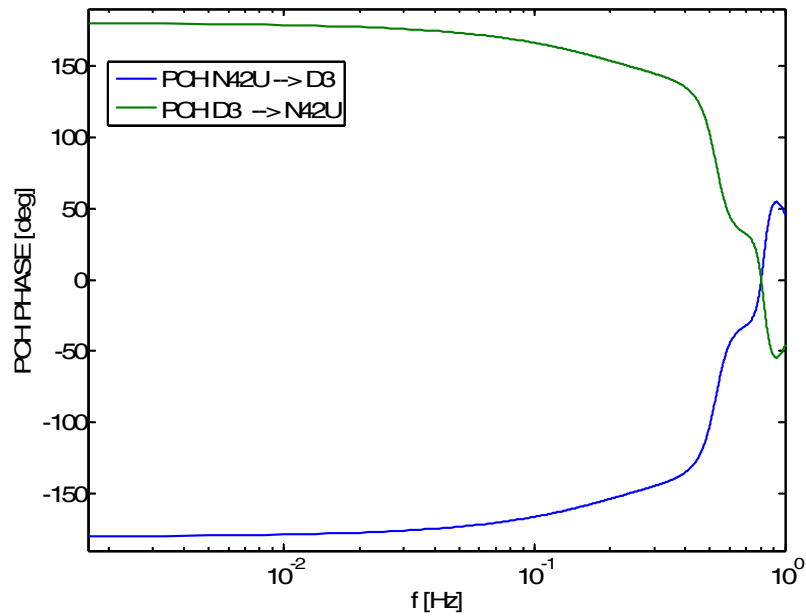


Fig. 28 PCH phase of ex-core detector N42U and thermocouple D3 (2012)

Further, a case with three detector signals is analysed. The selected detectors are one ex-core neutron detector N41L and two exit thermocouples M11 (close to N41L) and H8 (at the core centre). Following the same procedure as was described above, we first examine the APSD functions for each of three selected detector signals in order to identify the regions of interest. The corresponding APSDs for all three signals are plotted in *Fig. 29*. Similar to the previous case with two detectors, there are two frequency regions of interest selected for the analysis, i.e. ultra-low and low frequency regions, correspondingly. The respective NPC functions are shown in *Fig. 30*. Combining the APSD of DET N41L with the corresponding NPC function, one can notice that for ultra-low frequencies, the main contribution into the APSD comes from the fluctuations in the H8 detector signal, whereas the low-frequency part of the APSD is presumably affected only by the signal itself. From the comparison between the APSD and NPC of CET M11, one can conclude that the low-frequency APSD fluctuations are primarily induced by the ones from lower ex-core neutron detector N41L. On the other hand, the ultra-low frequency part of the APSD is apparently controlled by only the original signal itself. Applying a similar approach to the third detector, it is seen that for all frequencies of interest, the oscillations in DET N41L are mainly due to the fluctuations in CET H8, with a slightly increasing contribution from CET M11 in the intermediate frequency region. The analysis of corresponding PCH and PNPC functions (shown in *Fig. 31*) will then provide the information about possible transition paths between different detector pairs. As *Fig. 31* (upper left figure) shows, there is one direct STP from DET N41L to CET M11 for low frequencies where both PCH and PNPC functions are different from zero in the respective frequency region. In addition, one transition path from CET M11 to N41L can also be identified in the ultra-low frequency region (see *Fig. 31*, upper right figure).

The results for another core-exit thermocouple CET H8 combined with the same neutron detector are also shown in *Fig. 31* (middle figure). From this figure, it can be seen that the PCH and PNPC exhibit similar behaviour in the causal direction from DET-N41L to CET H8 and the PNPC is almost zero in the opposite direction for low frequencies of interest. However, the situation is slightly different for ultra-low frequencies where both the PCH and PNPC are different from zero value in both directions. The latter indicates that there is probably a bilateral STP existing between two detector signals. In the same way, one can determine the STPs between two thermocouples M11 and H8. The results of this analysis are given in *Fig. 31* (lower figure). As it is shown in this figure, there is a bilateral STP between the APSDs of CET H8 and CET M11 in the low frequency region, and no STPs can be detected for ultra-low frequencies.

To summarise, from the NPC and PCH-PNPC analysis demonstrated above together with *Fig. 29*, the following conclusions about STPs (or feedbacks) between different detectors and their possible noise sources can be drawn:

- a) for low frequencies: 1) oscillations in DET N41L are mainly driven by the signal itself (or any other sources which were not taken into account during this study); 2) oscillations in CET H8 are partly caused by DET N41L and

partly by the signal itself (a small contribution coming from CET-M11 can also be pointed out). 3) CET-M11 signal is partly influenced by DET N41L and partly by the original signal (a small contribution coming from CET-H8 can also be pointed out).

- b) for ultra-low frequencies: 1) oscillations in DET N41L are induced by H8 thermocouple signal; 2) H8 oscillations are partly controlled by DET N41L and partly by some other noise sources; 3) M11 signal is affected by only the signal itself (or some other sources not included in this investigation).

The corresponding phases of NPC functions are presented in *Fig. 32*.

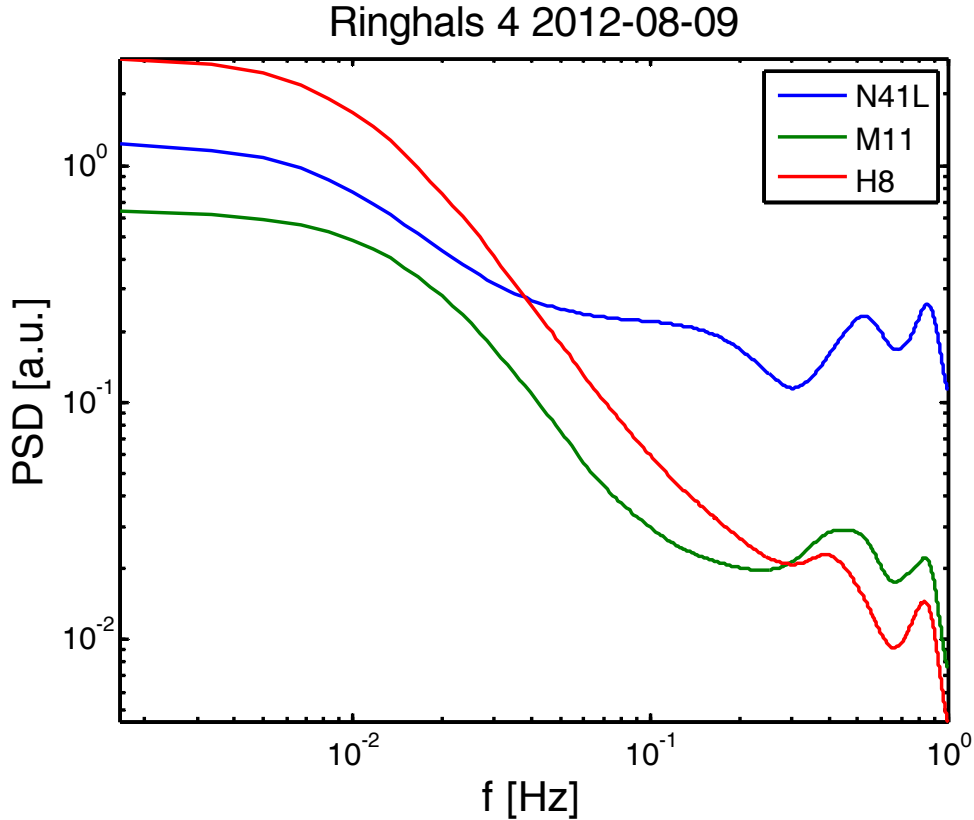


*Fig. 29 APSD of ex-core detector N41L and thermocouples M11, H8 (2012)*

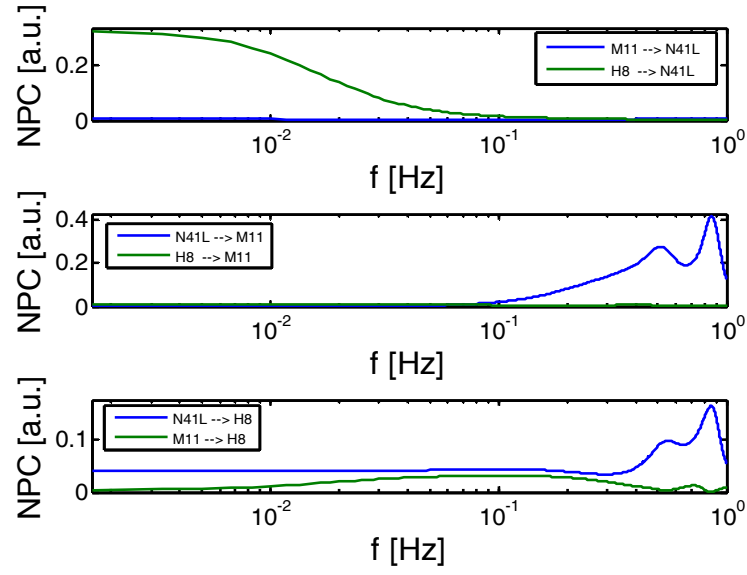


Fig. 30 NPC of ex-core detector N41L and thermocouples M11, H8 (2012)

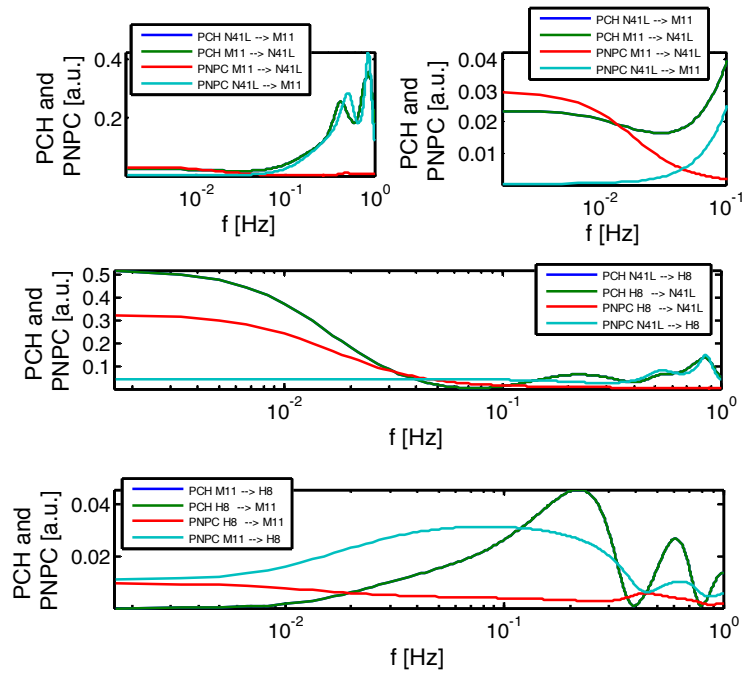
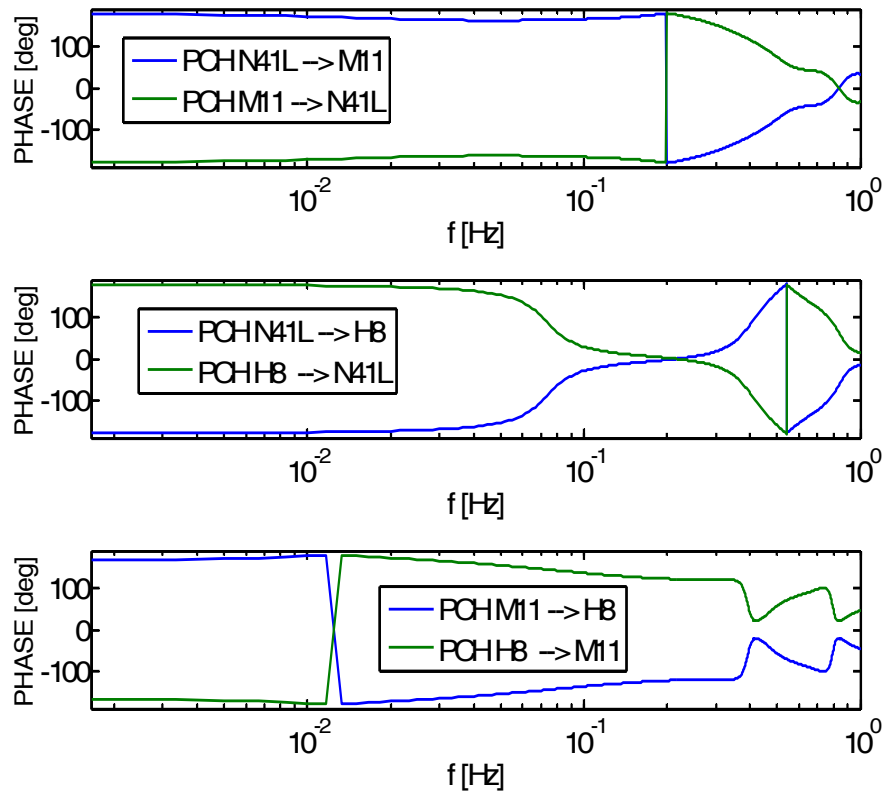


Fig. 31 PCH and PNPC of ex-core detector N41L and thermocouples M11, H8 (green and blue curves coincide with each other, 2012)



Here, it should also be underlined, that the current STPA is based on a linear AR (Auto Regressive) modelling which assumes that all noise sources are uncorrelated. In order to validate this assumption the ACF (Auto Correlation Function) of residual time signals (i.e. the difference between the AR modelled signals and the original ones) should be investigated. The respective ACF functions for all four detectors are demonstrated in *Fig. 33*. From *Fig. 33* it can be noticed that all ACFs are almost zero for all time lags, thus justifying the above assumption.



*Fig. 32 PCH phase of ex-core detector N41L and thermocouples M11, H8 (2012)*

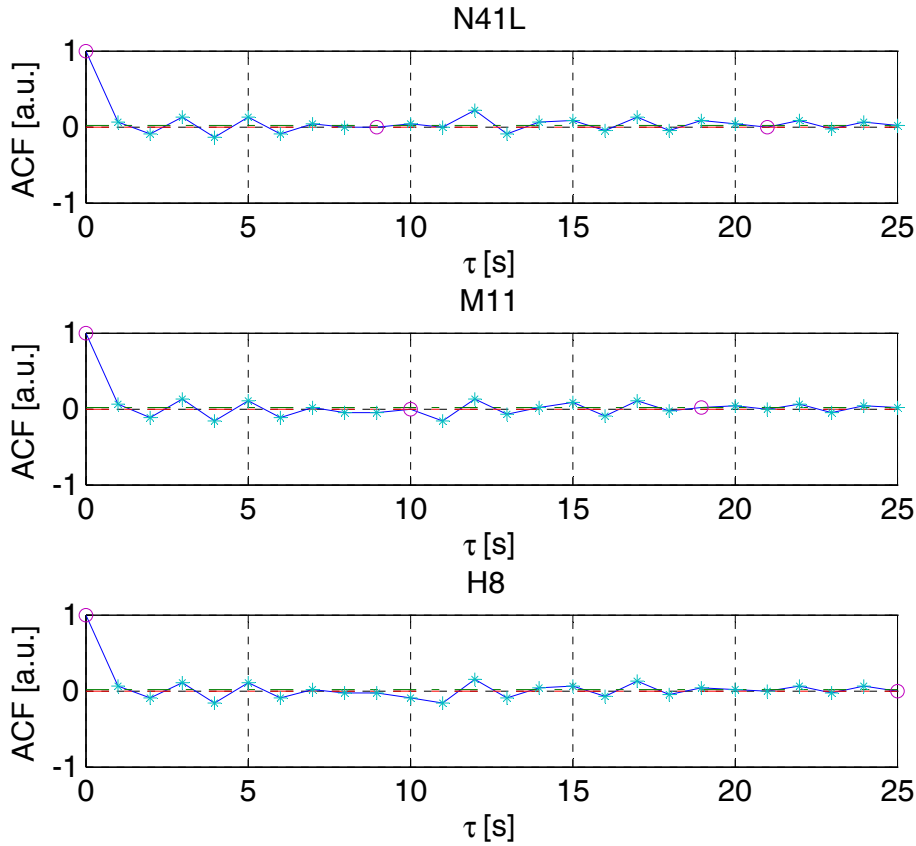


*Fig. 33 ACF of residual signals of ex-core detector N41l and thermocouples M11, H8 (2012)*

Further the results of the analysis of the measurements taken in 2014 are given. The PSD, NPC, PCH-PNPC for two and three detector signals are shown respectively in *Fig. 34-Fig. 37* and *Fig. 39-Fig. 42*. As can be seen from these figures, the results show certain changes in the curve characteristics between 2012 and 2014. In particular, the amplitude factors of various functions are different in the measurements taken in 2012 and 2014. In addition, comparing *Fig. 31* with *Fig. 40* it can be noticed that one of the STPs (from M11 to N41L) earlier observed in 2012 is missing in 2014 since the amplitudes of both PCH and PNPC are almost zero in ultra-low frequency region.

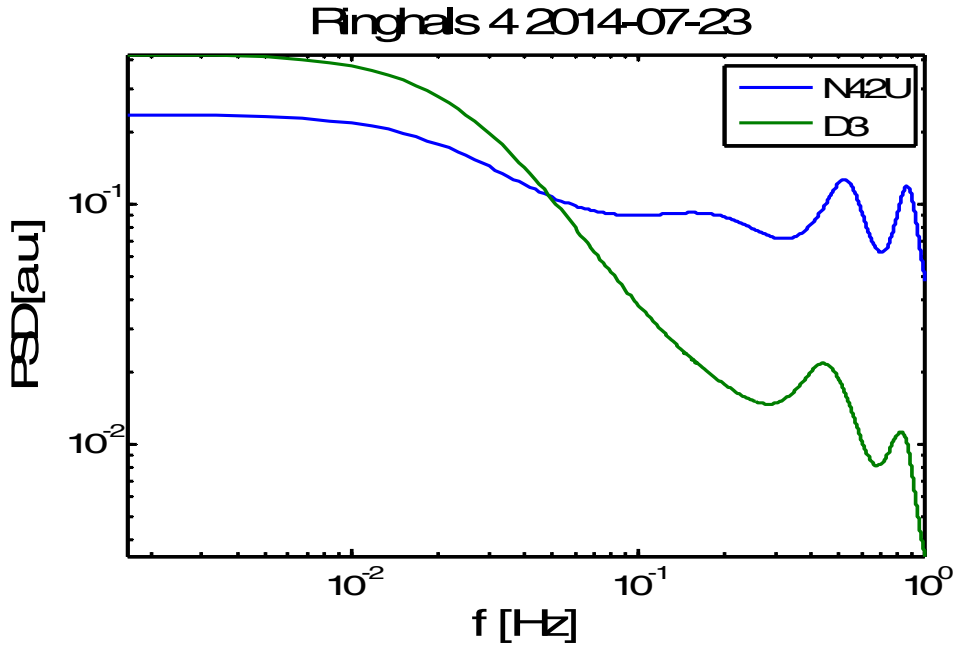


Fig. 34 APSD of ex-core detector N42U and thermocouple D3 (2014)

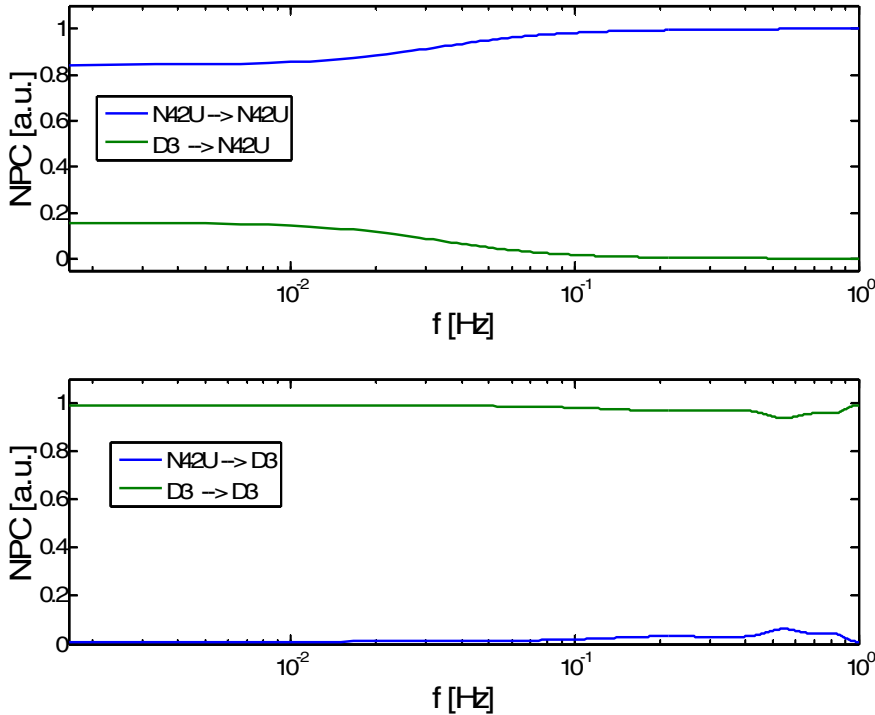


Fig. 35 NPC of ex-core detectors N42U and thermocouple D3 (2014)

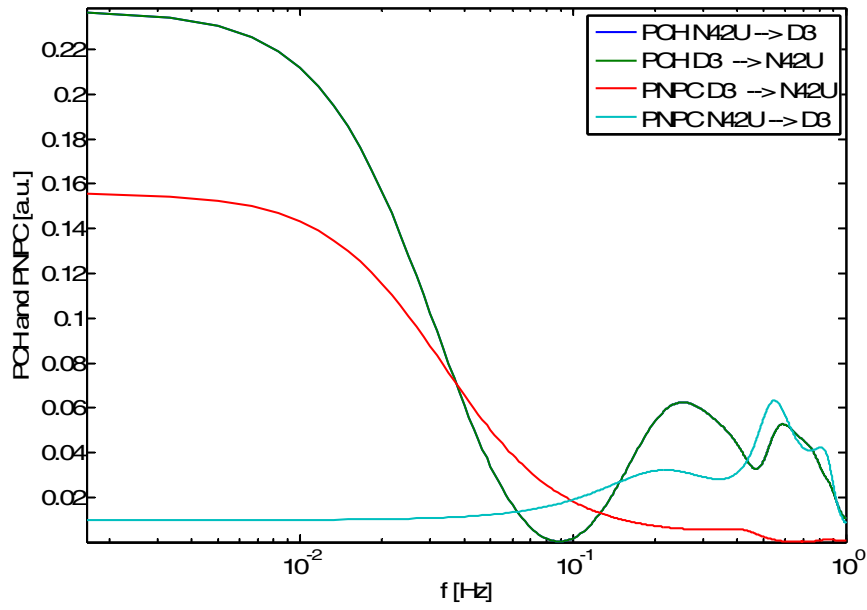


Fig. 36 PCH and PNPC of ex-core detectors N42U and thermocouple D3 (green and blue curves coincide with each other, 2014)

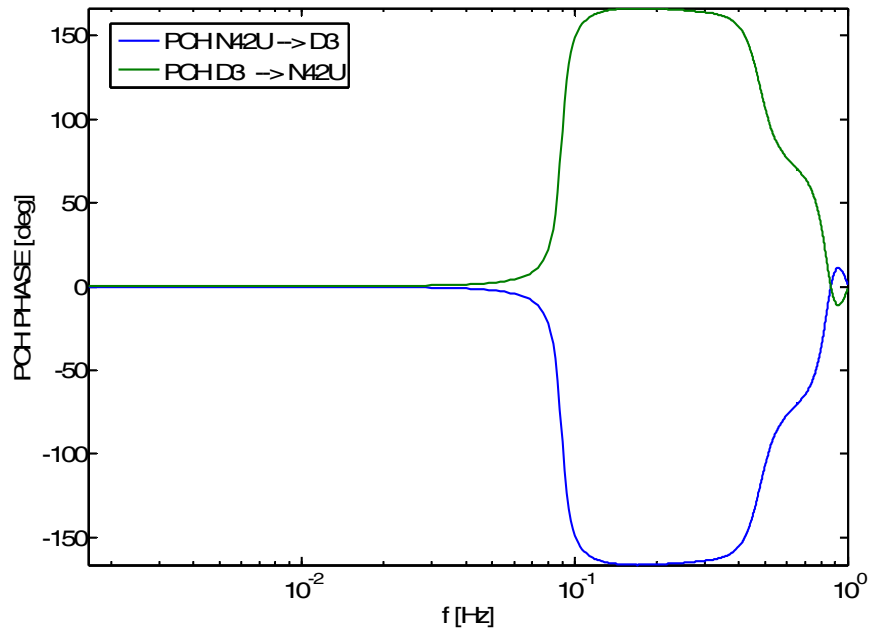


Fig. 37 PCH phase of ex-core detector N42U and thermocouple D3 (2014)

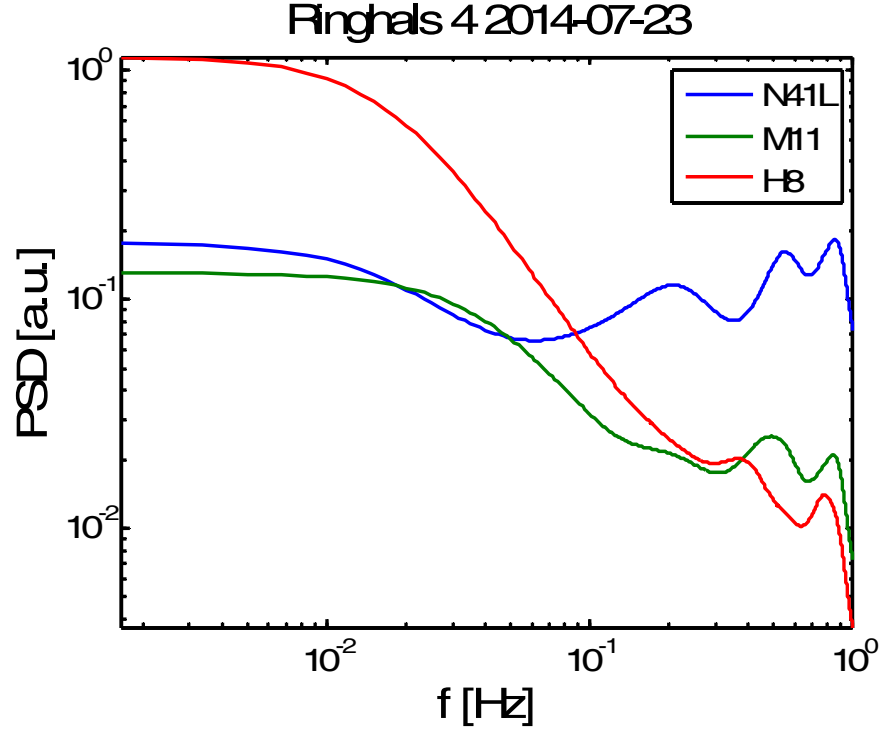


Fig. 38 APSD of ex-core detector N41L and thermocouples M11, H8 (2014)

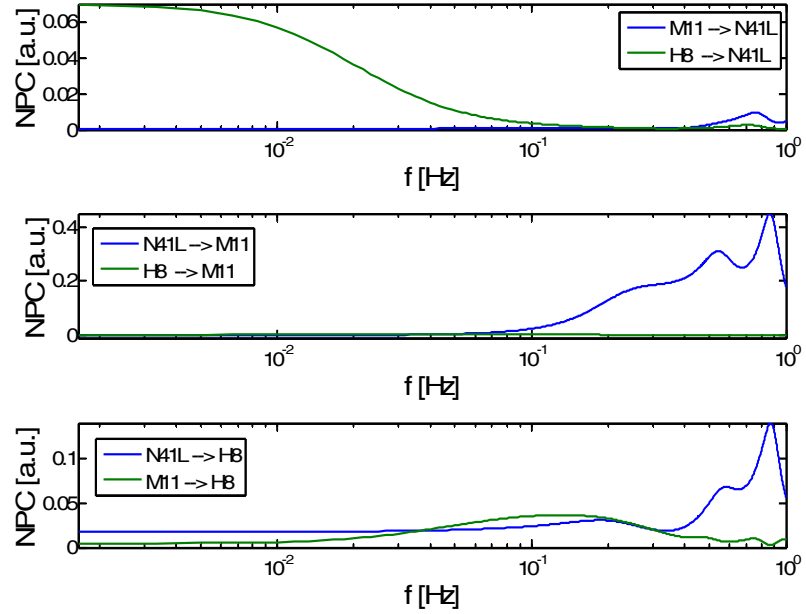


Fig. 39 NPC of ex-core detector N41L and thermocouples M11, H8 (2014)

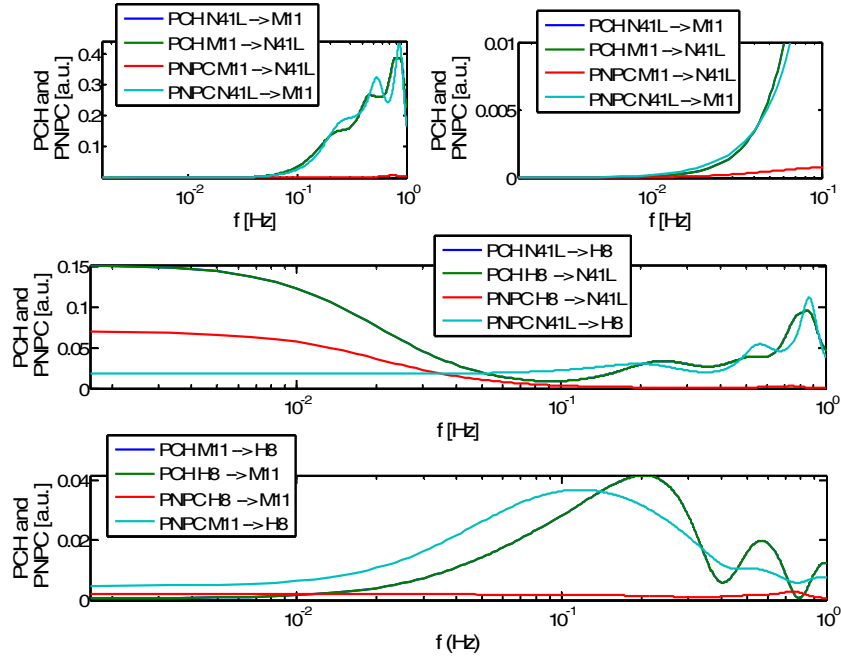


Fig. 40 PCH and PNPC of ex-core detector N41L and thermocouples M11, H8 (green and blue curves coincide with each other) (2014)

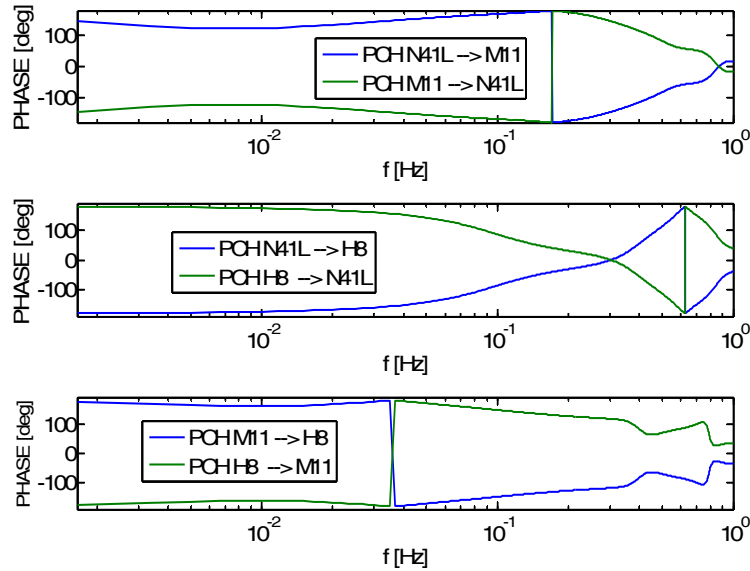


Fig. 41 PCH phase of ex-core detector N41L and thermocouples M11, H8 (2014)

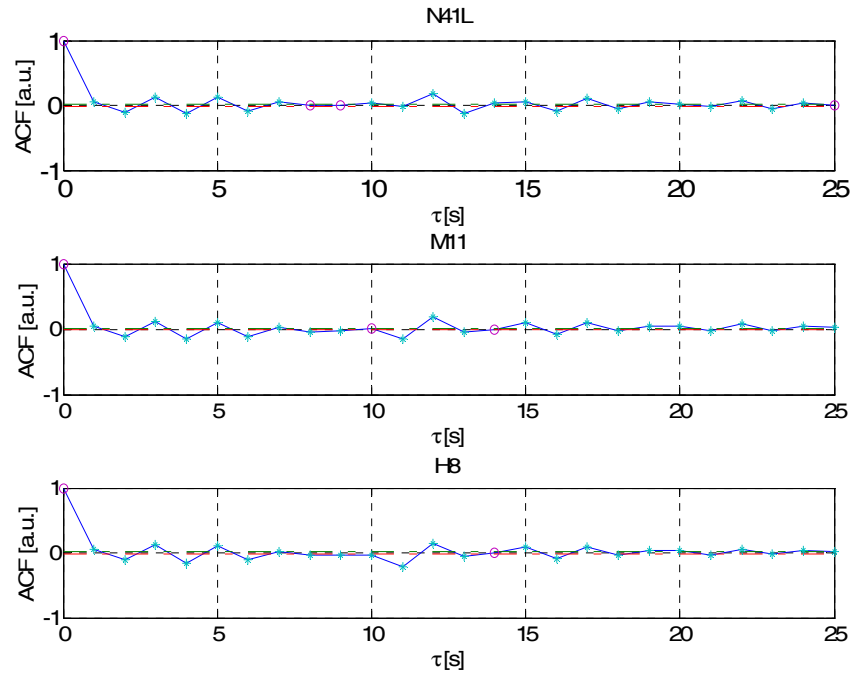


Fig. 42 ACF of residual signals of ex-core detector N41L and thermocouples M11, H8 (2014)

### 3.4. Conclusions

The ordinary coherence analysis, performed between different combinations of detector signals (ex-core neutron detector-core exit thermocouple), allowed to estimate the transit time of the coolant in three different quadrants of the core. Further analysis of these transit times indicated that there is a clear asymmetry in the radial flow distribution between different parts of the core with the lowest flow rate being in the upper right quadrant (N42) and with equally high flow rate in the upper and lower left quadrants (N41 and N43, respectively) (see Fig. 18). The latter result partly supports the earlier suggested hypothesis about the origin of low frequency oscillations observed in Ringhals 4. However, in order to ensure that such an asymmetric flow distribution oscillates with ultralow frequencies, an additional inspection of detector signals is necessary. From a physical point-of-view, it is clear that any changes in the radial flow distribution with time should also lead to the corresponding periodical changes in some of the characteristics of time-dependent signals, measured by neutron detectors/thermocouples (for example, their mean values). Therefore, as a further step, it is reasonable to perform a similar coherence analysis for different parts of the same signal separately (where its properties do not change much), in order to estimate the flow velocities corresponding to the selected time intervals of the original signal. Such an investigation will be undertaken in the continuation. Furthermore, it might also be useful to apply a similar coherence analysis for

a new set of measurements taken in 2014 such that the discovered flow pattern can be verified. Such an analysis is planned to be done in the future.

From the STP-analysis performed in 2012, some correlation between ex-core neutron detector and core exit thermocouple measurements was found which leads to the conclusion that for ultra-low frequencies the neutron noise is most likely driven by the temperature fluctuations. However, this is not the case for the low frequency region where the situation becomes reverse, i.e. the fluctuations in thermocouple signals (or temperature fluctuations) are apparently caused by the fluctuations in corresponding neutron detector signals (or neutron noise) which in their turn are induced by some other external sources. In order to draw final conclusions about transmission paths between different detector signals, all possible detector pairs should be analyzed. In 2014 another set of measurements was analysed which verified the tendencies found in 2012. However, no conclusive explanations about the origin of low frequency oscillations can be drawn from STP analysis.

### 3.5. Double transit time in PWR measurements.

#### 3.5.1. Calculation of the noise induced by two propagating perturbations travelling with the same velocity in opposite directions.

In order to calculate the neutron noise induced by a propagating perturbation, the noise source  $S(z, \omega)$  should first be specified. In the present study, the noise source is selected as an axially propagating perturbation of the absorption cross-section  $\delta\Sigma_a(z, \omega)$  induced by density or temperature fluctuations in the coolant of a PWR, which in the frequency domain conventionally reads as:

$$\delta\Sigma_a(z, \omega) = \delta\Sigma_a(0, \omega) \exp\left(-\frac{i\omega}{v} z\right) \quad (14)$$

where  $v$  stands for the propagating velocity. Then, for the neutron noise source in one-dimension the first order perturbation theory yields

$$S(z, \omega) = \frac{\phi_0(z) \delta\Sigma_a(z, \omega)}{D} \cong S_0 \phi_0(z) \exp\left(-\frac{i\omega}{v} z\right), \quad (15)$$

where  $S_0$  is a constant indicating the white noise character of the inlet noise. The neutron noise induced by the perturbation (15) can be calculated via the standard Green's function technique. In the present study, only the local component of the neutron noise will be considered and therefore, for simplicity, an exponential form of the Greens function will be used in the further calculations.

According to our hypothesis, the core exit thermocouple can detect only perturbations propagating upwards, whereas the (upper) neutron detector is able to see two propagating perturbations: one is travelling downwards and another one upwards. Therefore, in the calculations of the neutron noise induced in the ex-core neutron detector, two perturbations



similar to (15) but taken with opposite velocity signs will be utilized (notice that for the noise in the exit thermocouple only one perturbation in upstream direction is needed). The amplitudes of the selected perturbations are set to be different and defined correspondingly as  $A$  (for travelling downstream) and  $B$  (for travelling upstream). Here, it should be stressed that in a realistic case, a two dimensional model of the propagating noise should be considered since the two propagating perturbations travel at some distance away from each other (one in the downcomer and the other in the core) in two different radial positions and thus are integrated with different regions of the transfer function, with different spatial relaxation properties.

In the analysis performed in 2013, in order to keep the model simple enough, the second dimension was disregarded (a 2-dimensional case was considered in 2014 and will be discussed further on). Thus in the preliminary study in 2013, the two perturbations were convoluted with two different transfer functions (i.e. Greens functions) which have different relaxation properties, i.e. two different relaxation lengths  $\lambda_{ds}$  and  $\lambda_{us}$  in the corresponding exponential functions. Then, for the normalized neutron noise induced in the core exit thermocouple  $CET - M11$  and in the (upper) neutron detector  $N41U$ , one correspondingly gets:

$$\frac{\delta T_{CET-M11}^m(z, \omega)}{T_0^m(z)} = \frac{D}{1 + (\omega \lambda_f)^2} \exp\left(\frac{i\omega}{v} z\right), \quad (16)$$

$$\begin{aligned} \frac{\delta \phi_{N41U}^l(z, \omega)}{\phi_0(z)} &= C_{ds} A \int_0^H \exp(-(\lambda_{ds} |z - z'| - \frac{i\omega}{v} z') dz' + C_{us} B \int_0^H \exp(-(\lambda_{us} |z - z'| + \frac{i\omega}{v} z') dz' \\ &= \frac{C_{ds} A}{1 + (\omega \lambda_{ds})^2} \exp(-\frac{i\omega}{v} z) + \frac{C_{us} B}{1 + (\omega \lambda_{us})^2} \exp(\frac{i\omega}{v} z), \end{aligned} \quad (17)$$

where  $H$  is the axial height of the reactor core,  $T_0^m(z)$  stands for the steady-state temperature,  $D = \delta T^m(z = z_{inlet}, \omega) = C_{us} B$  is the fluctuation of the moderator temperature at the core entrance,  $\lambda_f$  being the time constant of the fuel,  $\phi_0(z)$  stands for the static flux

and  $C_{ds} = \frac{\Sigma_R - \Sigma_1 - D_1 \lambda_{ds}^2}{2D_1 D_2 \lambda_{ds}^3}$ ,  $C_{us} = \frac{\Sigma_R - \Sigma_1 - D_1 \lambda_{us}^2}{2D_1 D_2 \lambda_{us}^3}$  are the Greens function parameters

which depend on the system properties (cross-sections) [31]. In the above it was assumed that the static flux does not change much in the vicinity of the perturbation [31]. Finally, for the Cross-Power Spectral Density function (CPSD) calculated between one (upper) neutron detector  $N41U$  and one thermocouple  $CET - M11$  located at  $z_1$  and  $z_2$ , respectively, one obtains [31]:

$$\begin{aligned}
CPSD_{N41U-CETM11}(z_1, z_2, \omega) &= \frac{\delta\phi_{N41U}^l(z_1, \omega)}{\phi_0(z_1)} * \frac{\delta T_{CET-M11}^{m*}(z_2, \omega)}{T_0^m(z_2)} = \\
&= A1 * A2 * \exp(i(\varphi_1 + \varphi_2)),
\end{aligned} \tag{18}$$

where  $A1 = P(\omega) * \sqrt{1 + Q^2(\omega) + 2Q(\omega)\cos\varphi_1}$  and  $\varphi_1 = \arctan \frac{\sin(\alpha_1)}{\frac{1}{Q(\omega)} + \cos(\alpha_1)}$  with

$$\alpha_1 = -\omega\tau_2, \tau_1 = \frac{z_1 - z_2}{v}, \tau_2 = \frac{2z_1}{v}, A2 = 1 \text{ and } \varphi_2 = \omega\tau_2.$$

As can be seen from the derivation above,  $\varphi_2$  is a linear function in frequency with the slope  $\tau_2$  and  $\varphi_1$  is an oscillating function around a linear function with the slope  $\tau_1$  (similar to the case of BWR where the oscillating character of the CPSD phase was observed and interpreted due to the interplay between reactivity term and local component).

From Eq. (18) one can clearly see that the calculated CPSD has at least two different phases which may result in two different linear slopes (and thus in two different transit times) such as the ones observed previously in the measurements. The analysis of the calculated CPSD, in particular, its phase behaviour will be given in the next section.

The oscillating character of the phase of the CPSD can also be explained in a way it was done in the case of a BWR where the oscillating behaviour of the CPSD phase was also noticed and explained by the interplay between the reactivity and local components of the noise induced by propagating perturbation [61]. However, in the present case of a PWR, the origin of the oscillating phase is somewhat different from that of the BWR case. As it will be shown below, the oscillating behaviour of the phase is an inherent property of one of the detector signals, namely the one which senses both travelling perturbations (propagating in positive and negative directions) and is not related to the CPSD between the detector signals. The reason for such an unusual behaviour of the phase of the detector signal is obviously the simultaneous presence of two propagating perturbation travelling in opposite directions. The validity of such a statement is demonstrated below.

We start with Eq. (17) which describes the noise induced in the neutron detector N41U by two propagating perturbations and can be transformed in the following form:

$$\frac{\delta\phi_{N41U}^l(z, \omega)}{\phi_0(z)} = \frac{C_{ds} A}{1 + (\omega\lambda_{ds})^2} \left[ \exp\left(-\frac{i\omega}{v} z\right) + k \exp\left(\frac{i\omega}{v} z\right) \right] = Z * [R1 + R2] \tag{19}$$

where  $Z = \frac{C_{ds} A}{1 + (\omega \lambda_{ds})^2}$ ,  $R1 = (1 - k) * \exp(-\frac{i\omega}{v} z)$  and  $R2 = 2 * \cos(\frac{\omega}{v} z)$ . As Eq. (19)

shows, the detector signal N41U  $\frac{\delta\phi_{N41U}^l(z, \omega)}{\phi_0(z)}$  contains two terms  $R1$  and  $R2$  with

different amplitude and phase characteristics. The first term  $R1$  has a linear phase in frequency characterized by the slope  $\tau_l = \frac{z}{v}$ . The second terms  $R2$  (cosine function)

represents a harmonic (oscillating) function which has a periodic zero structure in the amplitude and periodic step-wise (constant) phase oscillating between 0 and  $\pi$ . In the points where  $R2$  is zero the total phase of  $\frac{\delta\phi_{N41U}^l(z, \omega)}{\phi_0(z)}$  coincides with a linear phase

of  $R1$ . Similar arguments were used to explain the oscillating behaviour of the phase in a BWR case mentioned earlier [50]. There the amplitude of the reactivity term had a similar zero structure as  $R2$  and did not contribute into the total phase at zero points. Therefore, the total phase in a BWR case coincided with a linear phase of another local component creating the oscillating character of the phase. In the points where  $R2$  is not zero, the total

phase of  $\frac{\delta\phi_{N41U}^l(z, \omega)}{\phi_0(z)}$  gains additional constant component (0 or  $\pi$ ) coming from  $R2$  and

thus creating an oscillating pattern of the phase. From the physical point of view, such unusual phase behaviour can be interpreted in the following way: if there are two similar perturbations in the system propagating in two opposite directions and having different amplitude weights, then at certain frequencies the weaker perturbation can be cancelled out by a part of the stronger perturbations. As a result, at those frequencies, the total phase of the signal is only driven by the strongest perturbation. Otherwise, the phase starts to deviate from the linear behaviour showing an oscillating pattern.

To make the study complete, an additional remark regarding the total phase of the CPSD should be done. As was shown above, the oscillating behaviour of the phase of the CPSD is due to the oscillating behaviour of the neutron detector signal N41U. As Eq.(18) shows, the CPSD represents the convolution between two detector signals: neutron detector signal N41U and complex conjugated thermocouple signal M11. From Eq. (16) it can be seen that the latter signals has a pure linear phase. Obviously the convolution between two signals both having a linear phase will again results in a signal with a linear phase. On the other hand, since one of the signals has an oscillating phase, such a pathological property will also be transferred into the total phase. It should be pointed out that in the present study the detector response time was not taken into account which obviously can also influence the shape of the total phase. Such a possibility will be investigated in the further studies.

Finally, the 2-dimensional case is considered below. Similarly to the 1-dimensional case, the normalized neutron noise induced by a propagating perturbation, Eq. (14), in the

core exit thermocouple  $CET - M11$  and in the (upper) neutron detector  $N41U$  read correspondingly as:

$$\frac{\delta T_{CET-M11}^m(x, z, \omega)}{T_0^m(x, z)} = \frac{D}{1 + (\omega \lambda_f)^2} \exp\left(\frac{i\omega}{v} z\right), \quad (20)$$

$$\begin{aligned} \frac{\delta \phi_{N41U}^l(x, z, \omega)}{\phi_0(x, z)} = & C_{ds} A \int_{-R}^R \int_0^H \exp\left(-(\lambda_{ds} \sqrt{(z - z')^2 + (x - x')^2} - \frac{i\omega}{v} z') dz' dx' + \right. \\ & \left. C_{us} B \int_{-R}^R \int_0^H \exp\left(-(\lambda_{us} \sqrt{(z - z')^2 + (x - x')^2} + \frac{i\omega}{v} z') dz' dx', \right. \end{aligned} \quad (21)$$

where  $R$  stands for the radius of the reactor core and  $D = \delta T^m(x = x_{inlet}, z = z_{inlet}, \omega) = C_{us} B$ . As can be seen from Eqs (20)-(21), in 2D case the expressions for the induced neutron noise is much more involved and can not be represented in a simple analytical form whereas only numerical treatment is possible. Then, for the Cross-Power Spectral Density function (CPSD) calculated between one (upper) neutron detector  $N41U$  and one thermocouple  $CET - M11$  located at  $(x_1, z_1)$  and  $(x_2, z_2)$ , respectively, one obtains:

$$CPSD_{N41U-CETM11}(x_1, x_2, z_1, z_2, \omega) = \frac{\delta \phi_{N41U}^l(x_1, z_1, \omega)}{\phi_0(x_1, z_1)} * \frac{\delta \phi_{CET-M11}^{*l}(x_2, z_2, \omega)}{\phi_0(x_2, z_2)}, \quad (22)$$

A more detailed analysis of the results for 2D case will be given in next section.

### 3.5.2. Results and discussion

The phase of the CPSD between one ex-core neutron detector and one core exit

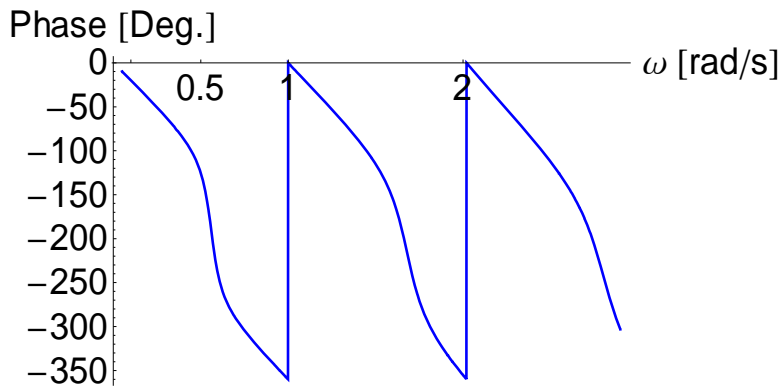
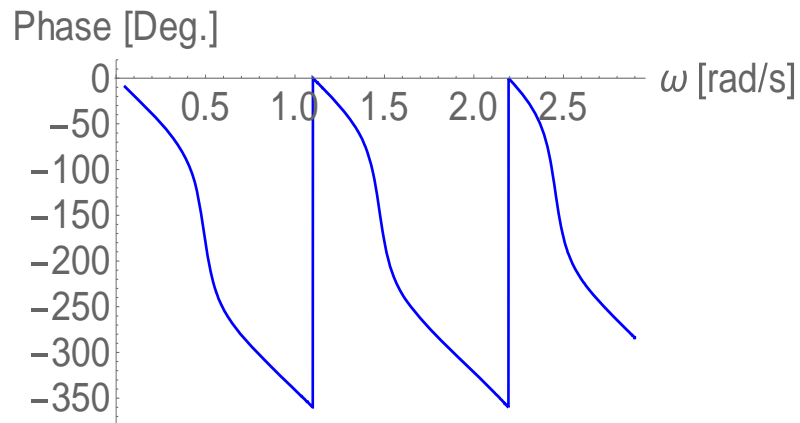


Fig. 43 Simulated phase of the CPSD calculated between thermocouple M11 and ex-core detector N41 Upper for the case of two perturbations propagating in opposite directions (1-dimensional model,  $A = 7.2 \cdot 10^{-5}$ ,  $B = 8.64 \cdot 10^{-5}$ ).

thermocouple calculated by the formulae derived in the previous section is plotted in *Fig. 43*. The corresponding parameters used in the simulation (for both 1D and 2D cases) are summarized in Table 2. Comparing this result with the phase obtained earlier from the measurements (see *Fig. 17*), several similarities can be pointed out. The main one is related to the behaviour of two phases in the low frequency region between 0.1-1 Hz where both phases show similar qualitative behaviour. As *Fig. 43* shows, in the frequency region of interest, the simulated phase does not have a constant slope but rather it changes with frequency showing at least two different slopes. These two slopes are apparently due to the presence of two perturbations propagating in two opposite directions. Although the two phases show a similar pattern, the convexity of the slopes of two curves are somewhat different, i.e. in the measurements the curve is convex between 0.1-0.5 Hz whereas in the simulation it is concave in the same frequency region. The amplitudes of the phase change (i.e. scaling factor) in both cases are also different. This latter mismatch can be related to the choice of the perturbations' relative strengths and their velocity directions. From these results, the hypothesis about the presence of two different slopes (and thus two different transit times) in the measured phase between 0.1-1 Hz gets some confirmation but more solid conclusions require additional investigations with a more sophisticated model and can not be obtained with the present simulations.

The results of the calculations for 2-dimensional case are given in *Fig. 44*. From the figure, it is seen that the behaviour of the phase is qualitatively identical with the results derived in 1D case. The clear presence of two distinct slopes and thus two different transit times can also be noticed in 2D case. Comparing these results, with real measurements shown in *Fig. 17*, similar conclusions as in 1D case can be drawn here. Thus, although the behaviour in both cases is similar, the exact reconstruction of the measurement pattern in terms of convexity of the slopes, number of the slopes and scaling factors was not performed. In particular, the scaling factors are far from being similar.



*Fig. 44 Simulated phase of the CPSD calculated between thermocouple M11 and ex-core detector N41 Upper for the case of two perturbations propagating in opposite directions 2-dimensional model,  $A = 7.2 \cdot 10^{-5}$ ,  $B = 6 \cdot 10^{-5}$ ).*

As was mentioned earlier, the observed difference can be explained due to inappropriately chosen scaling (amplitude) factors used for the perturbations. Therefore, in 2014 several additional attempts were undertaken to obtain the same amplitude factor in the simulated signals as in the measurements by adjusting the ratio between two neutron noise sources as in the measurement but were not successful. Apparently, the reason for such a strange behaviour of the phase of the CPSD in *Fig. 17* has a different origin. Some more insight can be obtained by performing quantitative analyses of both the measured and simulated signals by fitting the phase curve to a linear function in order to determine the slopes and thus the corresponding transit times. Such a study can provide better understanding and more conclusive results, as well as understanding of whether it is possible to see two transit times in the real case.

**Table 2 Parameters used in the simulation.**

Parameter	Value
$H$	365.76 cm
$R$	200 cm
$z_1$	$0.7H$
$z_2$	$0.8H$
$x_1$	$0.99R$
$x_2$	$0.95R$

### 3.5.3. Conclusions

The results obtained in the present study in both the 1D and the 2D cases are not conclusive and require additional consideration. As was demonstrated above, the possibility of the presence of two different slopes related to two different transit times in ex-core/thermocouple measurements in a PWR was confirmed. The existence of two different transit times can be explained by the convolution of the two propagating perturbations travelling in opposite directions. In practice, the latter means that neutron detectors placed near the downcomer sense the same perturbation twice (when it passes the core and the downcomer), whereas the thermocouple can detect the perturbation only inside the core. Despite some similarities in the simulated and measured signals, some severe differences in terms of scaling factors and others can still be observed which need to be explained by other means. Therefore, one can conclude that the specific pattern

observed in the measurements can not be explained by the proposed hypothesis and most likely has a different origin. In order to finally confirm or object the proposed assumption, as well as get better understanding, qualitative estimation of the slopes with a curve fitting procedure can be useful and should be done in the continuation.

### 3.6. Future work

In 2012 the ordinary coherence analysis, performed between different combinations of detector signals (ex-core neutron detector-core exit thermocouple), allowed to estimate the transit time of the coolant in three different quadrants of the core. Further analysis of these transit times indicated that there is a clear asymmetry in the radial flow distribution between different parts of the core with the lowest flow rate being in the upper right quadrant (N42) and with equally high flow rate in the upper and lower left quadrants (N41 and N43, respectively). The latter result partly supports the earlier suggested hypothesis about the origin for ultra-low frequency oscillations observed in Ringhals-4. However, in order to ensure that such an asymmetric flow distribution oscillates with ultralow frequencies, an additional inspection of detector signals is necessary. From a physical point-of-view, it is clear that any changes in the radial flow distribution with time should also lead to the corresponding periodical changes in some of the characteristics of time-dependent signals, measured by neutron detectors/thermocouples (for example, their mean values). Therefore, as a further step, it is reasonable to perform a similar coherence analysis for different parts of the same signal separately (where its properties do not change much), in order to estimate the flow velocities corresponding to the selected time intervals of the original signal. Such an investigation will be undertaken in the continuation. Furthermore, it might also be useful to apply a similar coherence analysis for a new set of measurements such that the discovered flow pattern can be verified.

From the STP-analysis presented in 2012, some correlation between ex-core neutron detector and core exit thermocouple measurements was found which leads to the conclusion that for ultra-low frequencies the neutron noise is most likely driven by the temperature fluctuations. However, this is not a case for low frequency region where the situation becomes reverse, i.e. the fluctuations in thermocouple signals (or temperature fluctuations) are apparently caused by the fluctuations in corresponding neutron detector signals (or neutron noise) which in their turn are induced by some other external sources. In order to draw final conclusions about transmission paths between different detector signals, all possible detector pairs should be analyzed. The analyses is planned to be done in the continuation.

## **4. DEVELOPMENT OF THE THEORY AND SIMULATIONS TO DETERMINE VOID CONTENT IN R-1 FROM THE ANALYSIS OF IN-CORE NEUTRON NOISE MEASUREMENTS.**

### **4.1. Introduction**

In Stage 14 [29], some preliminary results of the study on void fraction/void velocity reconstruction from numerically-simulated in-core neutron noise have been reported. In this report, a simple Monte Carlo based model was developed to simulate two-phase bubbly flow fluctuations in a BWR heated channel. The major advantage of such numerical simulation is a direct access to the model input data, which gives a unique opportunity to test and quantify different unfolding techniques by comparing the reconstructed quantities (the “output”) with the original ones (defined by the model input). In addition, two different approaches (called the “break frequency” and the “transit time” [62] - [66]) for void fraction evaluation were investigated on the basis of this model. Although a good qualitative agreement has been obtained, due to implementation of a simple correlation between the local void fraction and the local void velocity, both methods are far from being applicable for real applications and more advanced and complex modelling is necessary.

Therefore, the purpose of the work in 2012 [30] was to address the above-mentioned problem. For this reason, the two methods were combined together, i.e. the velocity profile was estimated from transit times, and then the result was used in the break frequency method. Thus, no extra correlation between the local void velocity and local void fraction was needed. In this stage it was pointed out that since the original quantities of interest, i.e. the void fraction and void velocity are directly available from the model, the “true” (original) dependence between the local component and the local void fraction can easily be evaluated and compared with the true one obtained from a system code. From this comparison, the axial void fraction and the quality of the unfolding procedure can be estimated. More details on this topic can be found in [30].

In 2013 some additional modifications of the Monte Carlo model were implemented. One of the crucial limitations of the earlier model was that it could handle only bubbly flow regime (i.e. low void fraction,  $\alpha < 0.35$ ) since the overlapping of bubbles was not allowed. However, in a real BWR system, the void fraction tends to be much higher than this value and rises up to 70-80 %, thus covering several flow regimes (slug, annular). Therefore, it was decided in the present period try to extend the existing model to higher void fraction by simply relaxing the condition of bubble non-overlapping. Such a relaxation helps to overcome several problems, in particular, to reach much higher void fraction and change the shape of the bubbles to more realistic, i.e. non-spherical one. Another benefit from allowing the bubble overlapping is that such a model is free of any necessity to specify which of the two phases is a perturbation and which is a medium (more details are given in [29]). In addition, the size of the bubbles (their radius) was also varied while they are generated and travel upwards in the channel.



In 2014 the extended model was used to investigate ANN (Artificial Neural Network)-based method for void fraction and void velocity reconstruction. Such a methodology does not require any correlation between the void fraction and void velocity, however a large training set for ANN should be provided. Some of the results of the velocity reconstruction are presented and discussed below.

#### 4.2. Model description and simulation

In this section, the main features of the aforementioned two-phase flow model utilized in the current study are discussed. In order to construct a realistic model of the two-phase flow based on a Monte Carlo technique, a proper distribution for bubble generation should be chosen [30]. The goal is to construct such a stationary bubble distribution that the resulting void fraction profile will resemble the actual BWR one. Therefore, the bubble generation rate (intensity) per unit length was selected to be proportional to the sin-shaped static flux in the boiling length regime.

The main principles of such a simple model can be summarized as follows: first the bubbles are sampled according to the preselected cumulative function, and then the bubbles are transported with the chosen velocity. As a result, the desired axial void profile can be achieved. Here, it is important to emphasize that the bubble overlapping was allowed in this model. To simplify the simulations, only a two-dimensional model of the heated channel, i.e. the radial and axial cross-section of a real fuel assembly is considered. The height of the channel is chosen to be equal  $H = 400$  cm and its diameter is fixed to  $D = 10$  cm. The bubble inlet velocity is taken to be  $v_0 = 200$  cm/s. The last two quantities are selected in such a way that they correspond to the characteristic parameters of a real BWR fuel assembly.

Accordingly, the bubbles were represented as 2 -D circles. For newly generated bubbles a Gaussian distribution of the bubble diameters with the following parameters was assumed: mean diameter  $\bar{d} = 0.65$  mm, maximum diameter  $d_{\max} = 0.9$  mm and minimum diameter  $d_{\min} = 0.4$  mm. To keep the model simple, this distribution was assumed to be uniform in axial direction, i.e. axially- independent. Besides, while the bubbles propagate upwards along the channel their size was also varying in a linear fashion (up between  $d_{\min} = 0.4$  mm and  $d_{\max} = 0.9$  mm). In order to provide good calculation efficiency, in the present model the time step of the simulation was reduced up to  $6.7 \cdot 10^{-4}$  s. More details on the description of the model can be found in [62]-[65].

Below in Fig. 45-47, we just show some simulation results for the axial void fraction void velocity and neutron noise, respectively, obtained after 320 seconds of the simulation.

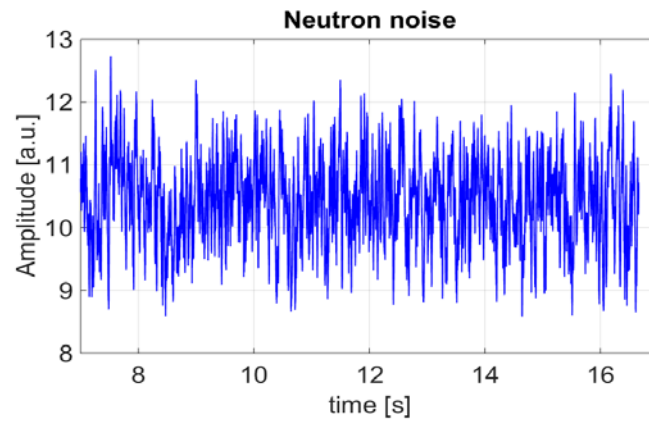


Fig. 45 Simulated neutron noise due to void fraction fluctuations (the output from modified Monte Carlo model) at  $(x = 2.5; z = 240)$  cm.

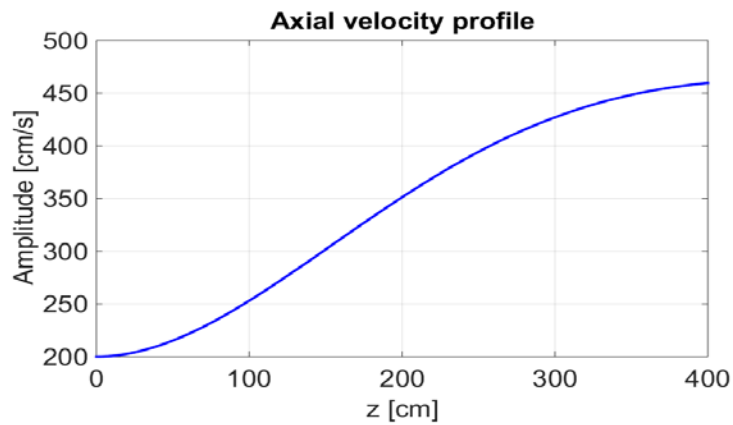


Fig. 46 Cross-section averaged axial velocity profile (the output from modified Monte Carlo model)

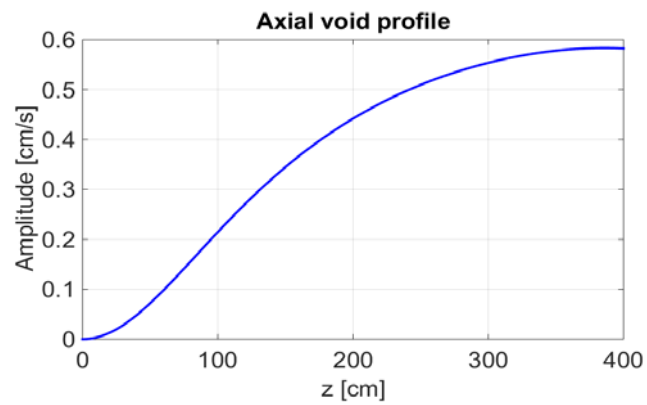


Fig. 47 Cross-section averaged axial void profile (the output from modified Monte Carlo model)

The corresponding normalized neutron noise is generated by spatial convolution between the generated void fraction signals and the local component of the transfer function as:

$$\frac{\delta\phi_\lambda(t, x, z)}{\phi(x, z)} = \int_{-\frac{D}{2}}^{\frac{D}{2}} \int_0^H \exp\left(-\lambda(z)\sqrt{(z-z')^2 + (x-x')^2}\right) \delta\alpha(t, x', z') dz' dx' \quad (23)$$

where  $\phi_0(x, z)$  stands for a static flux,  $\delta\phi(t, x, z)$  is the simulated neutron noise due to void fraction fluctuations,  $\delta\alpha(t, x', z')$  is the simulated void fraction signal at position  $(x', z')$  recorded in a binary form (“1” indicates the presence of the vapour bubble and “0” designates the presence of water) and  $\lambda(z)$  is the axially-dependent local component calculated from CASMO (for more details see report Stage 14 [29]).

#### 4.3. Reconstruction of axial void fraction profile from neutron noise measurements

In the following, the main principles of the modified break frequency method for reconstruction of axial void profile from neutron noise are illustrated. One assumes that the propagating character of the void fluctuations (i.e. propagating bubbles) can be described as:

$$\delta\alpha(x', z', \omega) \propto e^{-i\omega \frac{z'}{v(z)}}, \quad (24)$$

where  $v(z)$  stands for the velocity of the perturbation. Then, one can obtain the following simplified relationship between the Auto Power Density (APSD) of the density (void) fluctuations and the one corresponding to the local component of the induced noise [63]:

$$APSD_z^{\delta\phi_\lambda} = C \cdot APSD_z^{\delta\alpha}(\omega) \cdot \frac{1}{(1 + \omega^2 \tau_\lambda^2)^2}, \quad (25)$$

where

$$\tau_\lambda(z) = \frac{1}{v(z) \cdot \lambda(z)}, \quad (26)$$

defines the time it takes for the perturbation to pass the range of the local component  $\lambda(z)$  and  $C$  stands for the proportionality coefficient. Here, as well as in the further considerations, the APSD is written for the normalized quantities, i.e. normalized to the static (mean) values (static neutron flux).

Eq. (25) shows that the fluctuations in the neutron flux  $\delta\phi_\lambda(x, z, \omega)$  are proportional to the fluctuations in the void fraction  $\delta\alpha(x, z, \omega)$  times a Lorentzian frequency-dependent term with a break frequency at [63], [64]:

$$f_b(z) \equiv f_b(\alpha(z)) = \frac{1}{2\pi} \cdot v(\alpha(z)) \cdot \lambda(\alpha(z)). \quad (27)$$

From Eq. (27) it can be clearly seen that the break frequency depends on the void fraction through the local void velocity and the dependence of the range of the local component on the void fraction. Since the dependence of the range of the local component on the local void fraction can be determined from the code calculations, by using the break frequency and the void velocity from the measurements (estimated by “transit time method”, see next section) to obtain the axial dependence of the range of the local component  $\lambda(z)$  (thus calculated from the measurements), the axial void fraction can be identified. Comparing the reconstructed profile with the one provided by the model (i.e. with the original one), the quality of the proposed method for the void fraction reconstruction can be quantified. The results of such quantification procedure are summarized below.

First, the neutron noise measurements were simulated in eight different axial levels within the same radial position. The corresponding spectral densities were calculated by using a standard Fast Fourier Transform. The results of such calculations can be found in [30]. In addition, the break frequencies for all eight APSDs as well as their amplitudes were numerically estimated by fitting the corresponding curves to Lorentzian coefficient defined in Eq. (25) (see Table 6 in [30]).

For convenience of further considerations, it is instructive to introduce the following terminology: the void fraction (void velocity) estimated from the Monte Carlo model by time averaging of the time-dependent void fraction signals will be called as “true” (or original) one whereas the one estimated from the simulated neutron noise measurements as “reconstructed” (“experimental”).

Finally, in *Fig. 48* the “reconstructed” (i.e. “experimental”) void fraction profile as a function of axial position is shown. For comparison, the “true” void fraction profile is also given in *Fig. 48*. As one can see from the figure, both curves are in a satisfactory qualitative agreement between each other. However, some quantitative deviations between the curves can be observed. Such a mismatch is not surprising since the applied model is very simple and probably does not take into account all aspects of the real phenomenon.

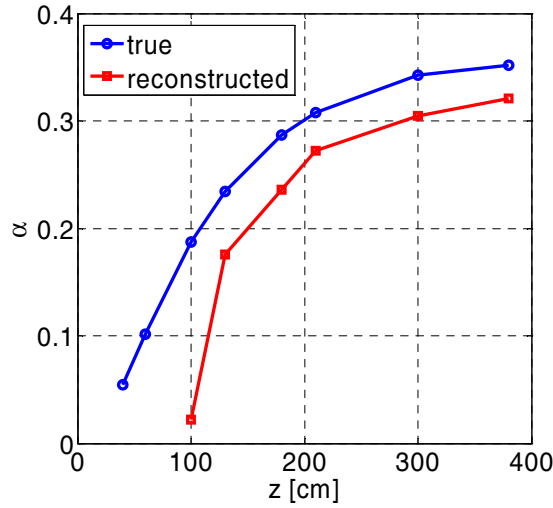


Fig. 48 “True” axial void fraction profile (calculated from Monte Carlo model, blue line) and “reconstructed” (“experimental”) void fraction (estimated from modified break frequency method, red line), respectively.

#### 4.4. Reconstruction of axial void velocity profile from the simulated neutron noise measurements

##### 4.4.1. Overview of the transit time based method for steam velocity reconstruction

The transit times of two-phase flow fluctuations between pairs of detectors axially separated from each other (i.e. the time it takes for the fluctuation to propagate between two axial points, e.g.  $z_1$  and  $z_2$ ) can be determined from noise measurements. In the present work, transit times are estimated from the cross-correlation function (CCF) by using the maximum of this function.

However, the transit time does not give any direct information of the velocity  $v(z_1)$  or  $v(z_2)$  because it is related to the integral of the inverse velocity as

$$\tau_{12} = \int_{z_1}^{z_2} \frac{dz}{v(z)}. \quad (28)$$

Then, assuming the 3rd order polynomial two-piecewise approximation for the inverse velocity  $\frac{1}{v(z)}$ , expressed as:

$$\frac{1}{v(z)} = \begin{cases} b_{11}z^3 + b_{12}z^2 + b_{14} & \text{if } z < z_0, \\ b_{21}z^3 + b_{22}z^2 + b_{23}z + b_{24} & \text{if } z \geq z_0. \end{cases} \quad (29)$$

with  $z_0$  standing for the division point between two profiles and using 5 transit times calculated from the simulated neutron noise together with the continuity condition of the void velocity and its derivative, the unknown coefficients  $b_{11}$ ,  $b_{12}$ ,  $b_{14}$ ,  $b_{21}$ ,  $b_{22}$ ,  $b_{24}$  and  $z_0$  can be estimated by solving the system of non-linear algebraic equations. Once the unknown coefficients are evaluated, the axial velocity profile can be reconstructed.

The particular choice of such 3rd order polynomial approximation for the inverse velocity profile has already been justified earlier in [30]. In practice, in a real BWR power plant, there is an access to only the signals of a set of five in-core detectors (four standard LPRM plus one TIP detector), i.e. only four transit times can be provided. However, in the present study, to improve the quality of the results and avoid extra complexity, an increased number of detector signals will be used.

The corresponding results of the transit time estimations are discussed below. The CCF function between different detector pairs is estimated using the detector signals generated by the Monte Carlo model. The utilized detector positions (which are different from the ones used in the first method) can be found in [30] (see Table 7). Then, the corresponding experimental  $\tau_{tr}$  and true  $\tau_{exp}$  transit times are calculated, and the results are shown in Table 3.

**Table 3 Results of the transit time calculations from the Monte Carlo simulation (both the true and reconstructed ones).**

Det. distance, $d_{ij}$ [cm]	$\tau_{tr}$ , [s]	$\tau_{exp}$ , [s]
$z_{12} = 35$ cm	0.1711	0.1608
$z_{23} = 20$ cm	0.0922	0.0920
$z_{34} = 70$ cm	0.2887	0.2888
$z_{45} = 110$ cm	0.3924	0.3928
$z_{56} = 140$ cm	0.4604	0.4640

As one can see from Table 3, the results for two cases are in a good agreement with each other. Once the transit times are found, one can estimate the unknown coefficients for the velocity profile (see Eq. (29)), as mentioned in the previous section. The results for both the true and “reconstructed” velocity profiles are given in Fig. 49. As one can see from the figure, the two profiles are in a satisfactory agreement with each other. However, some mismatch between the two profiles, especially in the upper part of the core, can be observed. The latter might be due to the low order of the polynomial used for the velocity reconstruction. Thus, it might be reasonable to test other (higher order) polynomial approximations, which at the same time will require additional information about transit times.

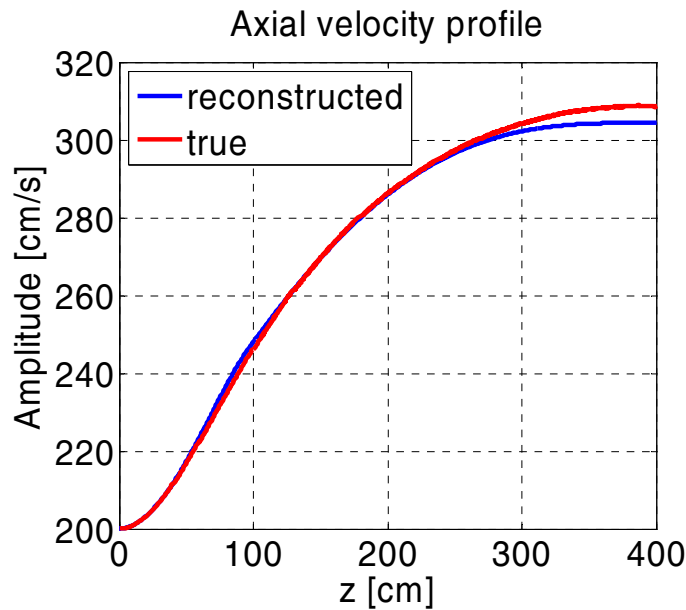


Fig. 49 True axial velocity profile (the output from Monte Carlo model) and reconstructed axial velocity profile (Eq. (29)).

#### 4.4.2. Overview of the ANN based method for steam velocity reconstruction

Further, the steam velocity reconstruction method based on ANN is discussed. Following the standard procedure for ANN, first a large set of input data and corresponding output data (73 samples) was generated by using the aforementioned Monte Carlo model. The choice of the input – output quantities was based on the previous experience with “transit time” method where the axial void velocity profile was approximated with polynomial function and the polynomial coefficients were estimated from several transit times. Therefore, it seems to be natural to select transit times as an input for ANN and corresponding polynomial coefficients as an output. The order of the polynomial as well as the number of transit times (or number of available detectors) should be determined experimentally by testing different combinations of input/output data with

different dimensions. For obvious reasons mentioned in the previous section, the maximum number of transit times cannot exceed more than four. In the following, the results for the 5<sup>th</sup> order polynomial approximation with three (four) transit times will be demonstrated.

For this purpose, 74 samples of velocity profiles were generated in the Monte Carlo model, out of which 73 were used for training and 1 sample for validation and testing. All velocity profiles were then fitted to a 5th order polynomial with 6 unknown coefficients by using MATLAB built-in function “cftool”. Some of the selected velocity profiles used as a training set are plotted in *Fig. 50*. Different velocity profiles were obtained by varying intensity of bubble generation between 8 to 82 bubbles per time step and keeping the inlet velocity constant.

Further, 3 transit times between 4 preselected detector positions shown in Table 4

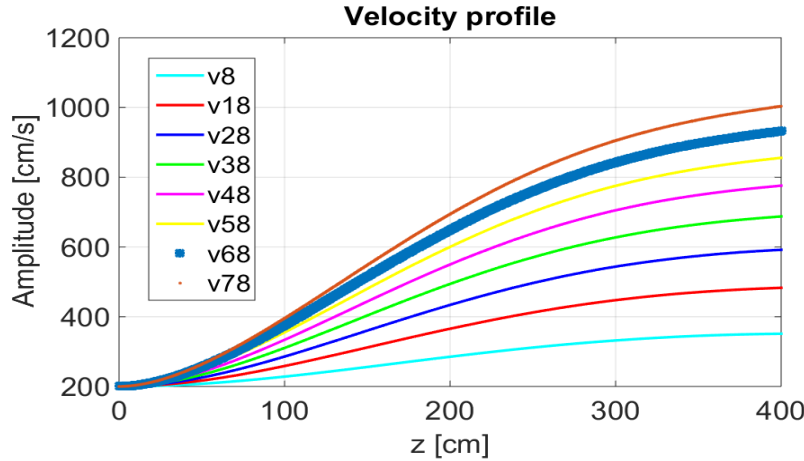


*Fig. 50 ANN training set of axial velocity profiles (the output from modified Monte Carlo model)*

were calculated by using Eq.(28). The corresponding transit times are given in Table 5 (middle column). As a next step the calculated polynomial coefficients and respective transit times were used for creating ANN (training) with 20 hidden layers by using MATLAB built-in tool called “nnstart”. Finally, the prepared ANN was validated by feeding it with the “theoretical” transit times calculated from the excluded (validating) velocity profile in order to determine unknown polynomial coefficients. Thereafter, another test with “experimental” transit times calculated from the simulated neutron noise was performed. The corresponding results for the “true”, theoretically- reconstructed (validating) and experimentally-reconstructed polynomial coefficients for the case of three input transit times are shown Table 6. From Table 6 it can easily be seen that all coefficients except to  $P_1$  and  $P_5$  are very close to each other. The corresponding velocity profiles are demonstrated in *Fig. 51*.

As can be seen from *Fig. 51*, the velocity profile reconstructed from the true transit times is in a good agreement with the “true” (original) velocity profile whereas the one evaluated from experimental transit times slightly deviates from the reference pattern, especially in



the upper part of the core. The latter fact can be explained by the bad precision in the estimations of experimental transit times as can be noticed from Table 5. For comparison purpose, in *Fig. 52* the case with four input transit times is shown. This time, the trend is somewhat different from the one observed in the previous case, i.e. the experimentally reconstructed velocity profile is in a good agreement with the reference one whereas theoretically-reconstructed (validating) is not. Further, in *Fig. 53*, the case with three input transit times but different detector positions is demonstrated. As can be seen from the figure, the situation is similar to the case of four transit times.

From the analysis of these figure, one can clearly see that the quality of the reconstruction strongly depend on the selection of detector position, the quality of transit time calculations and the number of available detectors. In order to achieve the best quality several additional tests are needed to be performed in the continuation.

**Table 4 Axial detector positions**

Detector position $z_d$ , [cm]
$z_1 = 60$
$z_2 = 130$
$z_3 = 240$
$z_4 = 300$
$z_5 = 340$

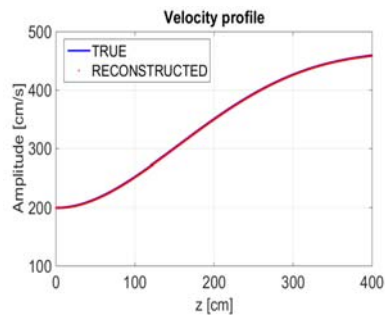
**Table 5 Results of the transit time calculations from the Monte Carlo simulation (both the true (calculated from velocity profile) and experiential (calculated from neutron noise) ones).**

Det. distance, $d_{ij}$ [cm]	$\tau_{tr}$ , [s]	$\tau_{exp}$ , [s]
$z_{12} = 70$ cm	0.2818	0.2807
$z_{23} = 110$ cm	0.3303	0.3300
$z_{34} = 60$ cm	0.1471	0.1473

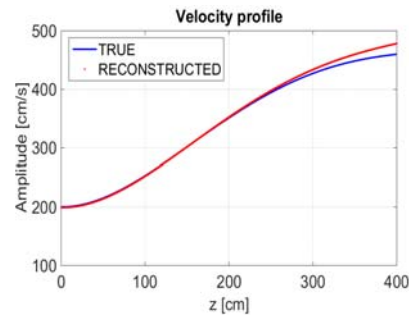
$z_{45} = 40 \text{ cm}$	0.09161	0.09067
$z_{35} = 100 \text{ cm}$	0.2387	0.2386

Table 6 Results of ANN calculations of the polynomial coefficients for axial velocity profile reconstruction.

	True (cal. from velocity profile)	Validated (from true transit times)	Experimental (from calculated transit times)
$P_1$	$2.902 \cdot 10^{-12}$	$1.643 \cdot 10^{-12}$	$1.243 \cdot 10^{-12}$
$P_2$	$1.625 \cdot 10^{-10}$	$1.730 \cdot 10^{-10}$	$1.860 \cdot 10^{-10}$
$P_3$	$-21.67 \cdot 10^{-6}$	$-22.02 \cdot 10^{-6}$	$-22.53 \cdot 10^{-6}$
$P_4$	$7.575 \cdot 10^{-3}$	$7.658 \cdot 10^{-3}$	$7.732 \cdot 10^{-3}$
$P_5$	$-2.813 \cdot 10^{-2}$	$-4.078 \cdot 10^{-2}$	$-3.895 \cdot 10^{-2}$
$P_6$	$2.002 \cdot 10^2$	$1.992 \cdot 10^2$	$1.992 \cdot 10^2$



a)



b)

Fig. 51 True axial velocity profile (the output from Monte Carlo model) and reconstructed axial velocity profile (from ANN, 3 transit times, 5<sup>th</sup> order polynomial): a) transit times calculated from true profile; b) transit times calculated from simulated neutron noise.

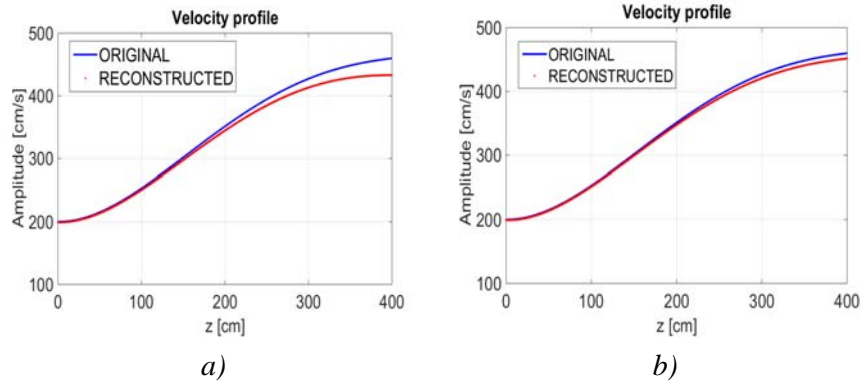


Fig. 52 True axial velocity profile (the output from Monte Carlo model) and reconstructed axial velocity profile (from ANN, 4 transit times, 5<sup>th</sup> order polynomial): a) transit times calculated from true profile; b) transit times calculated from simulated neutron noise.

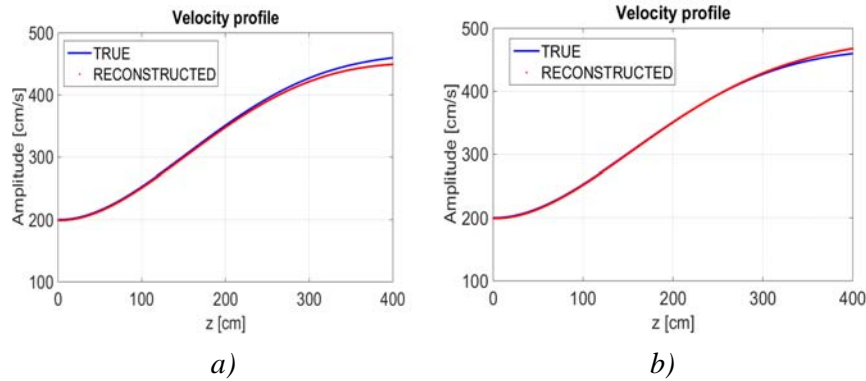


Fig. 53 True axial velocity profile (the output from Monte Carlo model) and reconstructed axial velocity profile (from ANN, 3 transit times, 5<sup>th</sup> order polynomial): a) transit times calculated from true profile; b) transit times calculated from simulated neutron noise.

#### 4.5. Conclusions

During 2012 period, a random bubbly flow regime in a BWR heated channel was simulated by using the earlier-developed Monte Carlo model. The generated signals of the two-phase flow were recorded and employed to calculate the induced neutron noise. Using standard signal processing methods, the break frequency of the APSD of the simulated noise measured at several axial elevations was estimated and then used to determine the “experimental” axial void fraction. Thereafter, a quantitative comparison with the “true” void fraction was performed in order to quantify the accuracy of the modified break frequency method for void fraction reconstruction. Although the two curves show a satisfactory qualitative agreement, further investigation is required to clarify the inconsistencies found. The main advantage of the modified break frequency method is that

it is based on only one single measured quantity (i.e. the neutron noise). As a result, the accuracy of the suggested unfolding technique for void fraction will depend less sensitively on the validity of the assumed correlation between flow velocity and void fraction, since this correlation is not needed. In addition, it is possible to have some redundancy in the methodology, which can be used to increase the reliability of the unfolding. However, to further improve the method, more adequate and realistic correlation between the void fraction and the local component, rather than simple homogeneous CASMO calculations, is needed and will be accomplished in the future work. In addition, during this stage, the method based on the polynomial reconstruction of the axial velocity profile from “experimental” transit times (called “transit time method”) was investigated and some promising results were obtained.

During 2013, the Monte Carlo model of two-phase flow elaborated in previous stage to simulate the in-core neutron noise due to boiling, was modified in order to be able to handle higher void fraction regimes. Some additional modifications (in particular, varying bubble diameter, etc.) to improve the model credibility were also implemented.

In the present stage the newly-developed model was used to generate a set of different velocity profiles for different conditions which was then used as a training set for Artificial Neural Network (ANN) in order to elaborate the method of void velocity reconstruction. Some similar tests with the data obtained from RAMONA code have already been performed in 2013 and showed promising results. Unfortunately, the RAMONA results could not be directly utilized for real applications related to the void velocity reconstruction since the information about the perturbation velocity is not retrievable (for more details see [30]). However, the currently developed model is free from such problems and more suitable for elaborating reconstruction methods.

In the coming period, the developed methodology with ANN is planned to be used to generate a set of data for void fraction reconstruction directly without any need for additional correlations between void fraction and void velocity. More details of such a methodology will be pointed out in the next report.

## **5. EVALUATION OF THE MEASUREMENTS MADE IN R1 WITH THE USE OF 4 LPRMS AND ONE TIP DETECTOR, FOR TESTING THE VELOCITY AND VOID FRACTION PROFILE RECONSTRUCTION METHODS**

### **5.1. Introduction**

In this section some results on the analysis of the transit times evaluated from LPRM-TIP measurements taken in R1 will be presented and discussed. This study was originally initiated by another problem, namely the possibility to reconstruct axial void profile from in-core neutron noise measurements. As previous investigations indicated, in order to obtain a reliable estimation of the void fraction, the axial void velocity profile should be known a priori. Such a reconstruction of the void velocity profile can be performed by using the information about the transit times between axially distributed in-core detectors. As was pointed out in earlier reports, the four permanently installed LPRM detectors in one detector tube can provide only three independent transit times which is definitely not sufficient for a reliable reconstruction of velocity profile. Therefore it was decided to complement the LPRM measurements with one additional TIP measurement to obtain an additional transit time. More details on this topic can be found in [30].

Some preliminary results on the transit time estimation from LPRM-TIP detector pairs were already reported in 2012, but were not successful due to low coherence between the LPRM and TIP signals. The main reason for the negative result in 2012 lay in the properties of the TIP- acquisition system and post processing of the measurement data. It turned out that the TIP-detector signals, which are usually used for calibration purposes of LPRM detectors, were filtered with a low-pass filter and not suitable for the determination of a 4<sup>th</sup> transit time. Thus, it was decided to make another attempt in 2013, where the raw signals (i.e. the excitation current in the form of analog signals) from TIP detectors without any pre-processing were recorded. Using these measurements, four transit times were evaluated. However, the quality of such estimations turned out to be very low, especially for the upper LPRM detector pairs where some obscure transit times were observed. More details can be found in [31].

As a result, it was decided to perform another set of raw (analog) measurements for both LPRM and TIP detectors to exclude any negative effects from signal discretization. Such measurements were performed and analysed in 2014. Unfortunately, the analog LPRM signals are not directly retrievable from the acquisition system. Therefore, in order to obtain such signals, the discretized signals were converted back into analog form. In addition, to improve the resolution of the signals, the length of measurements was doubled by performing two subsequent measurements of the maximum allowed acquisition time for the TIP-detector. Some preliminary results of such estimation are summarized below.

## 5.2. TIP-LRPM measurements in the 2012-2014 period

During the 2012-2014 period, three sets of LPRM-TIP measurements, taken in the Ringhals-1 BWR were analyzed in order to determine four transit times needed for the axial velocity reconstruction.

In 2012 neutron noise analysis was performed on measurements made on 19 December 2011 at nominal conditions. The effective sampling rate was 33.33 Hz. The TIP-measurements were performed with a single movable TIP detector in 7 selected axial positions, whereas the LPRM measurements were taken in four fixed axial positions. Both measurements were made in 4 different radial locations (Strings 20, 21 22, 23). The corresponding axial positions of the LPRM and TIP detectors in the reactor core are shown in *Fig. 54*. The LPRM measurements were made for each TIP-detector position separately. The time span for one measurement was set to around 9 minutes.

In 2013 a new set of neutron noise measurements was performed and analyzed. This time the measurements were taken on 3 July 2013 at nominal conditions. The position of the control rods was changed from 63 % to 65 % and from 32 % to 33 % just before the measurements were started. The effective sampling rate was 33.33 Hz.

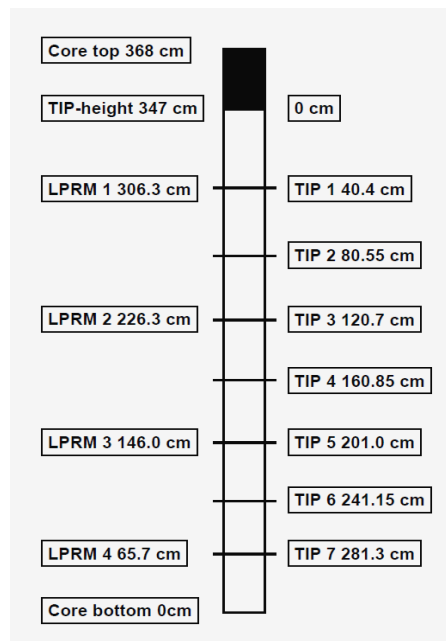


*Fig. 54 Illustration of the axial positions of the LPRM and TIP detector measurement positions.*

The set-up for LPRM and TIP-measurements was similar to the one used in 2012, i.e. 7 selected axial positions (TIP-20-1, 2, 3, 4, 5, 6, 7) for TIP detectors and four fixed axial positions and 4 different radial locations (Strings 20, 21 22, 23) for LPRM measurements. The LPRM measurements were made for each TIP-detector position separately. The time

span for the first three measurements (TIP-20-1, 2, 3) was set to around 9 minutes, but two of these measurements were manually stopped close to the end since the TIP detector started to move. Therefore, the rest of the measurements were performed for the reduced time, i.e. for 8 minutes 50 seconds.

In 2014 similar TIP-LPRM measurements were made on 25 February 2014 at nominal conditions. The effective sampling rate was again set to 33.33 Hz. The axial detector locations for the measurements were selected to be the same as in 2012-2013 whereas the radial ones were reduced to only three of them i.e. String 20-22. Compared to the previous measurements, the time span for the measurements was doubled by performing two subsequent sets of measurements.

### 5.3. Spectral analysis of the TIP-LRPM signals

Before starting the analysis of estimated transit times, it is worth to mention here that the recording procedure for TIP and LPRM signals was not identical. Thus, in the case of TIP measurements the raw signals were directly registered on the computer, whereas in the LPRM case the detector signals had to be processed four times before they finally were recorded. This latter fact means that the two detector signals were not fully synchronized and were recorded with some internal time difference. Therefore, in order to obtain proper transit times between TIP and LPRM, the above-mentioned time delay should properly be accounted for. Obviously, this extra time delay introduces an additional complexity and uncertainty in the estimation procedure. According to the measurement instructions such a time delay cannot exceed more than 120 ms (it takes 30 ms for each of four pre-processing steps). This prediction is in a relatively good agreement with the obtained results for transit times as will be seen later on.

Compared to the ordinary LPRM-detectors, which are usually fission chambers, the TIP-detectors are often so-called self-powered neutron detectors, whose main signal is given rise by the electrons of a beta-decay of the reaction products, and which can only follow slow flux variations. However, there is some prompt component of the signal from the prompt gamma of the neutron reaction, which can be used for noise measurements. Hence the TIP detectors are mainly utilized for calibrating purposes. In addition, the raw TIP measurements are rarely used for the determination of the transit times. Thus, as a starting point, it is instructive to first analyze the shape of the measured signals themselves, and their probability distributions (PDF). The corresponding TIP-signals, taken in 2013 at String 20 together with their PDFs, are plotted in *Fig. 55*. As it is clearly seen from the left part of the figure, the time dependence of the TIP-signals has the standard shape of LPRM signals, and no signal distortion can be observed. The form of the probability density function (see the right part of *Fig. 55*.) also follows a typical Gaussian shape, which is a common shape for the neutron noise LPRM measurements.

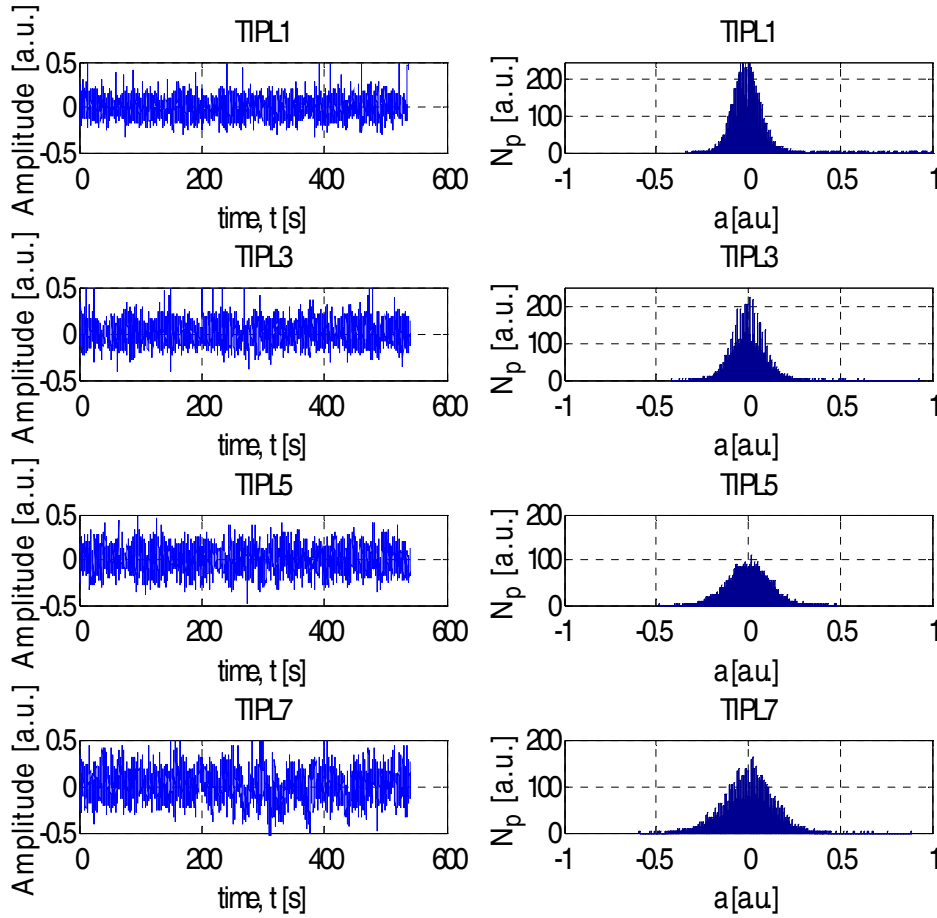
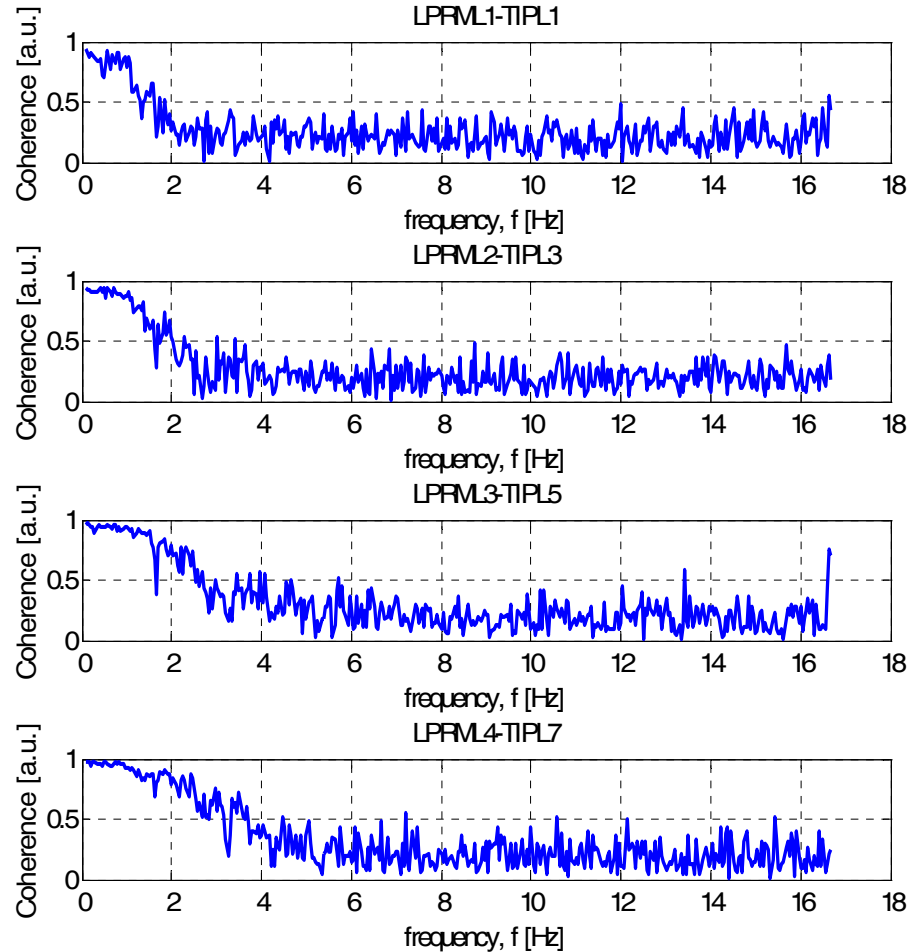


Fig. 55 TIP detector signals (left figure) and their probability distributions (right figure), String 20.

Further, the coherence function between different TIP and LPRM signals was also plotted and analysed. The result is shown in Fig. 56. As one can notice, in all cases the coherence is relatively high, (close to unity) in the low frequency region, i.e. between 0.1-3 Hz. The latter result confirms that both detectors see the same phenomenon (or perturbation). For comparison, in Fig. 57, the coherence between two LPRM detectors is shown where high coherence values can be observed in the same low frequency region as before. The presented plots for the coherence function give some confidence in the reliable estimation of the transit times.





*Fig. 56 Coherence between LPRM and the corresponding TIP detector signals measured at the same axial position, String 20.*

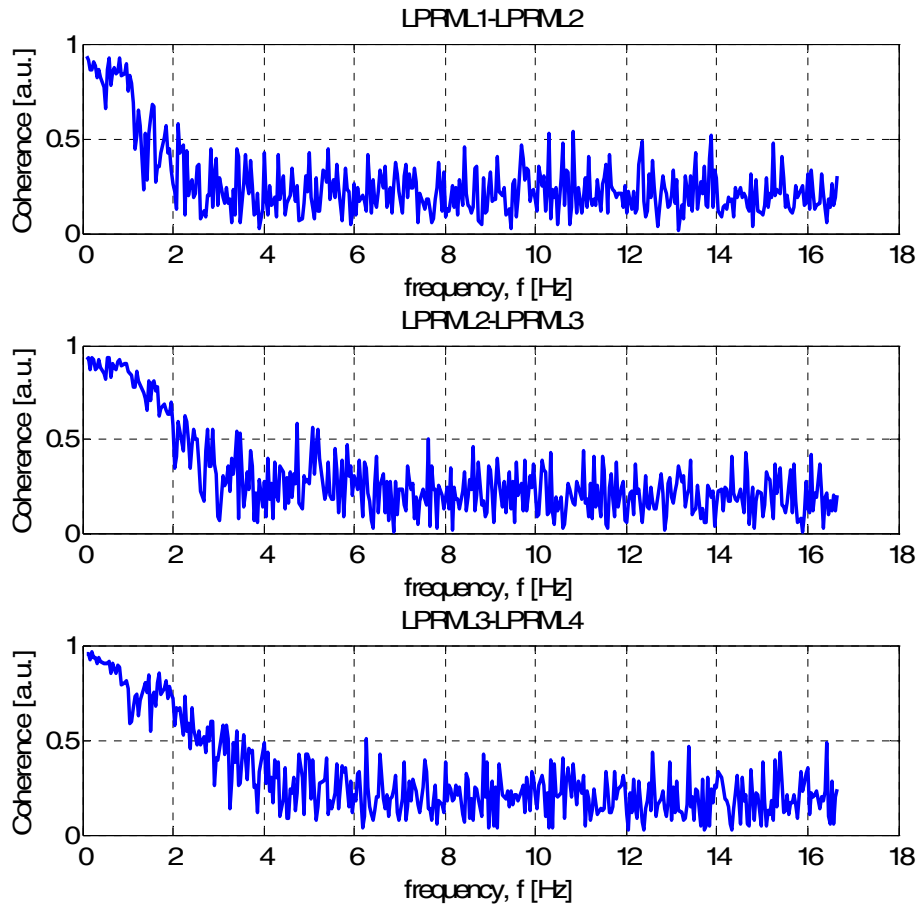


*Fig. 57 Coherence between LPRM detector signals measured at the same radial position and different axial elevations, String 20.*

It should also be mentioned that on the contrary to 2013, the measurements taken in 2012 were not suitable for determining transit times from TIP-LPRM detector pairs. As was pointed out in an earlier report [30], for those measurements the phase of the CPSD calculated between TIP and LPRM signals was not linear and none of peaks were detected in IRF (Impulse Response Function [30]) which could be used for transit time estimations. The further analysis of the signals showed a very low coherence (close to zero) between TIP and LPRM detectors located in the same axial position. The corresponding coherence functions for String 21 are plotted in *Fig. 58*. From the thorough analysis of the figure, it was concluded that LPRM and TIP detectors did not measure the same phenomenon; otherwise the coherence would be close to unity as was observed above in *Fig. 56*. This latter fact can then explain why neither the CPSD (i.e. its phase) nor the IRF gave any consistent physically interpretable information for estimating corresponding transit times in 2012.

As was mentioned in [30], the reason for these negative results in 2012 lay in the acquisition system and post processing of the measurement data. It turned out that the TIP-detector signals, which are usually used for the calibration purpose of LPRM detectors, were filtered with a low-pass filter. The break frequency of the filter was set at 0.5 Hz, which means that all frequencies above 0.5 Hz (including the region of interest above 1 Hz) were filtered out from the measured signals. The latter means that the obtained noise measurements made by TIP-detectors was not suitable for the determination of a 4<sup>th</sup> transit time. However, in the Ringhals acquisition system, there is a possibility to obtain raw TIP measurements which are not filtered, and could be then used for transit time estimations. Such a study has been performed in 2013 and the results of analysis of the measurements and transit time estimations are shown below.

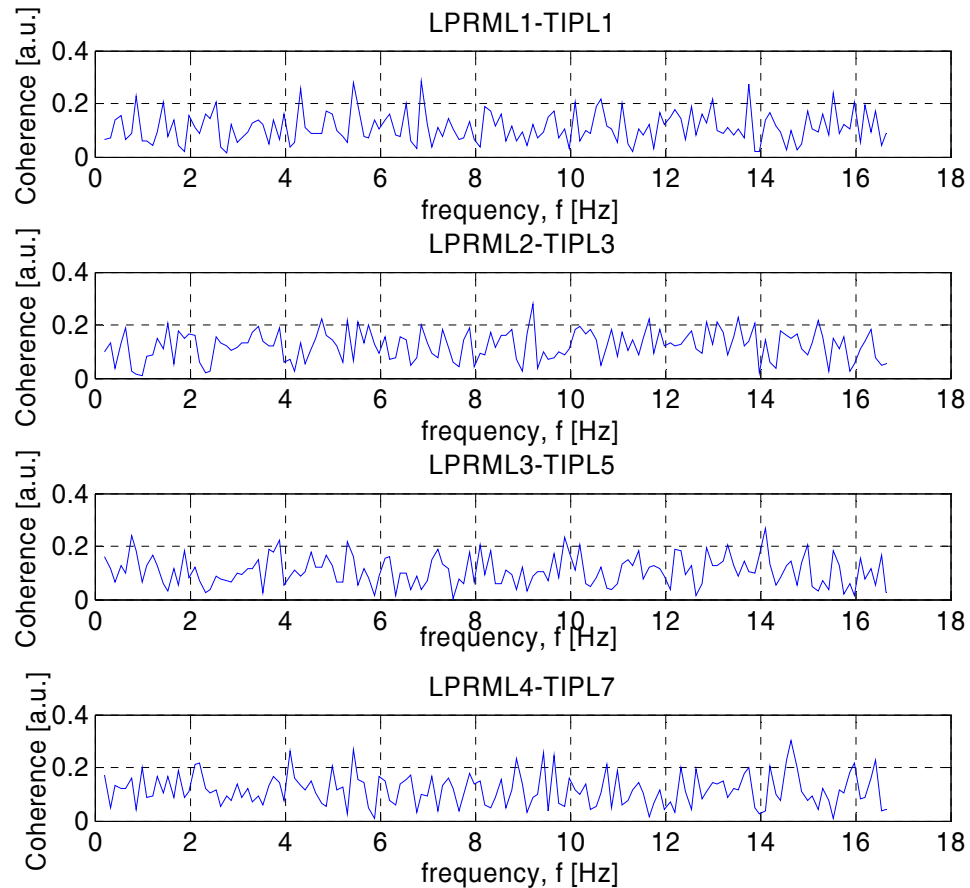


*Fig. 58 Coherence between LPRM and the corresponding TIP detector signals measured at the same axial position, String 21.*

In order to determine the transit time of the void fraction fluctuations, we will follow the standard procedure based on the calculation of the phase of Cross Power Spectral Density (CPSD) between different axially distributed detectors pairs. Assuming that only the local component exists (i.e. assuming that an in-core-neutron detector is sensitive to only local component), then the signal of two detectors  $i$  (upper) and  $j$  (lower) placed along an axial line at a distance  $z_i - z_j$  to each other would have signals similar to each

other but with some time delay  $\tau_{ij} = \frac{z_i - z_j}{v}$ , where  $v$  is the propagation velocity (i.e. its mean value). Thus, after the application of Wiener–Khinchin theorem, for the cross spectrum between the two detectors one gets

$$CPSD_{\phi_j^l}(z_i, z_j, \omega) \cong APSD_{\phi_j^l}(z_j, \omega) \exp(-i\omega\tau) \quad (30)$$

According to Eq. (30), the phase of the cross spectrum is a linear function of  $\omega$  from which the transit time of the propagation perturbation can be determined, as well as its averaged velocity can be estimated (in practice only the frequency range between 0.1-15 Hz can be used for this purpose due the presence of other noise sources).

Some illustrations for three selected detector pairs, in the form of the phase of the CPSD calculated between the original measured signals are given in *Fig. 59*. As one can see from the right figures where the phase of the CPSD between two LPRM detectors in the same string is plotted, the phase follows a pattern characteristic for the propagating perturbations, i.e. the phase is linear up to 4 Hz. The slope of the phase provides the transit time of the propagation of the perturbation between two axial detector positions. Such linear phase behaviour is observed for both the CPSD calculated between the TIP and LPRM detectors as well as between LPRM detectors only (see left figure of *Fig. 59*). Applying the following linear fit  $\varphi_{ij} = \tau_{ij}\omega + c_{ij}$  to the phase of the CPSD (red line), i.e. utilizing the corresponding formulas for the Least Mean Square Fitting with  $c_{ij}$  set to zero, the transit time between different detector pairs can be obtained. In the above,  $\tau_{ij}$  stands for phase slope and thus defines the corresponding transit time.

The results of the transit time estimations for different combinations of LPRM and TIP detectors, as well as between LPRM detectors alone for the measurements made in 2013 are presented in Table 7-8, respectively. The transit times with a poor quality of estimation due to a very short linear region of the CPSD phase, which are thus not reliable, are marked with red. For the case of LPRM-TIP detector pairs, the transit times were corrected with some time delay to account for the fact that the original detector signals were not properly synchronized, as has already been mentioned earlier. This time delay was determined by using the phase of the CPSD calculated between LPRM and TIP detectors placed at the same axial level. Since several such time delays were available, the time delay was not set to be constant for all detector pairs but was varied from one pair to another one. The corresponding LPRM-TIP pair used for the correction is given in

parentheses next to transit time value (see Table 7). Investigating transit times for different combinations of detector signals including both LPRM-TIP and LRPM-LRPM pairs, the one which introduced a minimum error for each specific LPRM-TIP detector pair was chosen. In Table 7, the corresponding LPRM-TIP detector pairs used for estimating the time delay are shown separately for each specific case.

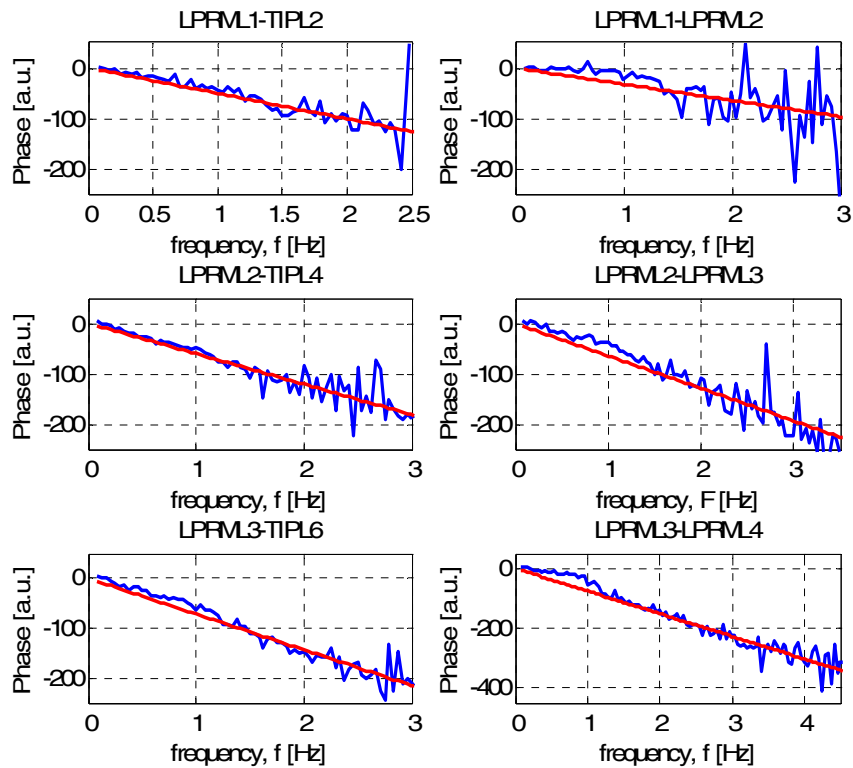


*Fig. 59 Phase of Cross Power Spectral Density calculated between the original detector signals, String 20.*

**Table 7 Transit times (in seconds) calculated from the slope of the phase of CPSD taken between LPRM and corresponding TIP detector signals for different axial positions (String 20, 2013) (the time delay due to desynchronization is taken into account); the quantities given in parenthesis are explained on page 38.**

	LPRM-1	LPRM-2	LPRM-3	LPRM-4
TIP-1	0 (L1-T1)	0.0837 (L1-T1)	-	-
TIP-2	-0.0493 (L1-T1)	-0.0100 (L2-T3)	0.2132 (L2-T3)	-
TIP-3	-0.0775 (L2-T3)	0 (L2-T3)	0.1707 (L2-T3)	-
TIP-4	-	-0.0533 (L2-T3)	0.0936 (L3-T5)	0.2827 (L3-T5)
TIP-5	-	-0.1750 (L3-T5)	0 (L3-T5)	0.2063 (L3-T5)
TIP-6	-	-0.2873 (L3-T5)	-0.1056 (L3-T5)	0.0470 (L4-T7)
TIP-7	-	-	-0.2077 (L4-T7)	0 (L4-T7)

**Table 8 Transit times (in seconds) calculated from the slope of the phase of CPSD taken between two consecutive LPRM detector signals for different axial positions of TIP detector (String 20, 2013)**

	LPRM 1-2	LPRM 2-3	LPRM 3-4
TIP-1	- 0.0745	- 0.1819	- 0.2123
TIP-2	- 0.0897	- 0.2069	- 0.2122
TIP-3	- 0.0838	- 0.1853	- 0.2131
TIP-4	- 0.0962	- 0.1794	- 0.2159
TIP-5	- 0.0802	- 0.1994	- 0.2086
TIP-6	- 0.0741	- 0.1944	- 0.2105
TIP-7	- 0.0738	- 0.1778	- 0.2116

The analysis of the results presented in Table 7-8 shows several peculiar features. The first one is the fact that not all estimated transit times fully agree with each other. In particular, the difference between two transit times, the one calculated between 2 LPRM detectors (LPRM2 and LPRM3 corresponding to the measurements with TIP detector positioned at axial level 5) and another transit time evaluated between one of the LPRMs (LPRM 2) and one TIP (TIP 5) detector placed at the same axial position as the second LPRM can reach up to 0.02 s (see Table 7 (line 6) and Table 8 (line 6), respectively).

Another problem of the obtained results, which has nothing to do with the TIP detectors, is related to the transit times estimated between different LPRM signals. In particular, the transit time between LPRM-2 and LPRM-3 is almost identical with the one obtained for another pair of LPRM signals, i.e. LPRM-3 and LPRM-4. From the physical point of view, one would expect a much larger difference between those detector pairs since the flow velocity is higher in the middle of the core as compared to the one in the lower part of the core. Thus, the reliable estimation of the transit time becomes questionable. In addition, it turned out that the present LPRM signals recorded with VXI-scanner connected to the digital TELEPERM XS-system were not of the same quality compared to earlier measurements where a separate recording system (DEWETRON) was used. Also, differences in low pass filtering efficiency, sampling rate, A/D resolution and digital signal processing, make a direct comparison between signals collected by the two

different data acquisition systems somewhat difficult. As a result, the frequency region with a linear character of the phase behaviour was significantly reduced. Yet another interesting observation is a constant phase in some of LPRM measurements between 0.1-1 Hz, such as, for example, in *Fig. 59* (see upper and lower right figures, LRPM1-2 and LRPM3-4 pairs). The reason for such an unexpected behaviour is not fully understood and can probably be explained due to presence of a strong reactivity component. These latter facts bring an additional ambiguity in the obtained results and affect their reliability. For better visualization, the results of the mean velocity estimations based on the data shown in Table 7-8 are plotted in *Fig. 60* as function of averaged axial detector position for both LPRM-LPRM and LPRM-TIP detector pairs. In *Fig. 60* the increasing trend of void velocity with axial elevation can be noticed which gives some confidence in the positive results of the further studies. From *Fig. 60* the similar conclusions as from Table 7-8 can also be drawn.

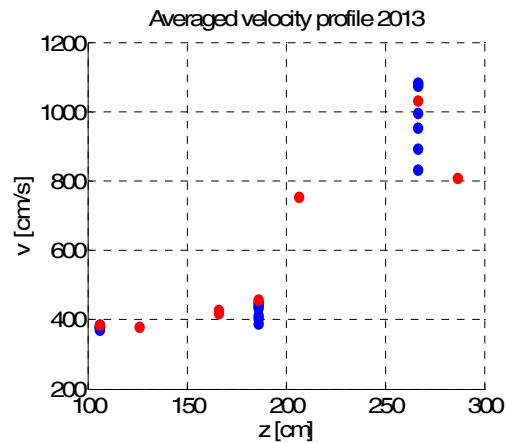


*Fig. 60 Results of mean velocity estimations from the measurements taken in 2013 at Ringhals-1, String 20 (blue circles for LPRM-LPRM pairs, red circles for LPRM-TIP pairs).*

The results for the transit times, evaluated from the last set of measurements taken in 2014 at String 22 are given in Table 9 and Table 10 for LPRM-LPRM and TIP-LPRM detector pairs, respectively. Some similar trends as observed previously in 2013 can also be observed here. In particular, not all estimated transit times fully agree with each other. For example, the difference between two transit times, the one calculated between 2 LPRM detectors (LPRM1 and LPRM2 corresponding to the measurements with TIP detector positioned at axial level 3) and another transit time evaluated between one of the LPRMs (LPRM 1) and one TIP (TIP 3) detector placed at the same axial position as the second LPRM can reach up to 0.07 s (see Table 9 (line 3) and Table 10 (line 3), respectively). On the other hand, another problem noticed in 2013 and related to the transit times estimated between different LPRM signals, does not seem to be so crucial anymore. As can be seen from Table 9, all three transit times calculated between two consecutive LPRM detectors are clearly distinct and thus can be considered as physical except for the last three cases which are marked in red. These data seem suffering from the same problem as the

evaluations made in 2013, namely the transit times calculated between LPRM-2 and LPRM-3 detectors are almost identical with the transit times calculated between LPRM-3 and LPRM-4. For comparison, in Table 11, the transit times estimated from doubled measurement set taken in 2014 are shown. Comparing these values with the ones in Table 9, one can conclude that in both cases the results are almost identical. Thus, there is no significant improvement in the quality of transit time estimation between single and double measurement sets.

**Table 9 Transit times (in seconds) calculated from the slope of the phase of CPSD taken between two consecutive LPRM detector signals for different axial positions of TIP detector (String 22, single measurement set, 2014)**

	LPRM 1-2	LPRM 2-3	LPRM 3-4
TIP-1	- 0.1251	- 0.2089	- 0.2755
TIP-2	- 0.1282	- 0.2049	- 0.2700
TIP-3	- 0.1295	- 0.2077	- 0.2646
TIP-4	-0.1295	- 0.2023	- 0.2671
TIP-5	- 0.1037	- 0.2398	- 0.2724
TIP-6	- 0.1053	- 0.2365	- 0.2491
TIP-7	- 0.1068	- 0.2281	- 0.2397

**Table 10 Transit times (in seconds) calculated from the slope of the phase of CPSD taken between LPRM and corresponding TIP detector signals for different axial positions (String 22, 2014) (the time delay due to desynchronization is taken into account); the quantities given in parenthesis are explained on pages 73-74.**

	LPRM-1	LPRM-2	LPRM-3	LPRM-4
TIP-1	0 (L1-T1)	0.101 (L1-T1)	-	-
TIP-2	-0.0197 (L1-T1)	-0.0084 (L2-T3)	-	-
TIP-3	-0.0581 (L2-T3)	0 (L2-T3)	-	-
TIP-4	-	-0.0666 (L2-T3)	0.116 (L3-T5)	-
TIP-5	-	-0.2046 (L3-T5)	0 (L3-T5)	-
TIP-6	-	-0.3048 (L3-T5)	-0.0722 (L3-T5)	-
TIP-7	-	-	-0.2596 (L3-T5)	0 (L4-T7)

**Table 11 Transit times (in seconds) calculated from the slope of the phase of CPSD taken between two consecutive LPRM detector signals for different axial positions of TIP detector (String 22, double measurement set, 2014)**

	LPRM 1-2	LPRM 2-3	LPRM 3-4
TIP-1	- 0.1253	- 0.2111	- 0.2712
TIP-2	- 0.1272	- 0.2089	- 0.2684
TIP-3	- 0.1289	- 0.2114	- 0.2740
TIP-4	-0.1291	- 0.2051	- 0.2765
TIP-5	- 0.1029	- 0.2303	- 0.2481
TIP-6	- 0.1056	- 0.2252	- 0.2461
TIP-7	- 0.1066	- 0.2267	- 0.2573



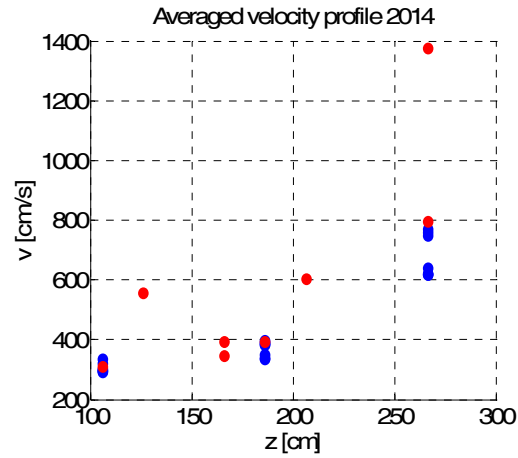


Fig. 62 Results of mean velocity estimations from the measurements taken in 2014 at Ringhals-1, String 22 (blue circles for LPRM-LPRM pairs, red circles for LPRM-TIP pairs, single measurement set).

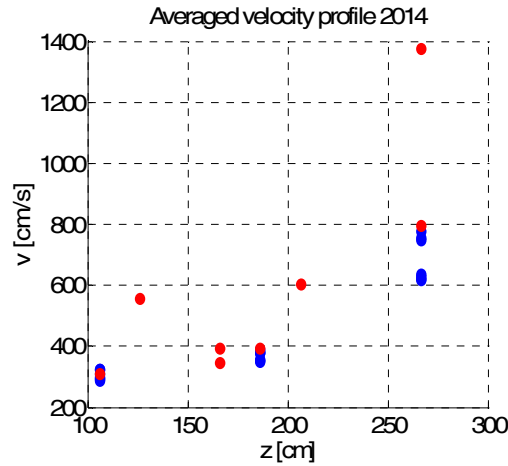


Fig. 61 Results of mean velocity estimations from the measurements taken in 2014 at Ringhals-1, String 22 (blue circles for LPRM-LPRM pairs, red circles for LPRM-TIP pairs, double measurement set).

The corresponding results of mean velocity evaluations made in 2014 at Ringhals-1 are plotted in Fig. 62 – 62 as a function of averaged axial detector position for both LPRM-LPRM and LPRM-TIP detector pairs for single and double measurements, respectively. Similar to the results obtained in 2013, in both figures Fig. 62 – 62 the increasing trend of the mean velocity with an axial detector position can be pointed out showing the possibility of further elaboration of the void velocity reconstruction method based on transit time estimations. From Fig. 62 – 62 the same conclusions as from Table 9-11 can also be drawn.

#### 5.4. Conclusions

The analysis of the measurements, taken in 2012 was not conclusive since the required frequency content of the LRPM signals was filtered out. However, the results presented in 2013-2014 clearly indicated the possibility to obtain 4 transit times from LRPM-TIP detector pairs. However, the accuracy of the obtained results is still questionable. Thus, in 2013 in the case of pure LRPM detector pairs, the transit times estimated at different axial levels showed identical values which were unphysical due to the different velocities of the flow at different axial positions. In 2014 the above-mentioned problem was partially mitigated by analysing raw analog LRPM/TIP signals and was observed just in a few cases and only for lower detector pair as compared to the upper detector pair in 2013. Moreover, some inconsistency in the transit time estimations between LRPM and TIP detectors was also observed, in particular the difference in transit time estimations from LRPM-LRPM and LRPM-TIP detector pairs placed at the same axial elevations. The latter observation can be explained by the fact that for the LRPM signals different processing system with different filtering properties as compared to the earlier measurements was applied. As a result, the frequency region with a linear phase behaviour was reduced which also affected the accuracy of the transit time estimations. At the present stage, the proper determination of extra (fourth transit) time from TIP-LRPM correlation does not seem to be possible due to low quality of the measured signals and as a result controversial results between LRPM-LRPM and LRPM-TIP measurements. Further investigation is necessary to clarify the way to improve the obtained results and is planned to be performed in the future.

### 6. PROPOSAL FOR 2015

1. A preliminary study of the possibility of modelling 3-dimensional fuel assembly vibrations in a realistic PWR system with the CORE SIM simulator. Due to the fact that the computational mesh grid of the existing core simulators is too coarse as compared to the displacement of the fuel assemblies (the node size is around 15 cm whereas the fuel assembly displacement is in the millimetre range), the direct simulation of the fuel vibrations with such tools seems to be problematic and might lead to erroneous results. One way to handle such a problem is to calculate the changes in cross sections (both amplitude and phase) due to fuel vibrations separately on a fixed grid computational tool and then use it as a noise source for the core simulator. In addition, compared to the earlier studies where only radial vibrations of the fuel assemblies were of a main interest, the axial vibrations of the fuel assemblies can also be properly taken into account in such a study. In the case of positive results, the analysis will be continued in the future.
2. A preliminary study of the 3-dimensional neutron noise induced by inlet temperature fluctuations in a realistic PWR system using the closed loop CORE SIM simulator. All previous studies on this topic were only performed for the 2-dimensional open-loop (i.e. all feedbacks were neglected) model of a reactor. The aim of the present study is to

analyze the effect of the inlet temperature fluctuations with different spatial relaxation lengths (i.e. different radial coupling) on the neutron flux using a more realistic 3-dimensional model of a PWR where all feedbacks are taken into account. Such an investigation is planned to be undertaken in 2015.

3. Analysis of new ex-core measurements, taken in R-4 after power increase. The aim is to investigate the effect of power increase by 18.6 %, which is planned to be undertaken in R-4 in 2015 on the measured neutron noise.
4. Development of the mode separation model with an extension to describe 3-D vibrations. Inspections of the core barrel indicate that in addition to the beam and shell mode vibrations, “wobbling” type vibrations can also occur. Such components can be identified if both the upper and lower ex-core detectors are utilised simultaneously, and the symmetry relationships are taken into account to enhance such components, similarly to how the beam and shell mode components can be enhanced by suitable combinations of the signals of only the lower or the upper detectors. Extending the formerly purely 2D model to 3-D can benefit even the diagnostics of the beam mode vibrations, if e.g. the reactivity component is estimated from the sum of 8 detectors instead of 4. The methods developed can be tested on already existing measurements. In particular it may happen that the method can explain the extra peaks that were observed in the spectra of R2, which are possibly due to the difference of the thermal shield in R2 from those in R3 and R4 (the frequency of the “wobbling” movement is not known).
5. A study was performed last year on calculating the ex-core noise by fuel assembly vibrations by the use of the dynamic core simulator CORE SIM, in order to see if the scaling factor between mechanical vibrations and the normalised detector current increases during the cycle. We propose to use the same CORE SIM model to investigate the correctness of the hypothesis that the reactivity component extracted from the ex-core detector signals can be due to fuel assembly vibrations. To this end, the neutron noise in four ex-core detectors at the same axial level should be calculated, and the reactivity effect extracted with the same signal analysis method as the one used in the experiments. On the other hand, the exact reactivity effect of the vibrations can be calculated by CORE SIM. Actually one could even calculate the space dependent component of the induced neutron noise by subtracting the reactivity component from the total noise, and its symmetries could be investigated. In possession of the symmetry properties one could test whether this component can also be obtained approximately by a signal addition and subtraction method from the measured signals. Such a study could give a useful support to the confirmation and utilisation of the hypothesis on the physical origin of the peaks in the measured spectra.
6. A basic study in neutron noise theory is suggested, which could give some indirect support to our efforts in the determination of the void fraction from neutron noise measurements. This study will be performed in a collaboration with internal (Chalmers Nuclear Engineering) and external (EPFL Lausanne) partners. The idea is that neutrons emitted independent from each other from a source with simple Poisson statistics (Am-Be or Pu-Be source), slowing down and diffusing in a non-multiplying medium, which are hence originally uncorrelated, become correlated if the medium in which the

slowing down and diffusion takes place is fluctuating (e.g. of a result of a perturbation, such as the presence of two-phase flow). This is the very essence of power reactor noise, namely the fact that it is the joint (simultaneous) perturbation of the history of several neutrons which creates the correlations between the neutrons, irrespective of the presence or absence of neutron chains due to multiplication. An experiment can be performed with a neutron source in a water tank and at least two neutron detectors, with introducing bubbles in the water between the source and the detectors. Such an experiment can be performed both in Chalmers and at our collaboration partners, the EPFL Lausanne.

## 7. ACKNOWLEDGEMENT

This three-year contract was performed by funding from Ringhals Vattenfall AB, contract No. 630217-031. Contact person from Ringhals was Adj. Prof. Henrik Nylén.

## REFERENCES

- [1] J. B. Dragt and E. Türkcan (1977), *Progress in Nuclear Energy*, vol. **1**, pp. 293-307.
- [2] F. Åkerhielm, R. Espefält and J. Lorenzen (1982), *Progress in Nuclear Energy*, vol. **9**, pp. 453-464.
- [3] G. Embring (2005), Ringhals AB, Private communication.
- [4] M. Pázsit and I. Pázsit (2008), Final report on the Analysis of Core Barrel Vibrations in Ringhals PWRs R2, R3 and R4 from the Measurements Made in winter 2007/2008. Nucleus DatorFysik report NDF-09.
- [5] M. Pázsit and I. Pázsit (2006), Final report on the Analysis of Core Barrel Vibrations in Ringhals PWRs R2, R3 and R4 from the Measurements Made in 2005. Internal report Chalmers Nukleär teknik, 2006-01-26.
- [6] M. Pázsit and I. Pázsit (2006), Final report on the Analysis of Core Barrel Vibrations in Ringhals PWRs R2, R3 and R4 from the Measurements Made in Spring 2006. Nucleus DatorFysik report NDF-1, 2006-10-01.
- [7] M. Pázsit and I. Pázsit (2007), Final Report on the Analysis of Core Barrel Vibrations in Ringhals PWRs R2, R3 and R4 from the Measurements Made in Autumn 2006. Nucleus DatorFysik report NDF-2, 2007-03-07.
- [8] G. Por, P. A. Kantor and L. A. Sokolov (1995), "Experience with a reactor noise diagnostics system for WWER-1000 type Russian reactors", *In: Proc. Symposium on Nuclear Reactor Surveillance and diagnostics (SMORN VII)*, vol. **1**, pp. 69-77.
- [9] Sizewell B Power Plant (2007), Private communication.

- [10] I. Pázsit, C. Montalvo-Martín, A. Hernández-Solís, P. Bernitt Carteno and H. Nylén (2010), "Diagnostics of core barrel and fuel assemblies vibrations in the Swedish Ringhals PWRs", *Seventh American Nuclear Society, International Topical Meeting on Nuclear Plant Instrumentation, Control and Human-Machine Interface Technologies*, Las Vegas, Nevada, November 7-11, 2010, on CD-ROM, American Nuclear Society, LaGrange Park, IL.
- [11] R. Pérez and D. N. Wood (1991), "Modeling and Analysis of Neutron Noise from an Ex-Core Detector at a PWR", *Proceedings of SMORN-VI*, Gatlinburg, Tennessee, USA.
- [12] R. T. Wood (1990), "A neutron noise diagnostic methodology for Pressurized Water Reactors", The University of Tennessee, Knoxville.
- [13] I. Pázsit, N. S. Garis, O. Thomson, and L. Norberg (1996), *Analys av brusmätningar genomförda under perioden 93-94 vid Ringhals 3*. CTH-RF-116/RR-2, Chalmers University of Technology, Gothenburg, Sweden.
- [14] I. Pázsit (Editor) (1996), *Final Report on the Research Project Ringhals Diagnostics and Monitoring, Stage 1*. CTH-RF-122/RR-3, Chalmers University of Technology, Gothenburg, Sweden.
- [15] I. Pázsit, J. Karlsson, and N. S. Garis (1997), *Final Report on the Research Project Ringhals Diagnostics and Monitoring, Stage 2*. CTH-RF-132/RR-4, Chalmers University of Technology, Gothenburg, Sweden.
- [16] J. K.-H. Karlsson, and I. Pázsit (1998), *Final Report on the Research Project Ringhals Diagnostics and Monitoring. Stage 3: Analysis of core barrel vibrations in Ringhals 2, 3 and 4 for several fuel cycles*. CTH-RF-135/RR-5, Chalmers University of Technology, Gothenburg, Sweden.
- [17] C. Demazière, V. Arzhanov, J. K.-H. Karlsson, and I. Pázsit (1999), *Final Report on the Research Project Ringhals Diagnostics and Monitoring, Stage 4*. CTH-RF-145/RR6, Chalmers University of Technology, Gothenburg, Sweden.
- [18] C. Demazière, V. Arzhanov, and I. Pázsit (2000), *Final Report on the Research Project Ringhals Diagnostics and Monitoring, Stage 5*. CTH-RF-156/RR7, Chalmers University of Technology, Gothenburg, Sweden.
- [19] C. Demazière, V. Arzhanov, and I. Pázsit (2001), *Final Report on the Research Project Ringhals Diagnostics and Monitoring, Stage 6*. CTH-RF-161/RR8, Chalmers University of Technology, Gothenburg, Sweden.
- [20] C. Demazière, V. Arzhanov, and I. Pázsit (2002), *Final Report on the Research Project Ringhals Diagnostics and Monitoring, Stage 7*. CTH-RF-167/RR9, Chalmers University of Technology, Gothenburg, Sweden.

- [21] C. Demazière, C. Sunde, V. Arzhanov, and I. Pázsit (2003), Final Report on the Research Project Ringhals Diagnostics and Monitoring, Stage 8. CTH-RF-177/RR10, Chalmers University of Technology, Sweden.
- [22] C. Demazière, C. Sunde, and I. Pázsit (2005), Final Report on the Research Project Ringhals Diagnostics and Monitoring, Stage 9. CTH-RF-187/RR11, Chalmers University of Technology, Sweden.
- [23] C. Sunde, J. Wright, C. Demazière and I. Pázsit (2005), Final Report on the Research Project Ringhals Diagnostics and Monitoring, Stage 10. CTH-RF-194/RR12, Chalmers University of Technology, Sweden.
- [24] C. Sunde, C. Demazière and I. Pázsit (2007), Final Report on the Research Project Ringhals Diagnostics and Monitoring, Stage 11. CTH-NT-206/RR13, Chalmers University of Technology, Sweden.
- [25] C. Demazière (2011) CORE SIM: A multi-purpose neutronic tool for research and education, *Ann. nucl. Energy* 38, 2698-2718
- [26] I. Pázsit, C. Demazière, C. Sunde, P. Bernitt and A. Hernández-Solís (2008), Final Report on the Research Project Ringhals Diagnostics and Monitoring, Stage 12. CTH-NT-220/RR-14, August 2008, Chalmers University of Technology, Sweden.
- [27] M. Pázsit and I. Pázsit (2009), Final Report on the Analysis of Core Barrel Vibrations in Ringhals PWR R4 from Measurements Made in February 2009. Nucleus DatorFysik report NDF-12, 2009-05-01.
- [28] I. Pázsit, C. Montalvo Martín, V. Dykin and T. Tambouratzis (2010), Final Report on the Research Project Ringhals Diagnostics and Monitoring, Stage 13. CTH-NT-230/RR-15, March 2010.
- [29] I. Pázsit, C. Montalvo Martín, V. Dykin and H. Nylén (2011), Final Report on the Research Project Ringhals Diagnostics and Monitoring, Stage 14. CTH-NT-253/RR-15, December 2011.
- [30] V. Dykin, C. Montalvo Martín, H. Nylén and I. Pázsit (2012), Ringhals Diagnostics and Monitoring Annual Research Report 2012, CTH-NT-269/RR-17, December 2012.
- [31] V. Dykin, C. Montalvo Martín, H. Nylén and I. Pázsit (2013), Ringhals Diagnostics and Monitoring, Annual Research Report 2013, CTH-NT-286/RR-18.
- [32] A. Carcía-Berrocal, J. Blázquez, C. Montalvo and M. Balbás (2010), “Resolving Mechanical Resonances with the Breit-Wigner Formula”, *J. Vibr. Control*.
- [33] N. H. Tran, I. Pázsit and H. Nylén (2015), “Investigation of the ex-core noise induced by fuel assembly vibrations in Ringhals-3 PWR”, To appear in *Annals of Nuclear Energy*.

- [34] P. Bernitt (2008), “In-core neutron noise analysis for diagnosing fuel assembly vibrations at R4”, *MSc thesis work*, Department of Nuclear Engineering, Chalmers University of Technology, CTH-NT-218.
- [35] C. Sunde, M. Pázsit and I. Pázsit, (2006), “Diagnostics of beam mode core-barrel vibrations in the PWRs Ringhals 2-4”, PHYSOR 2006, American Nuclear Society's Topical Meeting on Reactor Physics, September 10-14, Vancouver, BC, Canada.
- [36] G. Kosály, L. Meskó and I. Pázsit (1977), “Investigation of the possibility of using static calculations (adiabatic approximation) in the theory of neutron noise”, *Annals of Nuclear Energy*, vol. **4**, pp. 79.
- [37] I. Pázsit (1977), “Investigation of the space-dependent noise induced by a vibrating absorber”, *Atomkernenergie*, vol. **30**, pp. 29.
- [38] F. J. Sweeney, J. March-Leuba and C. M. Smith (1985), “Excitation Sources for Fuel Assembly Vibrations in a PWR”, *Trans. Am. Nuc. Soc.* Vol. **49**, pp 334-335.
- [39] I. Pázsit, J. Karlsson and N. S. Garis (1998), “Some development in core barrel vibration diagnostics”, *Annals of Nuclear Energy*, vol. **25**, pp. 1079-1093.
- [40] R. Perez and D. N. Wood (1991) “Modeling and Analysis of Neutron Noise from an Ex-Core Detector at a PWR”, In: *Proc. Symposium on Nuclear Reactor Surveillance and diagnostics (SMORN IV)*, Gatlinburg, Tennessee, USA, May 19-24, Vol. **1**, pp 18.01-18.14.
- [41] F. J. Sweeney, J. March-Leuba and C. M. Smith (1985), “Contributions of fuel vibrations to ex-core neutron noise during the first and second fuel cycles of the Sequoyah-1 pressurized water reactor”. *Prog. Nucl. Energy* Vol. **15**, pp 283-290.
- [42] I. Pázsit. H. N. Tran, V. Dykin and A. Jonsson (2013) *Research and Development Program in Reactor Diagnostics and Monitoring with Neutron Noise Methods*, Stage 18. SSM Internal Report No. 2013:04 ISSN: 2000-0456. Available at [www.stralsakerhetsmyndigheten.se](http://www.stralsakerhetsmyndigheten.se)
- [43] B. Severinsson (July 2013), “Brusmätningar för analys av hårdhöljesvibrationer på Ringhals 3. Utförda mellan 2013-02-26 och 2013-07-05”. Ringhals internal report, UH-rapport 2245846 / 2.0.
- [44] B. Severinsson (Sept. 2013), “Brusmätning för analys av Hårdhöljesvibrationer på utförda under 2013”. Ringhals internal report, UH-rapport 2233461 / 2.0.
- [45] M. Nilsson (October 2010), “Brusmätning för att söka lågfrekventa störningar i R3, 100826. Ringhals internal report, UH-rapport 2099930 / 2.0.
- [46] R. Oguma (1984), “A Method of Signal Transmission Path Analysis for Multivariate Random Processes”. Report JAERI-M 84-084.

- [47] R. Oguma and E. Türkcan (1985), “Application of an improved multivariable noise analysis method to investigation of PWR noise; signal transmission path analysis”, *Progress in Nuclear Energy*, vol. **15**, pp. 863-873.
- [48] R. Oguma (1982), “Extended Partial and Multiple Coherence Analyses and Their Application to Reactor Noise Investigations”, *Journal of Nuclear Science and technology*, vol. **19**, pp. 543-554.
- [49] G. Pór, I. Lux and L. Meskó (1985), “Comments on practical application of autoregressive signal analysis to PWR NNP noise data”, *Progress in Nuclear Energy*, vol. **15**, pp. 897-902.
- [50] D. Wach, G. Kosály (1974), Investigation of the joint effect of local and global driving sources in incore-neutron noise measurements. *Atomkernenergie*, vol. **23**, pp. 224-250.
- [51] G. Kosály, L. Maróti, L. Meskó (1975), “A simple space dependent theory of the neutron noise in a boiling water reactor”, *Annals of Nuclear Energy*, vol. **2**, pp. 315-321.
- [52] I. Pázsit, Transport theory and stochastic processes, (2007), Lecture notes, Chalmers University of Technology, Sweden.
- [53] H.M. Hashemian, I. Jakubenko and V. Forej (1994), Measurements of core barrel-vibration and testing for core flow anomalies. Proceedings of the Specialist's Meeting on Instrumentation and Control of WWER Type Nuclear Power Plants, Prague, Czech Republic.
- [54] I. Pázsit, C. Demazière (2011), Noise Techniques in Nuclear Systems, Chapter in Handbook of Nuclear Engineering, Vol. 3, Reactors of Generation II, Springer, New York, USA.
- [55] I. Pázsit, O. Glöckler (1983), “On the neutron noise diagnostics of PWR control rod vibrations I. Periodic vibrations”, *Nucl. Sci. Engng*, vol. **85**, pp. 167-177.
- [56] I. Pázsit, O. Glöckler (1984), “On the neutron noise diagnostics of PWR control rod vibrations II. Stochastic vibrations”, *Nucl. Sci. Engng*, vol. **88**, pp. 77-87.
- [57] G. Kosály (1980), “Noise investigations in boiling-water and pressurized-water reactors”, *Prog. in Nuclear Energy*, vol. **5**, pp. 145-199.
- [58] I. Pázsit, O. Glöckler (1985), “Cross sectional identification of two-phase flow by correlation technique”, *Prog. in Nuclear Energy*, vol. **15**, pp. 661-669.
- [59] I. Pázsit (1986), “Two-phase flow identification by correlation techniques”, *Ann. Nucl. Energy*, vol. **13**, pp. 37-41.



- [60] F. B. Brown, T. M. Sutton (1996), Monte Carlo fundamentals, The 1996 Frederic Joliot summer school in reactor physics. Modern reactor physics and the modelling of complex systems proceedings, Cadarache & France, August 19-28, pp. 348-352.
- [61] D. Wach and G. Kosály (1974), Investigation of the joint effect of local and global driving sources in in-core neutron noise measurements, *Atomkernenergie*, vol. **23**, pp. 244-250.
- [62] V. Dykin, and I. Pázsit (2012), “Simulation of in-core neutron noise measurements for axial void profile reconstruction in boiling water reactors”, Proc. of the International Conference of the Physics of Reactors: Advances in Reactor Physics (PHYSOR 2012), Knoxville, Tennessee, USA, April 15-20.
- [63] V. Dykin, and I. Pázsit (2012), “Simulation of neutron noise induced by two-phase density fluctuations in a Boiling Water Reactor”, Proc. of the Reactor Noise Transfer Knowledge Meeting (RNKTM 2012), Prague, Czech Republic, October 16-19
- [64] V. Dykin, and I. Pázsit (2012), “Neutron noise based method to determine void fraction in a Boiling Water Reactor ”, Proc. of the European Nuclear Conference (ENC 2012), Manchester, United Kingdom, December 9-12.
- [65] V. Dykin, and I. Pázsit (2012), “Simulation of in-core neutron noise measurements for axial void profile reconstruction in boiling water reactors”, *Nuclear Technology*, vol. **183** (3), pp. 354-366.
- [66] V. Dykin (August 2013), “Using neutron noise to determine void fraction”, *Nuclear Engineering International*, pp. 16-17.

## APPENDIX A

### Evaluation of the measurements taken in R2 in 2014

In the last report, containing the results of the measurements made in 2013, it was seen that the spectral characteristics of R2 were different from those in R3 and R4. The separation of the modes seemed not to work for the fitting and cross spectra between opposite detectors did not give the relationships expected by the beam mode vibrations. Very similar features were found in the 2014 measurements. The shape of the APSDs are different from those of R4. The coherence between opposite detectors is low in the frequency range of the beam mode and the phase is not  $180^\circ$ . Hence the characteristic signatures of the pendular motion are missing in the frequency range of the beam mode, around 7 Hz. At the same time, the peak appears to be entirely due to the reactivity component, as the mode separation in *Fig. 63*.

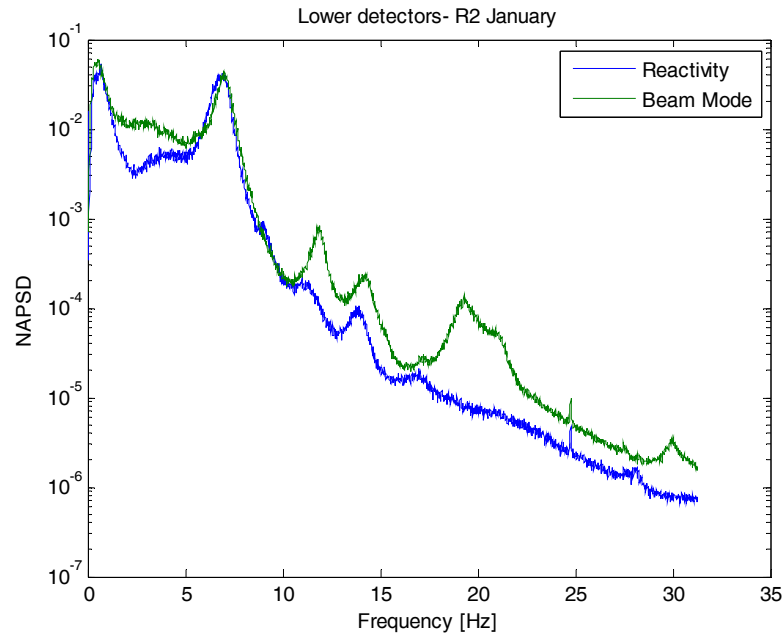


*Fig. 63. The beam mode and its reactivity component of the lower detector power spectra in R2*

As it can be observed, the peak around 7.5 Hz cannot be distinguished in two peaks; and at the same time the reactivity and beam mode components turn out to be almost the same.

In the following figures (*Fig. 64*), coherences and phases from cross spectra between opposite detectors are shown. In the range of 7.5 Hz the coherence is low and the phase is not fully  $180^\circ$ .

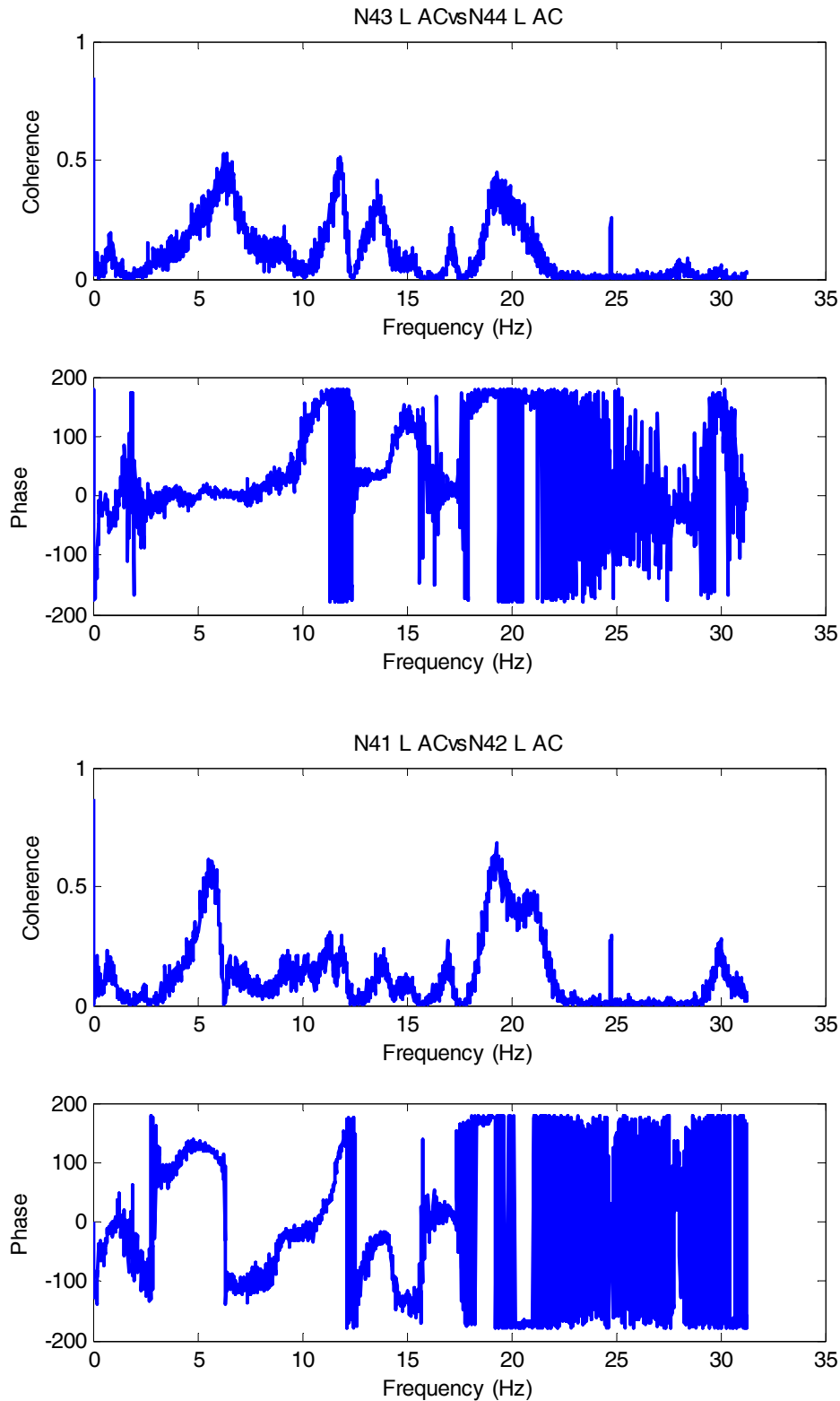
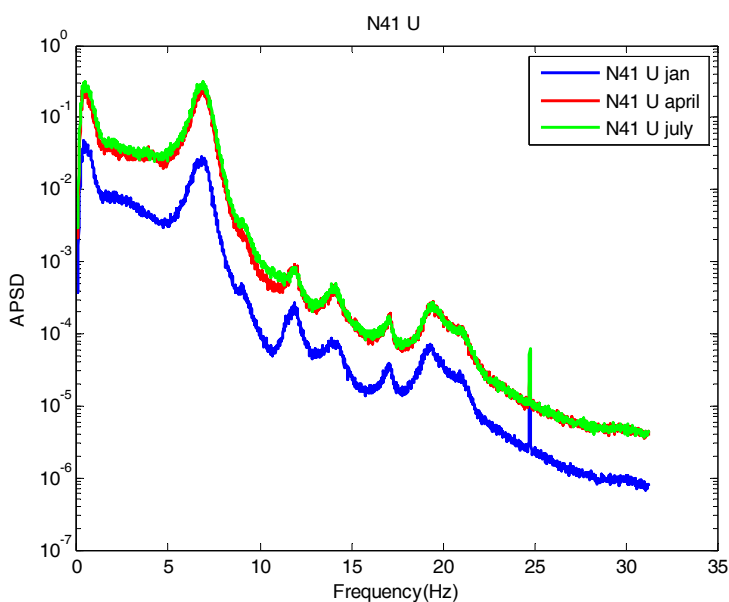
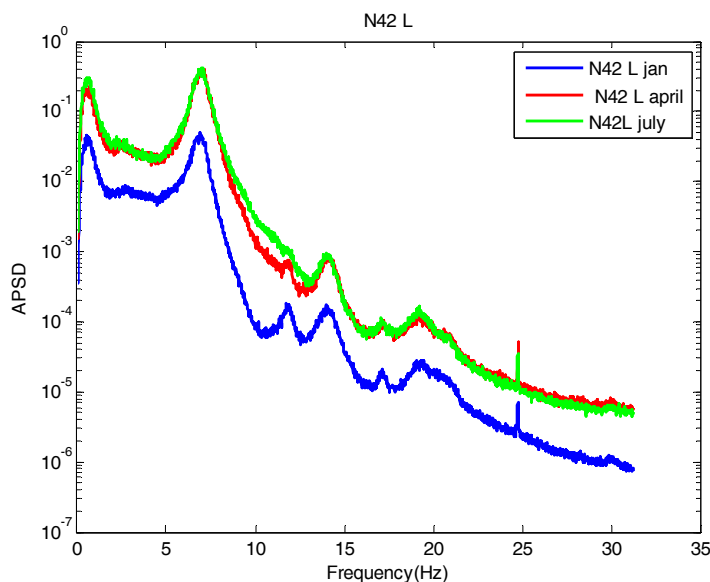


Fig. 64. Coherences and phases between two opposite detector pairs in R2

In the last annual report, there were significant changes in the APSDs from one set of measurements to the next one. Because of this, the trend analysis was not reliable. In the present set of measurements from 2014, there is an increase of the amplitude between the January set of measurements and the other two, April and July, but no noticeable changes in the shapes of the APSDs, as is seen in *Fig. 65 - Fig. 66*.



*Fig. 65 The APSDs of the detector N41 U in the three consecutive measurements.*



*Fig. 66. The APSDs of the detector N42 L in the three consecutive measurements*

### Qualitative analysis of the 2014 measurements in R2

The data to be characterized is both from 2013 and 2014. Basically the three components Beam Mode, Reactivity and Shell Mode are calculated to see how they progress along two cycles. Also coherence between them will be obtained in order to distinguish which components contribute more to the global reactivity component.

We can divide the qualitative analysis in three parts:

- A. Coherence and phase relationship between ex-core detectors in the beam mode and shell mode regions.
- B. Different components of the spectra for lower and upper detectors
- C. Coherence between the reactivity component and the beam and shell mode components.

These three features will be discussed below.

- A. Coherence and phase relationships between opposite detectors are shown in Fig. 67.

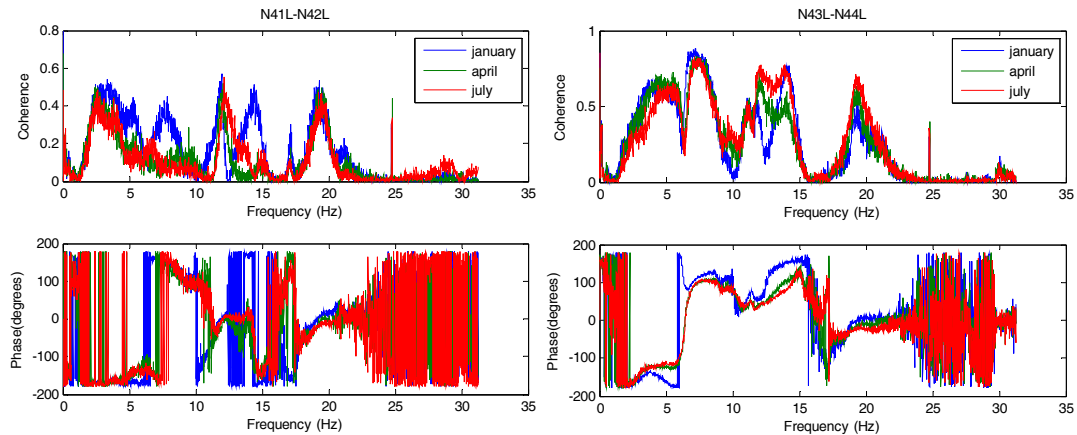


*Fig. 67 Coherence and relationships between opposite detectors in the 2014 measurements in R2*

As it is seen, the magnitude of the coherence between the lower detectors N41-N42 is relatively low, and the shape of the coherence changes between the three measurements. In the coherence between the lower detector pair N43-N44, there is a dip around the beam mode frequency, but the coherence is relatively high both below and above the dip frequency. The reason for the occurrence of the dip is not understood. The presence of the dip is persistent in all three measurements. The phase is approximately  $180^\circ$  between both pairs, but it fluctuates somewhat.

The coherence/phase relationships suggest that the beam mode properties are better seen in the signals of the pair N43-N44, indicating that the preferred direction of the movement is most likely along or close to the line of direction between N43-N44 rather than to the line N41-N42.

### B. Different components of the spectra for lower and upper detectors

Compared to R3 and R4, the spectra from R2 show two more peaks apart from the beam and the shell mode (*Fig. 68*). One is at around 12 Hz and it mainly exhibits a shell mode type character, whereas the peak at 15 Hz is a pendular type that leads to a reactivity component.

From January to July it is seen that the reactivity component overlaps with the beam mode component in the 6-8 Hz region as if the latter is producing most part of the reactivity in that frequency range. No separation of the reactivity and beam components is achieved, as was the case also in 2013. The shell mode is properly identified at around 20 Hz.

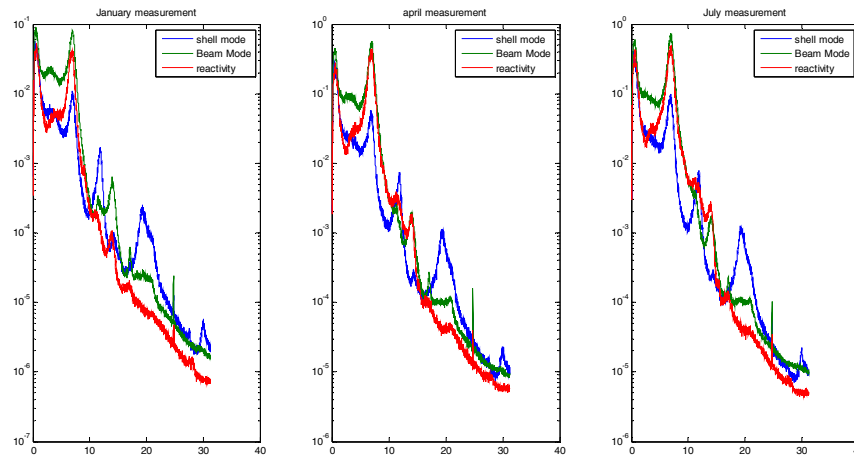
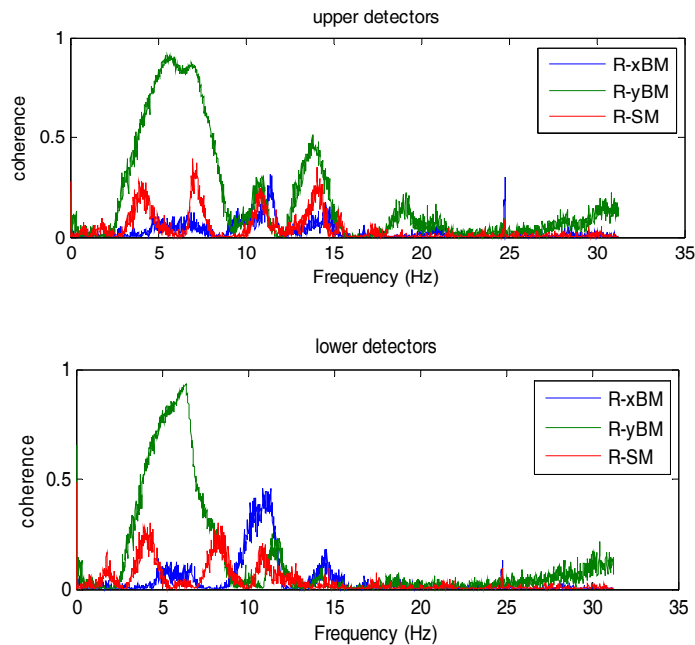


*Fig. 68 The beam mode, shell mode and reactivity components of the spectra in the 2014 measurements in R2*

### C. Coherence between the reactivity component and the beam and shell mode components.

#### January

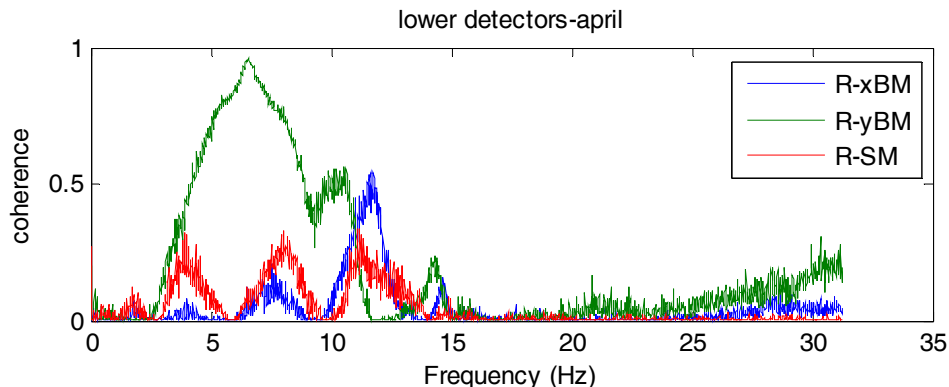
One way of getting insight into the characteristics of the vibrations is to investigate the coherences between the reactivity component on one side, and the  $x$ - and  $y$  components of the beam mode vibrations, (N41-N42 and N43-N44, respectively), and the shell mode component. These are shown in *Fig. 69* below.



*Fig. 69. Coherence between the reactivity component and the x- and y-direction beam mode components and the reactivity in the measurements in January 2014*

It is seen that in the beam mode frequency region, the coherence is overwhelmingly the largest between the reactivity and the y component of the beam mode vibrations. The coherence between the reactivity and the shell mode and the x component of the beam mode are considerably lower. Such a difference between the x and y components can also be seen in the cross spectra between opposite detectors, where the coherence was very high for the pair N43-N44 and very low for N41-N42. This implies that the beam mode vibrations are the ones which generate the reactivity fluctuations. This is different from what was found in R4 where the reactivity peak was associated with the individual vibrations of the fuel assemblies.

For the measurements in April and July, the coherence between the y-beam mode component and the reactivity one is even higher, as is seen in *Fig. 70* and *Fig. 71*. The overall tendencies are the same as in the January measurements.



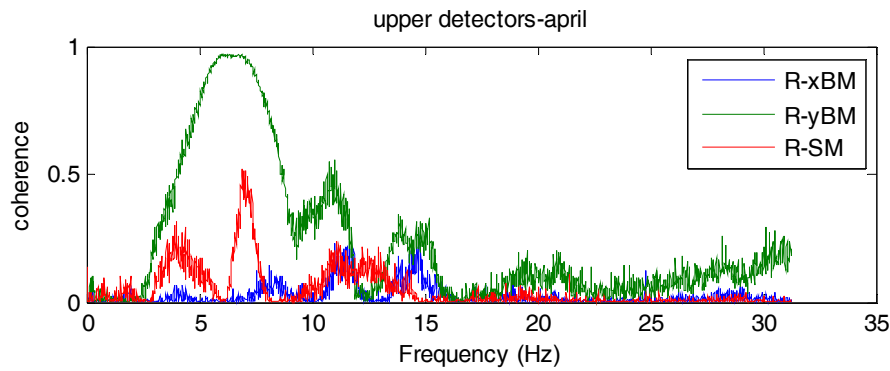


Fig. 70. Coherence between the reactivity component and the x- and y-direction beam mode components and the reactivity in the measurements in April 2014

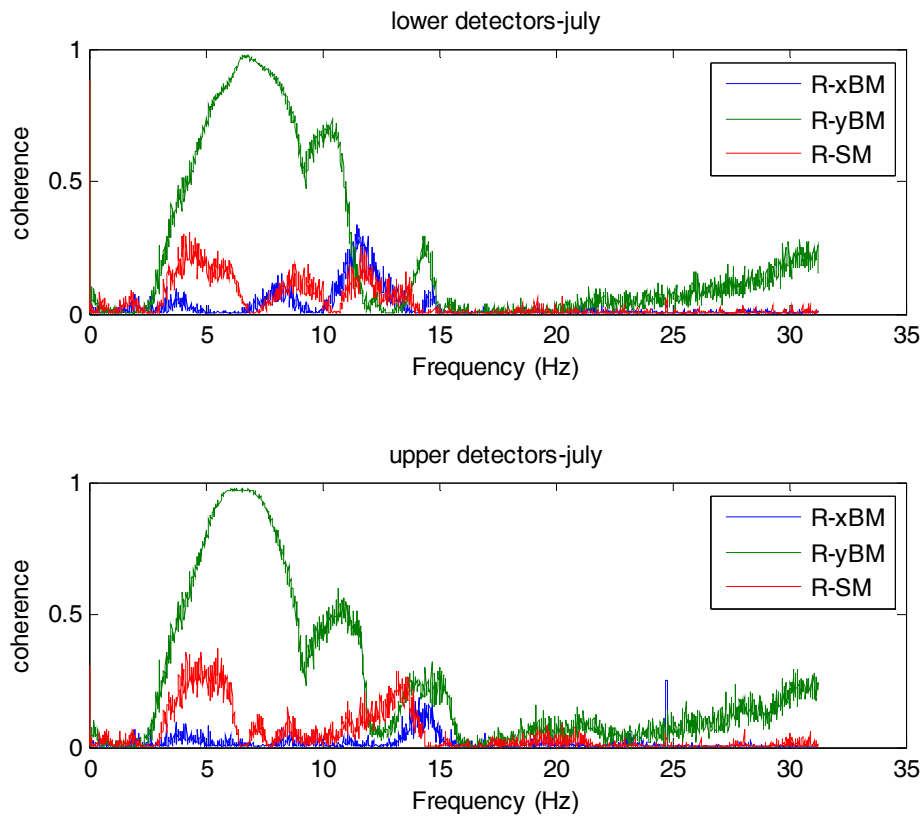


Fig. 71. Coherence between the reactivity component and the x- and y-direction beam mode components and the reactivity in the measurements in July 2014

These measurements suggest that there is no distinguishable double peak around the beam mode frequency in R2, which would be similar to those in R3 and R4. The trend analysis within the cycle and between different cycles will have to be made by different means. This will be done in the continuation of the project.



## APPENDIX B

### Evaluation of the measurements taken in R4 in 2014

There were three measurements, taken in February, April and July 2014.

The separation of the reactivity and the beam mode components was performed the same way as before with success, as it can be seen in *Fig. 72*.

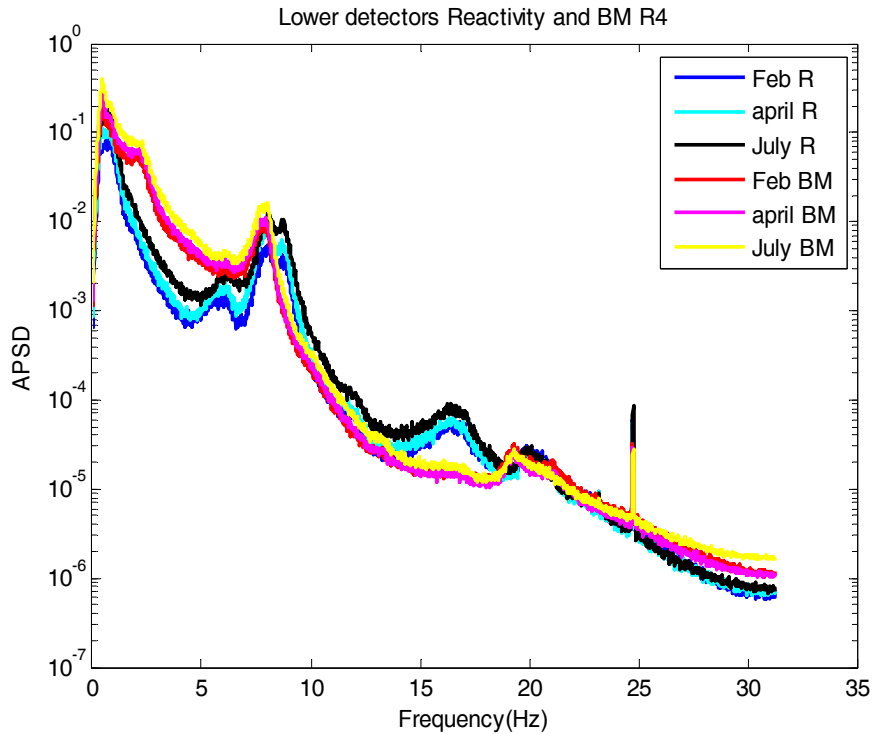


*Fig. 72 APSDs of the reactivity component (Mode 2, dark blue, blue and black lines) and of the beam mode (Mode 1, red, purple and yellow lines) after the separation, extracted from the measurement taken in February, April and July 2014, respectively, at Ringhals-4 for the lower detectors.*

Unlike in all the previous measurements, the separated reactivity component still has a double peak. The reason for this is not known. This indicates that in the present cycle, also the beam mode movement induces a non-negligible reactivity component. This is unexpected since, as it was discussed in the previous report, due to symmetry considerations, the reactivity effect of the pendular vibrations of the core barrel will be only of second order of the (small) vibration amplitude. One explanation could be if the symmetry of the core loading and the geometry of the core is not as complete as it is expected.

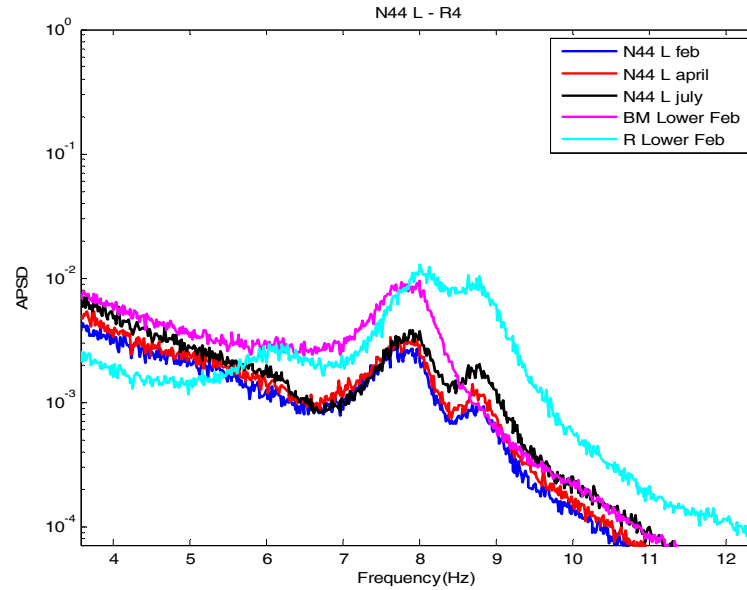


*Fig. 73 APSDs of the individual lower detector N44 (blue, red and black lines, taken in February, April and July 2014, respectively), the reactivity component (Mode 2, cyan line, February) and the beam mode (Mode 1, purple line, February) after the separation, extracted from the measurements in 2014 at Ringhals-4.*

On the other hand, the beam mode only contains only a single peak, as usual.

Another difference compared to the previous cycles is that the peak frequency of the modes is slightly different from the previous measurements. In Fig. 73, Mode 1 is situated at around 8 Hz, whereas Mode 2 is close to 9 Hz.

In order to check that the first Mode is related to the beam mode vibrations, coherences and phases between the two opposite detector pairs are calculated. The results are shown in Fig. 74 and Fig. 75. They both show similar characteristics. The coherence is relatively high at 8 and 9 Hz, and has a sharp dip in between. At the frequency of the first peak (8 Hz), corresponding to Mode 1, the signals of the opposite detectors are out of phase. At the frequency of the second peak (9 Hz), that is Mode 2, the signals of the opposite detectors are in-phase. This is in line with all the previous results and further confirms the hypothesis about the physical origin of the two peaks.

Finally, the evolution trend of the two components is shown in Fig. 76. It shows the same trend as in the previous cycles, i.e. that the amplitude of the reactivity mode increases more during the time span of the measurements than the beam mode. The only difference compared to the previous cycles is that the beam mode amplitude also increases, whereas it was approximately constant during the cycle in the previous cycles. This could be related to the fact that the reactivity component this time showed two peaks, which were not separated in the analysis. Further measurements will help to clarify these newly observed characteristics.

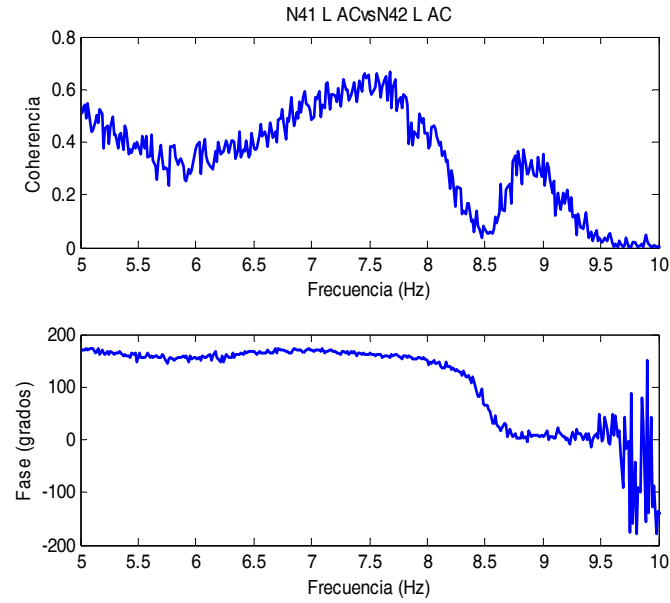


*Fig. 74 Coherence and phase between opposite lower ex-core detector signals N41 and N42, estimated from the measurements taken in 2014 at Ringhals-4*

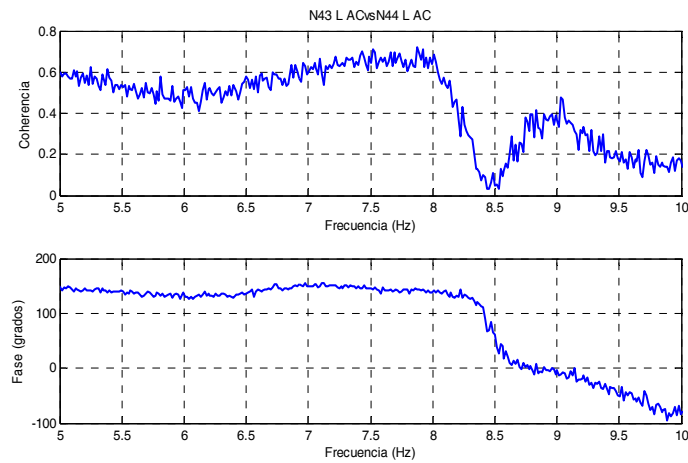


*Fig. 75 Coherence and phase between opposite lower ex-core detector signals N43 and N44, estimated from the measurements taken in 2014 at Ringhals-4*

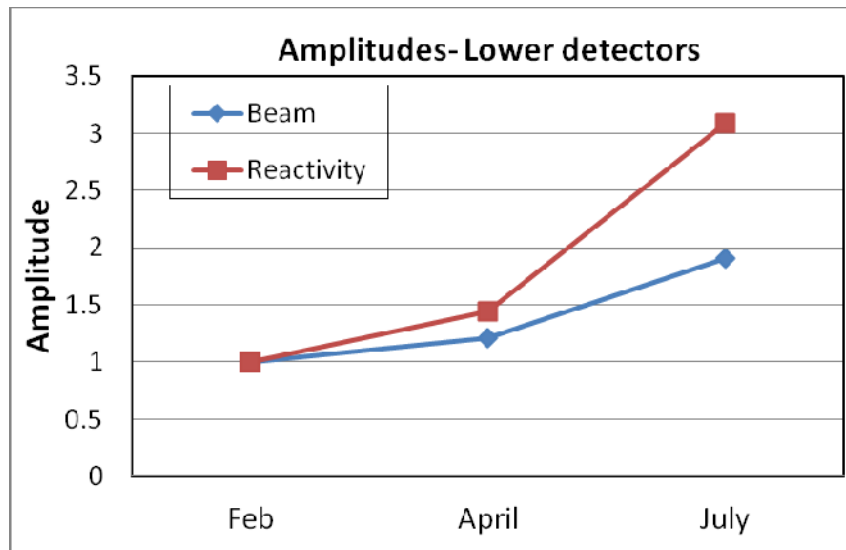


Fig. 76 Time evolution of the amplitude of the two modes in the measurements taken in 2014 at Ringhals-4